

## ABSTRACT

Title of Document: HOMOLEPTIC NAKED CLUSTERS OF  
ENDOEDRAL ZINTL IONS

Emren Nalbant Esentürk,  
Doctor of Philosophy, 2006

Directed By: Professor Bryan W. Eichhorn  
Department of Chemistry and Biochemistry

Nanoclusters are of interest because of their remarkable catalytic properties and their application in nanotechnology fields. There is a strong preference toward bimetallic systems due to their superior catalytic properties compare to monometallic systems. Synthetic protocols are developed by using polyatomic main group clusters (Zintl ions) for making new bimetallic nano-catalysts. In this study, new, free standing, transition metal stabilized Zintl ions have been isolated. They are promising candidates to be used both in nanotechnology and heterogeneous catalysis.

$[M@Pb_{12}]^{2-}$  (M = Ni, Pd, Pt) are the *first isolated* free-standing centered icosahedra without any attendant of ligands. The anions contain naked  $Pb_{12}$  icosahedra clusters encapsulating Group 10 transition metals and posses near perfect  $I_h$  point symmetry. These endohedral naked metal clusters have nontraditional spherical aromatic electronic structures. They are the smallest members of the nanoparticle growth sequence,  $M_{13}$  (centered icosahedra), with hcp lattices. Their

positive chemical shifts in  $^{207}\text{Pb}$  NMR spectra contradict theoretical chemical shift calculations of isostructural aromatic clusters.

A new type of Zintl ion,  $[\text{Ni}@\text{Pb}_{10}]^{2-}$ , has also been synthesized. The anion contains Ni atom centered in a *closo*- $\text{Pb}_{10}^{2-}$  bicapped square antiprism, and possesses virtual  $D_{4d}$  point symmetry. It is the first isolated ten atom, homoatomic naked Zintl ion cluster. The Pt and Pd analogs, and non-metallated  $\text{Pb}_{10}$  and  $\text{Pb}_{12}$  clusters have also been observed in the gas phase by LDI-TOF-MS.

NMR spectroscopy was used to investigate unusual dynamic behaviors of the one focus  $[\text{Ni}@\text{Pb}_{10}]^{2-}$  and two focus  $[\text{Ni}_2\text{Sn}_{17}]^{4-}$  anions and both demonstrated surprising global atomic mobility. The latter has a capsule like structure having central Sn atom with coordination number of eight. This extraordinary high coordination of the central Sn is more akin to solid state compounds.

The  $[\text{Ge}_9\text{Ni}_2(\text{PPh}_3)]^{2-}$  anion is the new example of Zintl ion, which do not adopt Wadlan type structure. Another Ni-Ge system with exciting structure,  $[\text{Ni}_6\text{Ge}_{13}(\text{CO})_5]^{4-}$  is also isolated. The anion has interpenetrating biicosahedral structure which is unique to Zintl ion chemistry. The potential interconversion of  $[\text{Ge}_9\text{Ni}_2(\text{PPh}_3)]^{2-}$  and  $[\text{Ni}_6\text{Ge}_{13}(\text{CO})_5]^{4-}$  have been investigated through ESI-MS studies.

HOMOLEPTIC NAKED CLUSTERS OF ENDOHEDRAL ZINTEL IONS

By

Emren Nalbant Esentürk

Dissertation submitted to the Faculty of the Graduate School of the  
University of Maryland, College Park, in partial fulfillment  
of the requirements for the degree of  
Doctor of Philosophy  
2006

Advisory Committee:  
Professor Bryan W. Eichhorn, Chair  
Professor Lawrence R. Sita  
Professor William F. McDonough  
Associate Professor Robert A. Walker  
Assistant Professor Andrei Vedernikov

© Copyright by  
[Emren Nalbant Esenturk]  
[2006]

## Dedication

To my husband,  
my lovely son  
and my parents.

# Table of Contents

Dedication .....	ii
Table of Contents .....	iii
List of Tables .....	vi
List of Figures .....	vii
Chapter 1 Introduction .....	1
1.1. Introduction.....	1
1.2. Nanoclusters.....	4
1.3. Bimetallic Catalysts .....	8
1.4. Zintl Ions.....	11
1.5. Overview of the Thesis .....	17
Chapter 2 $[M@Pb_{12}]^{2-}$ (M = Pt, Pd, Ni).....	19
2.1. Introduction.....	19
2.2. Results.....	20
2.2.1. Synthesis .....	20
2.2.2. Solid State Structure .....	22
2.2.3. NMR Spectroscopic Studies .....	28
2.2.4. Laser Desorption Ionization Time-of-Flight Mass Spectrometry.....	31
2.2.5. Extended Hückel Molecular Orbital Calculations .....	36
2.3. Discussion .....	38
2.4. Experimental Section.....	42
2.4.1. General Data .....	42
2.4.2. Chemicals.....	43
2.4.3. Synthesis .....	44

Chapter 3 The closo-Pb <sub>10</sub> <sup>2-</sup> Zintl ion in the [Ni@Pb <sub>10</sub> ] <sup>2-</sup> cluster.....	47
3.1. Introduction.....	47
3.2. Results and Discussion .....	49
3.2.1. Synthesis .....	49
3.2.2. Solid State Structure .....	50
3.2.3. NMR Spectroscopic Studies .....	53
3.2.4. LDI-TOF Mass Spectrometry.....	55
3.2.5. DFT analysis on [M@Pb <sub>10</sub> ] <sup>2-</sup> (M = Ni, Pd, Pt) clusters.....	58
3.3. Conclusion .....	61
3.4. Experimental Section.....	63
3.4.1. General Data .....	63
3.4.2. Chemicals.....	64
3.4.3. Synthesis .....	64
Chapter 4 Synthesis, Structure and Dynamic Properties of [Ni <sub>2</sub> Sn <sub>17</sub> ] <sup>4-</sup> .....	66
4.1. Introduction.....	66
4.1.1. Results.....	67
4.1.2. Synthesis .....	67
4.1.3. Solid State Structure .....	68
4.1.4. NMR Spectroscopic Studies .....	72
4.1.5. Electrospray Mass Spectrometry .....	74
4.2. Discussion.....	76
4.3. Experimental Section.....	78
4.3.1. General Data .....	78
4.3.2. Chemicals.....	78
4.3.3. Synthesis .....	79
Chapter 5 Synthesis and Characterization of the [Ni <sub>6</sub> Ge <sub>13</sub> (CO) <sub>5</sub> ] <sup>4-</sup> and [Ge <sub>9</sub> Ni <sub>2</sub> (PPh <sub>3</sub> )] <sup>2-</sup> Zintl ion Clusters.....	81

5.1. Introduction.....	81
5.2. Results and Discussion .....	83
5.2.1. Synthesis .....	83
5.2.2. Solid State Structures.....	85
5.2.3. NMR Spectroscopic Studies .....	93
5.2.4. Electrospray Mass Spectrometry .....	93
5.3. Conclusions.....	96
5.4. Experimental Section.....	97
5.4.1. General Data .....	97
5.4.2. Chemicals.....	98
5.4.3. Synthesis .....	98
5.4.4. Interconversion Studies.....	99
5.4.5. Crystallographic Studies .....	100
Chapter 6 Conclusions .....	101

## List of Tables

Table 2.1. Crystallographic data for the $[M@Pb_{12}]^{2-}$ (M = Pt, Pd, Ni) ions. ....	24
Table 2.2. Selected bond lengths [ $\text{\AA}$ ] for $[M@Pb_{12}] [K(2,2,2\text{-crypt})]_2$ (M = Ni, Pd, Pt). ....	25
Table 2.3. Selected bond angles [ $^\circ$ ] for $[M@Pb_{12}] [K(2,2,2\text{-crypt})]_2$ (M = Pt, Pd, Ni). ....	26
Table 2.4. Diagonal and Pb-M, Pb-Pb distances of the $[M@Pb_{12}]^{2-}$ (M = Pt, Pd, Ni) anions. ....	26
Table 2.5. The $^{207}\text{Pb}$ NMR chemical shifts. ....	28
Table 2.6. The $\sigma$ - Aromaticity in centered lead clusters. ....	41
Table 3.1. Crystallographic data for the $[Ni@Pb_{10}]^{2-}$ ion. ....	51
Table 3.2. Selected bond lengths [ $\text{\AA}$ ] and angles [ $^\circ$ ] for $[NiPb_{10}] [K(2,2,2\text{-crypt})]_2$ ..	52
Table 3.3. Calculated bond lengths [ $\text{\AA}$ ] for $[M@Pb_{10}]^{2-}$ (M = Ni, Pd, Pt). ....	59
Table 4.1. Crystallographic data for the $[Ni_2Sn_{17}]^{4+}$ ion. ....	70
Table 4.2. Selected bond lengths [ $\text{\AA}$ ] and angles [ $^\circ$ ] for $[Ni_2Sn_{17}] [K(2,2,2\text{-crypt})]_4 \cdot 2en$ . ....	71
Table 5.1. Summary of Crystallographic Data for the $[Ni_6Ge_{13}(CO)_5]^{4+}$ and $[Ge_9Ni_2(PPh_3)]^{2-}$ Ions. ....	88
Table 5.2. Selected bond distances [ $\text{\AA}$ ] and angles [ $^\circ$ ] for the $[Ge_{13}Ni_6(CO)_5]^{4+}$ ion. .	91
Table 5.3. Selected bond distances [ $\text{\AA}$ ] and angles [ $^\circ$ ] for the $[Ge_9Ni_2(PPh_3)]^{2-}$ ion. .	92

## List of Figures

Figure 1.1. Growth sequence of full-shell, ‘magic number’ clusters. <sup>25</sup> .....	5
Figure 1.2. Structures of soluble homoatomic Group 14 anions a) $[E_5]^{2-}$ , E = Ge, Sn, Pb; b) $[E_6]^{2-}$ in $[\{E-Cr(CO)_5\}_6]^{2-}$ with E = Ge, Sn; c,d) $[E_9]^{x-}$ (E = Si-Pb, x = 3,4) (taken from reference <sup>78</sup> ). .....	13
Figure 2.1. ORTEP drawings of the $[Pt@Pb_{12}]^{2-}$ ion showing a) the icosahedral structure and b) a view down the $\bar{3}$ axis. Pt is red, Pb is green, thermal ellipsoids are set at the 50% probability level. ....	22
Figure 2.2. ORTEP drawing of fully labeled $[M@Pb_{12}]^{2-}$ (M=Pt, Pd, Ni) anions showing the icosahedral structure. Thermal ellipsoids are set at the 50% probability level. ....	23
Figure 2.3. (a) The <sup>207</sup> Pb NMR spectrum of $[Pt@Pb_{12}]^{2-}$ ion recorded in dmf @ 11 °C and 83.7 MHz., (b) The <sup>195</sup> Pt NMR spectrum of $[Pt@Pb_{12}]^{2-}$ ion recorded in dmf @ 11 °C and 107.5 MHz. ....	29
Figure 2.4. The <sup>207</sup> Pb NMR spectrum of (a) $[Pt@Pb_{12}]^{2-}$ ion recorded in dmf @ 11 °C and 83.7 MHz., (b) $[Pd@Pb_{12}]^{2-}$ ion recorded in dmf @ 15 °C and 104.7 MHz, (c) $[Ni@Pb_{12}]^{2-}$ ion recorded in dmf @ 25 °C and 104.7 MHz. ....	30
Figure 2.5. LDI-TOF mass spectrum of $[K(2,2,2-crypt)]_2[Pt@Pb_{12}]$ crystals. Arrows denote the potassium coordinated ion pairs. ....	32
Figure 2.6. The LDI-TOF mass spectrum of the (a) $[Pt@Pb_{12}]^{-1}$ , (b) $[Pd@Pb_{12}]^{-1}$ , and (c) $[Pt@Pb_{12}]^{-1}$ ions. The insets show the calculated mass envelope of the corresponding ions. ....	33

Figure 2.7. The LDI-TOF mass spectrum of the (a) $[\text{Pt@Pb}_{10}]^{-1}$ , (b) $[\text{Pd@Pb}_{10}]^{-1}$ , and (c) $[\text{Pt@Pb}_{10}]^{-1}$ ions. The insets show the calculated mass envelope of the corresponding ions.....	34
Figure 2.8. The LDI-TOF mass spectrum of the (a) $[\text{Pb}_{12}]^{-1}$ , (b) $[\text{Pb}_{10}]^{-1}$ ions. The insets show the calculated mass envelope of the corresponding ions and their proposed structures.....	35
Figure 2.9. Qualitative MO diagram for the $[\text{Pt@Pb}_{12}]^{2-}$ ion constructed from the Pt atom and $\text{Pb}_{12}^{2-}$ fragments with the aid of Extended Hückel molecular orbital calculations. The highest occupied $h_g$ levels of the $[\text{Pt@Pb}_{12}]^{2-}$ complex and $\text{Pb}_{12}^{2-}$ fragment were normalized for comparison.....	37
Figure 2.10. Qualitative MO diagram for the $[\text{Pt@Pb}_{12}]^{2-}$ and $[\text{Al@Pb}_{12}]^{+}$ ions (figure is taken from reference <sup>39</sup> ).....	40
Figure 3.1. ORTEP drawing of the $[\text{Ni@Pb}_{10}]^{2-}$ ion showing bicapped square antiprism structure. Ni is yellow, Pb is yellow. Thermal ellipsoids are set at the 50% probability level.....	50
Figure 3.2. The $^{207}\text{Pb}$ NMR spectrum of the $[\text{Ni@Pb}_{10}]^{2-}$ ion recorded in dmf at 25 °C and 104.7 MHz. Table show change in line width ( $\nu\Delta_{1/2}$ ) with temperature. ....	53
Figure 3.3. Temperature dependence of the $^{207}\text{Pb}$ NMR line widths of $[\text{Ni@Pb}_{10}]^{2-}$ and $[\text{Ni@Pb}_{12}]^{2-}$ .....	54
Figure 3.4. The LDI-TOF mass spectrum of a) the $[\text{Pb}_{10}\text{Ni}]^{-1}$ and b) $[\text{Pb}_{10}\text{Ni K}]^{-1}$ ions. c) The insets show the calculated mass envelope of the $[\text{Pb}_{10}\text{Ni}]^{-1}$ and $[\text{Pb}_{10}\text{Ni K}]^{-1}$ ions. ....	55
Figure 3.5. The LDI-TOF mass spectrum of the a) $[\text{Pt@Pb}_{10}]^{-1}$ , b) $[\text{Pd@Pb}_{10}]^{-1}$ , and c) $[\text{Ni@Pb}_{10}]^{-1}$ ions. The insets show the calculated mass envelope of the corresponding ions.....	57
Figure 4.1. ORTEP drawing of the $[\text{Ni}_2\text{Sn}_{17}]^{4+}$ ion. Ni is yellow, Sn is blue, thermal ellipsoids are set at the 50 % probability level. ....	69

Figure 4.2. The $^{119}\text{Sn}$ NMR spectrum of the $[\text{Ni}_2\text{Sn}_{17}]^{4-}$ ion recorded in dmf at a) -64 °C b) 0 °C and c) 60 °C. ....	73
Figure 4.3. Negative ion ESI mass spectrum of $[\text{K}(2,2,2\text{-crypt})]_4[\text{Ni}_2\text{Sn}_{17}]$ . The labels represent the number of Sn atom (n) in the $[\text{K}(2,2,2\text{-crypt})\text{Ni}_2\text{Sn}_n]^{1-}$ series of ions. P is the oxidized $[\text{Ni}_2\text{Sn}_{17}]^{1-}$ parent ion. The insets show the $[\text{K}(2,2,2\text{-crypt})]_4[\text{Ni}_2\text{Sn}_{17}]^{1-}$ peak (17) and its simulated pattern (17').....	75
Figure 5.1. a) ORTEP drawing of the $[\text{Ni}_6\text{Ge}_{13}(\text{CO})_5]^{4-}$ anion. Ni is yellow, Ge is blue, C is gray and oxygen is red. b) The two interpenetrating icosahedral subunits, Ih1 and Ih2.....	86
Figure 5.2 ORTEP drawing of the $[\text{Ge}_9\text{Ni}_2(\text{PPh}_3)]^{2-}$ anion, (2) Ni is yellow, Ge is blue, C is gray, P is purple and H is turquoise.....	90
Figure 5.3. Experimental ESI-MS isotopic pattern of a) $[\text{K}(2,2,2\text{-crypt})\text{Ge}_{13}\text{Ni}_6(\text{CO})_4]^{1-}$ a') Simulated pattern of A, b) $[\text{K}(2,2,2\text{-crypt})\text{Ge}_{13}\text{Ni}_6(\text{CO})_5]^{1-}$ , b') Simulated pattern of b. ....	94
Figure 5.4. a) ESI-mass spectrum of the $\text{K}[\text{Ge}_9\text{Ni}_2(\text{PPh}_3)]^{1-}$ molecular ion. The inset shows the simulated mass envelope, b) Observed and calculated ESI-MS mass envelope for $[\text{K}(2,2,2\text{-crypt})\text{Ge}_9\text{Ni}_2(\text{CO})]^{1-}$ .....	95

# Chapter 1

## Introduction

### 1.1. Introduction

The growing demand on new technologies in the twenty first century is for the miniaturization of devices into nanometer size with enhanced performances. Currently, nanomaterials are subject of intense research with applications in wide variety of areas including medicine, electronics and synthesis of novel materials with unique properties.<sup>1-3</sup>

Nanomaterials, defined by some as a diameter of less than 10 nm,<sup>4</sup> have properties between those of atoms and bulk materials. Their unique properties along with enhanced performances are determined by their chemical compositions, surface structures and interparticle interactions besides their sizes. Appropriate control of these properties can lead to discovery of new class of high-performance materials.<sup>5</sup>

The history of the nanoparticles goes back to the mid-nineteenth century when Michael Faraday attributed the red color of colloidal gold to its finely divided state.<sup>6</sup> His early speculative experiments laid the foundation for some of the current optical and biological applications of gold nanoparticles. With the advent of new analysis techniques as well as the availability of innovative synthesis methods, new

nanoparticles have been developed with better understanding. For example, bimetallic alloys and core-shell nanoparticles have become great interest due to their unusual catalytic, optical and magnetic properties.<sup>5, 7</sup> New synthetic methods are being developed to prepare uniform, relatively monodispersed bimetallic particles in increasingly smaller size ranges (1-5 nm) for variety of bimetallic systems.<sup>7</sup>

Although the current characterization techniques provide valuable information about the size, morphology and approximate crystallographic form of these particles, it is still a challenge to determine the properties and structural details of materials in the nano-regime. In some cases, these nanomaterials have never been investigated due to the lack of appropriate synthetic methods available to prepare uniform (single phase), monodispersed binary nanoparticles. For example, one of the most extensively studied transition metal / main group bimetallic catalyst, the Pt-Sn system, shows desirable catalytic properties such as stability and durability in heterogeneous catalysis (e.g. CO oxidation in fuel cells).<sup>8-12</sup> However, conventional preparation methods lead to mixtures of Pt-Sn phases rather than single-phase PtSn alloys.<sup>10, 13</sup> Mixed phases make characterizing the identity of the active phase, and relating catalytic properties to an individual phase challenging.

Another promising area in the search of new bimetallic nanoparticles is the development of increasingly large molecular bimetallic clusters that approach or achieve bulk alloy structure. The major goal of cluster science is to discover new clusters with special electronic and structural stabilities so that they can be used as seeds for larger clusters. However, mechanism of nanocluster growth is not very well understood and isolating them is very difficult. The known clusters often rely on

tightly bound ligand shells that provide fixed nuclearity with exact monodispersity and minimal disorder in the crystal lattice. Although the ligated clusters are more amenable to structural and spectroscopic characterization and provide valuable information about the bimetallic nanoparticle architecture, the ligand shell can alter or eliminate the reactivity and properties of the nanoparticle core.

Transition metal derivatives of the polyatomic main group anions (Zintl ions) bridge the chemistry of large clusters and nanoparticles. They are possible nucleation sites for nanoparticle growth and also ideal precursors for making new bimetallic catalysts.

The group 14 polyatomic anions are prominent members of the Zintl ion family. The synthesis, characterization and exploration of unusual structural properties of new bimetallic anions from combinations of transition metals with group 14 Zintl ions was the objective of this study. Here, unique types of transition metal stabilized Zintl ion clusters have been isolated with their remarkable structures, non-traditional bonding natures, and unusual electronic and spectroscopic properties. They are promising candidates to be used as seeds for nanoparticles and also provide access to bimetallic catalysts. In addition, they have intriguing spectroscopic properties associated with sigma aromaticity. Since they are formed by NMR spin active metal atoms, it is possible to study dynamic properties by the way of NMR spectroscopy. Such studies open the ways of understanding the details of the structures and properties of nanoparticles such as the depressed melting points of nanoparticles compared to those of the bulk metals and alloys.<sup>14</sup>

As such the introduction of this thesis is organized as follows: first an overview of nanoclusters and bimetallic catalysts is provided, and Zintl ion complexes are reviewed.

## 1.2. Nanoclusters

Nanoclusters are monodispersed particles with the sizes generally less than 10 nm in diameter. They are attracting great interest due to their potential applications in areas such as chemical sensors<sup>15</sup>, flat-panel displays<sup>16</sup>, and quantum computers and devices.<sup>17-19</sup> They have also found extensive application in catalysis, such as oxidation of CO and hydrogenation of olefins.<sup>20, 21</sup> It is believed that their high catalytic activity and selectivity is due to a well-ordered, high ratio of atoms located on the surface.<sup>22</sup> The possibility of controlling cluster size and the surface structures gives them a distinct advantage over all nanoparticles and provides the possibility for a better understanding their unique properties.

Clusters have tendency to coalesce. Therefore, they have to be stabilized against coalescing into larger particles, and eventually bulk material. There are two ways to accomplish the stabilization and prevent coalescing. The first one is to protect clusters by coating them with one form or another (e.g. ligands, polymers, surfactants).<sup>23, 24</sup> The other method is to prepare individual stable clusters that interact weakly with one another. It is believed that clusters with complete, regular outer geometries are relatively more stable. These types of clusters are called magic number clusters and are constructed by surrounding a single metal atom progressively with layers of metal atoms in a cubic close packed arrangement.<sup>14</sup>

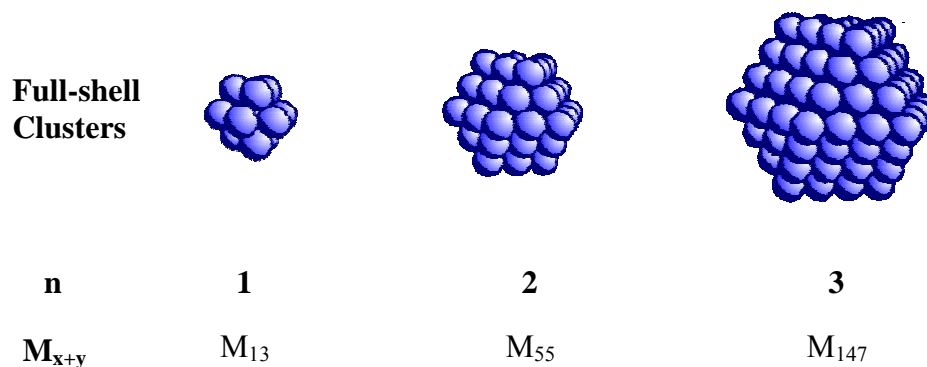


**Figure 1.1.** Growth sequence of full-shell, ‘magic number’ clusters.<sup>25</sup>

The total number of metal atoms in the cluster is calculated from the summation of number of atoms forming inner shells (x) and the number of atoms in the outer shell (y), which is calculated per *n*th shell according to,  $y = 10n^2 + 2$  ( $n > 0$ ). Thus full-shell, “magic number”, metal clusters have a  $M_{13}$  ( $x = 1, y = 12$ ),  $M_{55}$  ( $x = 13, y = 42$ ),  $M_{147}$  ( $x = 55, y = 92$ ),  $M_{309}$ ,  $M_{561}$ ,  $M_{923}$  (and so on) growth sequence. Figure 1.1 shows an idealized illustration of hexagonal close-packed full-shell clusters. Some of the clusters are the metal cores of the series of larger cluster molecules, such as an anticuboctahedron  $Rh_{13}$  core and icosahedron  $Au_{13}$  core, prepared by Schmid and coworkers.<sup>14</sup> They also synthesized a  $M_{55}$  core, uncharged cluster molecule,  $[Au_{55}(PPh_3)_{12}Cl_6]$ , which is the first example of a well-defined ligand-stabilized nanocluster.<sup>14</sup> Another important ‘magic number’ cluster is Moiseev et al.’s giant cationic cluster,  $Pd_{561}L_{60}(OAc)_{180}$ .<sup>26</sup> It is one of the most widely studied catalytic nanocluster systems in the literature and is known as the first example of isolated nanocluster that did catalysis in solution.

Clusters have also been studied extensively by physical chemists as well as inorganic chemists. While inorganic chemists have been isolating an enormous

variety of exciting ligated metal clusters in condensed phase environment for years, physical chemists have been investigating ligand free, gas phase clusters often in molecular beams and made theoretical predictions on their structures and bonding. For example, Castelman et al. presented experimental evidence for ionically bound magic number cluster,  $\text{Al}_{13}^{1-}$ .<sup>27</sup> Bowen et al. have succeeded in forming  $\text{KAl}_{13}$  in molecular beams.<sup>28</sup> The cluster consists of an anionic icosahedral  $\text{Al}_{13}^-$  core and a  $\text{K}^+$  located on the outer surface. They spectroscopically verified the theoretical prediction that the compound is ionically-bonded and could form the basis for making cluster-based materials.

Important advancements in the condensed phase have been achieved as well. For example, the highly symmetric metalloid aluminum cluster,  $[\text{Al}_{77}\text{R}_{20}]^{2-}$  ( $\text{R} = \text{N}(\text{SiMe}_3)_2$ ) which has a negatively charged  $\text{Al}_{13}$  center have been isolated by Schnokel et al.<sup>29</sup> The  $\text{Al}_{13}$  center is surrounded by two polyhedral shells having 44 and 20 Al atoms and 20 organic ligands are stabilizing the  $\text{Al}_{77}$  core against the formation of bulk metal.

Aside from monometallic clusters with unique properties, binary clusters are also well suited for the purpose of being ideal building blocks for nanomaterials. With their increased functionality, they show high stability, improved catalytic properties along with possibility of modifying cluster properties such as size, shape, and composition.<sup>30</sup> In particular, highly symmetric clusters with an encapsulated atom (i.e. 13-atom icosahedra) are especially intriguing. While variety of centered, binary clusters have been investigated and predicted by theoretical studies,<sup>31-33</sup> very few have been studied experimentally.<sup>34-36</sup> However, structural data are sparse, and most

of them are observed in gas phase.<sup>34, 37, 38</sup> For example, Schleyer et al identified  $\text{Al@Pb}_{10}^{1+}$  and  $\text{Al@Pb}_{12}^{1+}$  clusters in the gas phase by mass spectroscopy.<sup>39</sup> The clusters presumably have the structures with  $D_{4d}$  and  $I_h$  point symmetry, respectively. Pyykko et al. predicted centered icosahedral cluster-compound,  $\text{W@Au}_{12}$ ,<sup>33</sup> and it was prepared experimentally by Wang et al. in gas phase.<sup>37</sup> Subsequently, Mo, V, Nb, and Ta analogs of this cluster have also been reported by the same group.<sup>34, 38</sup>

Besides structural and optical properties of highly symmetric clusters, their spectroscopic properties have also been subject of interest. For example, theoretical studies have been performed on inorganic cage molecules to explain spherical aromaticity. In 1996, Schleyer et al proposed the NICS (Nucleus Independent Chemical Shift) method to explain aromatic and antiaromatic natures of the closed-shell clusters (via their calculated NMR chemical shifts).<sup>40</sup> The NICS method is based on DFT type NMR chemical shift calculations where shielding tensor is calculated for each orbital contribution separately, and the sum of all orbital contributions gives the shielding tensor.<sup>41</sup> According to these calculations the clusters with negative NICS values (diatropic chemical shift) denote aromaticity and positive NICS values (paratropic chemical shift) indicate antiaromaticity.<sup>40</sup> NICS method has been applied to variety of cluster molecules.<sup>42, 43</sup> For example,  $\text{Si}_{12}^{2-}$  has antiaromatic nature with its positive NICS value.<sup>42</sup> On the other hand,  $\text{Al@Pb}_{12}^{+}$  and  $\text{Al@Pb}_{10}^{+}$  clusters revealed aromatic character which is explained by their negative NICS values.<sup>39</sup> However, no experimental proof of the  $\sigma$ -aromaticity of the compounds have been reported. One of the few experimental measures for such systems regarding  $\sigma$ -aromaticity is presented in Chapter 2. Theoretical NICS and experimental  $^{207}\text{Pb}$  NMR

chemical shift values for the isolated, transition metal centered icosahedra,  $[\text{Pt}@\text{Pb}_{12}]^{2-}$  are compared.

### 1.3. Bimetallic Catalysts

Monometallic and bimetallic heterogeneous catalysts have found many important industrial applications such as naphtha reforming<sup>44</sup> and conversion of CO in automobile exhaust.<sup>45</sup> During the 1960's, Pt on alumina ( $\text{Al}_2\text{O}_3$ ) was the most commonly used reforming catalyst.<sup>46</sup> However, bimetallic catalysts have become more popular and have replaced traditional monometallic Pt catalysts in reforming processes due to their high stability and activity.<sup>47</sup>

Reforming is a process that converts saturated hydrocarbons in petroleum naphtha fractions into aromatic hydrocarbons. Some of the major reactions that occur during reforming are the conversion of alkanes or cyclic alkanes to aromatic hydrocarbons either by dehydrogenation or dehydrocyclization, isomerization of n-alkanes and fragmentation reactions (hydrocracking and hydrogenolysis).<sup>47</sup> Due to the high temperature reactions during the reforming of hydrocarbons, formation of unsaturated hydrocarbon residue occurs. Hydrocarbon residues cause carbon agglomeration on the catalyst surface, known as coke deposition, resulting in catalyst deactivation.<sup>10</sup> It has been observed that alloying of platinum with a second metal, main group or transition metal, (i.e. PtSn systems) increases resistance to coke formation as well as selectivity and stability over a longer period of time.<sup>48</sup> Although bimetallic systems have superior catalytic properties compared to monometallic catalysts in most cases, it is still unclear why the addition of a second metal (Sn)

increases catalyst stability and decreases coke deposition. There are different explanations debated in the literature. Some studies report that the addition of the second metal may influence the first metal by directly reacting with intermediates or reactants.<sup>9, 49</sup> Other reports suggest that the second metal (Sn) causes the Pt atoms to be more dispersed. Dilution of Pt reduces the probability of carbon residue agglomeration and deactivation of the catalyst.<sup>10, 49</sup> Therefore, advances in catalysis require more fundamental knowledge about interatomic interaction and properties.

CO oxidation is one of the most substantial and basic reactions in heterogeneous catalysis. Having separate sites for each reactant in bimetallic catalysts, i.e. Pt-Sn, promotes greater activity than monometallic Pt catalysts. In monometallic catalysts, both reactants (CO and O<sub>2</sub>) compete for the same binding site, this hinders the CO oxidation rate since the oxygen adsorption is limited by CO desorption.<sup>11</sup>

Pt alloys (e.g. Pt-Sn, Pt-Ru) are also in use for CO oxidation in fuel cells as PROX (preferential oxidation) catalysts.<sup>11, 50</sup> During the reforming process, CO gas is produced as well as H<sub>2</sub> gas from the fuel. The CO in the reformed gas binds to the surface of the catalyst at the anode and decreases the activity of catalyst thereby decreasing the efficiency of the fuel cell. Therefore, before contacting the anode the amount of CO in the gas has to be lowered to a level that the anode catalyst can tolerate. The PROX catalysts are used to make the anode more tolerant by converting CO to CO<sub>2</sub> prior to the fuel gases reaching the anode.

The superior catalytic properties of Pt-Sn systems encouraged researchers to investigate other transition metal / group 14 alloys. For instance, Pt-Ge catalysts have

been shown to exhibit enhanced properties in hydrocarbon reforming reactions, such as increased selectivity toward aromatics<sup>51, 52</sup> and tolerance towards sulfur.<sup>51, 53</sup> It is reported that Al<sub>2</sub>O<sub>3</sub> supported Pt-Ge bimetallic catalysts show remarkable thio-resistance during the reforming process.<sup>53</sup> In these studies, the superior performance is explained by assuming that Ge increases the electrophilic character of Pt, and this weakens the Pt-S bond strength and decreases the amount of sulfur poisoning. Addition of Pb to Al<sub>2</sub>O<sub>3</sub> supported Ni or Pd in order to improve catalytic properties has also been reported.<sup>54, 55</sup> These studies also show high selectivity and stability of Ni-Pb (or Pt-Pb) in the hydrogenation of unsaturated hydrocarbons.

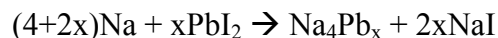
These studies indicate that the transition metal / group 14 alloyed bimetallic catalysts have desirable properties for many catalytic processes, i.e. naphtha reforming and CO oxidation. Improvement of synthetic routes for preparing these bimetallic catalyst systems by using molecular heterometallic cluster precursors is receiving increased attention. However, the currently used molecular precursors are not convenient because they have ligand stabilizers, and multiple steps and high temperatures are required to activate the bimetallic catalyst. For example, one traditional preparation technique, impregnation of support, uses PtCl<sub>2</sub>(PPh<sub>3</sub>)<sub>2</sub> and SnCl<sub>2</sub> as precursors to prepare Pt-Sn alloys.<sup>12</sup> Catalysts need to be activated by removal of ligands at high temperature. During this activation process decomposition and/or oxidation of the compounds can take place. Ligands attached to the metal such as Cl<sup>-</sup> and PPh<sub>3</sub> cause contamination and deactivation of the catalyst. Therefore, it would be desirable to use ligand-free binary clusters as precursors to prepare bimetallic catalysts.

The requirement of multiple steps and high temperatures for synthesis leads to development of new synthetic routes for bimetallic catalyst preparation. Zintl ions, which are polyatomic main group clusters, form complexes with transition metals at low temperatures. Oxidation of these complexes results in the formation of ligand free bimetallic alloys.<sup>56, 57</sup> Therefore, transition metal / Zintl ion complexes are ideal precursors for making new binary alloy catalysts. In addition, the preparation of these catalysts at low temperatures from ligand free precursors will facilitate characterization and understanding of catalytic properties.

#### 1.4. Zintl Ions

The main group polyanions, Zintl ions, were discovered in the 1890's by Joannis,<sup>58, 59</sup> Kraus,<sup>60, 61</sup> and Smyth<sup>62</sup> with the study of alkali metal plumbides. They observed that the reaction of excess Pb with Na in liquid ammonia produced an intense green-colored solution, from which NaPb<sub>4</sub> and NaPb<sub>2</sub> precipitated.<sup>58, 59</sup> These salts were electrolytes in liquid ammonia to give Na<sup>+</sup> and Pb<sup>n-</sup> (n = 2, 4) ions. These studies formed the basis for the identification of other main-group polyanionic salts by electrolytic methods such as Na<sub>4</sub>Pb•Pb<sub>8</sub>, Na<sub>4</sub>Sb•Sb<sub>6</sub>, and Na<sub>2</sub>Te•Te<sub>3</sub>, where Pb<sub>9</sub><sup>4-</sup>, Sb<sub>7</sub><sup>3-</sup>, Te<sub>4</sub><sup>2-</sup> anions present in the solution, respectively.<sup>61</sup>

In the 1930's, Zintl and co-workers conducted an extensive study on the group 14 and 15 polyanions. They showed that homopolyatomic main group anions can be collected by adjusting the concentration of the solution. They used potentiometric titrations of sodium and potassium in liquid ammonia with a salt of the metal (e.g. PbI<sub>2</sub>) to prepare polylead anions according to equation 1.1.<sup>63</sup>



## 1.1

Zintl and co-workers have shown that variety of polyatomic anions of main-group metals can be prepared by electrochemical methods like  $\text{E}_9^{4-}$  (E = Sn, Pb) and  $\text{E}_7^{3-}$  (E = Sb, Bi),  $\text{E}_5^{3-}$  (E = As, Bi), and  $\text{E}_3^{3-}$  (E = As, Sb, and Bi).<sup>63-65</sup> Due to his extensive studies on the synthesis, characterization and the properties of these highly charged polyanions, they are named as “Zintl ions”. Kummer and Diehl reported the first single crystal X-ray structure of polyatomic main group cluster,  $\text{Na}_4(\text{en})_7\text{Sn}_9$ , which had a  $\text{Sn}_9^{4-}$  anion thus confirming the existence of Zintl ions.<sup>66</sup>

In 1976, Corbett and co-workers reported the use of a macrocyclic ligand, 4, 7, 13, 16, 21, 24-Hexaoxa-1,10-diazobicyclo [8,8,8] hexacosane (referred as 2,2,2-crypt) as a sequestering agent for the alkali metal cations of the binary alloys.<sup>67</sup> 2,2,2-crypt increases solubility of alkali metals by breaking the ion pairing of the alkali metal / Zintl ion alloys to enhance the crystallization of the Zintl ions. Various Group 14 and Group 15 Zintl salts and naked metal clusters were subsequently isolated such as  $\text{E}_9^{4-}$  (E = Sn<sup>68, 69</sup>, Ge<sup>70, 71</sup>, Pb<sup>72</sup>),  $\text{Ge}_9^{2-}$ ,<sup>73</sup>  $\text{E}_7^{3-}$  (E = P<sup>74, 75</sup>, As<sup>76</sup>, Sb.<sup>67, 77</sup>).

The pnicogen (group 15) Zintl ions tend to form polycyclic hydrocarbon-like structures such as nortricyclane  $\text{E}_7^{3-}$  (E = P, As, Sb). The hydrocarbon analogy resides in the fact that E and  $\text{E}^-$  (E = P, As) are electronically equivalent to CH and  $\text{CH}_2$ , respectively. In contrast to the electron precise group 15 polyatomic anions, the

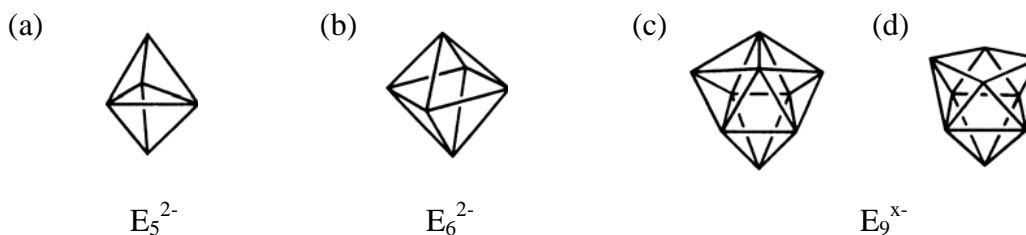


**Figure 1.2.** Structures of soluble homoatomic Group 14 anions a)  $[E_5]^{2-}$ , E = Ge, Sn, Pb; b)  $[E_6]^{2-}$  in  $[\{E-Cr(CO)_5\}_6]^{2-}$  with E = Ge, Sn; c,d)  $[E_9]^x$  (E = Si-Pb, x = 3,4) (taken from reference <sup>78</sup>).

group 14 Zintl ions form electron deficient, boron-hydride-like structures such as  $E_5^{2-}$ <sup>79, 80</sup> (Figure 1.1a) and  $E_9^{3-}$ <sup>81-83</sup> (E = Ge, Sn, Pb) (Figure 1.1c). Most commonly, the group 14 Zintl ions form deltahedral-like, nine atom clusters such as  $E_9^{4-}$  ion (E = Sn, Pb, Ge) in the solution and in the solid state. These clusters usually crystallize in distorted, monocapped square antiprisms ( $C_{4v}$ ) (Figure 1.1d) and tricapped trigonal prisms ( $D_{3h}$ ) (Figure 1.1c).<sup>78</sup> The  $C_{4v} \leftrightarrow C_{2v} \leftrightarrow D_{3h}$  interconversion was proposed by Corbet et al.<sup>69, 78, 84</sup>. The exchange mechanism involves bond formation across the open face of the cluster, followed by bond breaking.

Rudolph and co-workers investigated solution dynamics of nido- $Sn_9^{4-}$  cluster by means of  $^{119}Sn$  NMR spectroscopy.<sup>85</sup> Their studies showed that even though a  $C_{4v}$  type structure of the  $Sn_9^{4-}$  cluster has three distinct chemical environments of Sn atoms, a single resonance is observed in  $^{119}Sn$  NMR spectra. This indicates nido- $Sn_9^{4-}$  is highly fluxional in solution and Sn atoms in the cluster are in rapid exchange on the NMR time scale. The observation of  $^{119}Sn$ - $^{117}Sn$  satellites and their magnitude relative to the single resonance shows that the exchange process is intramolecular. Rudolph's study provides valuable insight into nuclearity of the cluster.

Similar to the borohydrides, in the case of electron deficiency, the elements could form either homoatomic multiple bonds or two-electrons-more-centers bonds. Due to the higher coordination number requirement, the latter is more common for heavier members of Group 14 which form stable, naked, ligand-free anions. Delocalized electrons are responsible for bonding within the deltahedral clusters; therefore, Wade-Mingos Rules are used for electron counting rather than the octet rule.<sup>86</sup> The Wade's rules introduced the terminology of *closo*, *nido*, *aracno* and *hypo* deltahedra to describe the structure of the cluster according to the number of vertex and overall charge of the cluster. For example, the  $E_9^{4-}$  has a *nido* structure,  $2n+4$  type ( $n$  = number of cluster atoms), with 9 vertices and 22 cluster electrons. On the other hand, the  $E_9^{2-}$  has 20 skeletal electrons, 9 vertices, thus the cluster is defined as a  $2n+2$  type and a *closo* geometry.

Extensive studies were performed on the group 14 Zintl ions lead to formation of various clusters with distinct structures. The first dimer of the deltahedral Zintl ions have been reported by Sevov *et al.*<sup>87</sup> The  $[(Ge_9)_2]^{6-}$  dimer is prepared by oxidative coupling of  $Ge_9^{4-}$  deltahedra. It contains two monocapped square antiprismatic  $Ge_9$  clusters that are bonded via two-center-two-electron exo-bond between the vertices in the open squares.  $[(Ge_9)_3]^{6-}$  trimer<sup>88</sup>,  $[(Ge_9)_4]^{8-}$  tetramer<sup>89</sup> have also been prepared with similar fashion. They have nine atom germanium clusters connected with two exo-bonds to each other.

Redox reactions of nine-atom deltahedral Zintl anions have also made it possible to form polymers. Guloy *et al.*<sup>90, 91</sup> prepared polymeric chains of the  $Ge_9$  units.  $_{1\infty}[(Ge_9)^{2-}]$  polymer is formed by oxidative coupling of *nido*- $Ge_9$  clusters, which

are exo-bonded to each other with 2-center 2-electron bonds. Fassler *et al.* also prepared polymers of Ge<sub>9</sub> clusters,  $_{1\infty}[\text{HgGe}_9]^{2-}$ .<sup>92</sup> The polymeric chain contains the Ge<sub>9</sub> clusters connected via Hg atoms. Each Hg atom is connected to two Ge atoms of open rectangular face of the Ge<sub>9</sub> cluster positioned opposite to each other.

The isolation of the dimers, trimers, tetramers and polymers showed the potential preparation of nanomaterials with various sizes by controlled cluster growth. The success of functionalizing clusters with each other indicated the possibility of exo-bonding other main-group substituents to the deltahedral Zintl ions. Similar redox reactions have been used to prepare  $[\text{Ph}_2\text{Bi-Ge}_9\text{-BiPh}_2]^{2-}$ , which is the first example of such complexes.<sup>88</sup> It has two BiPh<sub>2</sub> exo-bonded to two opposite vertices of the open face of the Ge<sub>9</sub> cluster.

Ligand free, Group 14 polyhedra have been studied extensively due to their simplicity and high reactivity. They react with transition metals to form the transition metal / group 14 Zintl anions. One hundred years after the study of Joannis, Haushalter *et al.* structurally characterized the first transition metal-plumbide cluster,  $[\text{Pb}_9\text{Cr}(\text{CO})_3]^{4-}$ .<sup>79</sup>  $[\eta^4\text{-E}_9\text{Cr}(\text{CO})_3]^{4-}$  anions<sup>93</sup> (E = Pb, Sn) have capping Cr(CO)<sub>3</sub> unit on the open face of the E<sub>9</sub> cluster resulting *closo* geometry. Eichhorn *et al.* have reported the solution dynamics of the *closo*- $[\text{Sn}_9\text{M}(\text{CO})_3]^{4-}$  where M = Cr, Mo, W as well as their synthesis, structures and properties.<sup>94</sup> They described the new isomeric form of the anions and showed equilibrium between  $\eta^4$  and  $\eta^5$  isomers by the way of data from <sup>13</sup>C and <sup>119</sup>Sn NMR spectroscopy.

Further studies have showed that nine-atom cluster can accommodate a central transition metal. Eichhorn *et al.* have prepared  $[\text{Sn}_9\text{Pt}_2(\text{PPh}_3)]^{2-}$ <sup>95</sup> and  $[\text{Sn}_9\text{Ni}_2(\text{CO})]^{3-}$

Zintl anions. They contain ligated transition metal fragments, Pt(PPh<sub>3</sub>) and Ni(CO), incorporated into the transition metal centered anion frameworks as a vertex of the cluster. Although the Pt centered anion has a highly distorted Sn<sub>9</sub> cluster, the Ni centered one possesses an undistorted, C<sub>4v</sub> *closo* structure. Besides the synthesis, structures and characterization, solution dynamics of [Sn<sub>9</sub>Pt<sub>2</sub>(PPh<sub>3</sub>)]<sup>2-</sup> anion were studied by <sup>31</sup>P and <sup>119</sup>Sn NMR spectroscopy. It has been shown that Sn<sub>9</sub> cluster is highly fluxional, on the other hand Pt-Pt-PPh<sub>3</sub> unit remains intact and it is not in exchange on the NMR time scale. [Sn<sub>9</sub>Ni<sub>2</sub>(CO)]<sup>3-</sup> is a rare example of a paramagnetic Zintl ion complex. Due to its paramagnetic nature, the dynamic behavior of this complex could not be reported.

New group 14 Zintl ions, having frameworks other than E<sub>9</sub> cluster, are also stabilized by transition metals. Huttner *et al.* reported octahedral E<sub>6</sub><sup>2-</sup> unit in *closo*-[E<sub>6</sub>{M(CO)<sub>5</sub>}<sub>6</sub>]<sup>2-</sup> (E = Sn, Ge) and (M = Cr, Mo, W)<sup>96, 97</sup>. These complexes were prepared from the reduction of EX<sub>2</sub> (GeI<sub>2</sub>, SnCl<sub>2</sub>) with M<sub>2</sub>(CO)<sub>10</sub><sup>2-</sup> (M = Cr, Mo, W) in THF solutions. Studies by Eichhorn *et al.* showed that cyclohexane-like Sn<sub>6</sub><sup>12-</sup> Zintl ion exists in the *closo*-[Sn<sub>6</sub>{Nb(tol)}<sub>2</sub>]<sup>2-</sup> anion. Six-membered ring of tin atoms in a chair cyclohexane conformation stabilized by two Nb(tol) fragments, forming distorted cube with the two Nb atoms at opposite corners.<sup>56</sup>

The metal stabilized group 14 Zintl ions have become an active research area due to their potential application in the preparation of catalytically active binary alloys and nanomaterials.<sup>84, 98</sup> It has been a desire to prepare ligand free transition metal / main group binary anions to enhance the catalytic activity. Recent studies have shown that employing metal precursors with more labile ligands is the most

efficient way to prepare ligand-free transition metal / Zintl ion clusters. Although extensive theoretical studies have been reported on the metallated Zintl ions, very few structural data have been reported. Sevov *et al.*<sup>99</sup> succeeded in preparing a ligand-free, eighteen atom single-cage deltahedron of germanium atoms, centered by dimer of palladium atoms.  $[\text{Pd}_2@\text{Ge}_{18}]^{4-}$  is made of two nine-atom germanium clusters, forming oblong shape 18-vertex deltahedron. Subsequently, clusters of eighteen Ge atoms enclosing trimer of Ni atoms have been prepared.<sup>100</sup> The ligand-free anion,  $[\text{Ni}_3\text{Ge}_{18}]^{4-}$ , contains two Ni centered  $\text{Ge}_9$  clusters connected by a central Ni atom which plays a role as both inversion center and vertex for each cluster.

## 1.5. Overview of the Thesis

In the following chapters of this thesis, the syntheses and characterizations of variety of new transition metal stabilized Group 14 Zintl ion clusters with few or no ligands are presented. Their unique structural properties, unusual spectroscopic and electronic properties are discussed.

Chapter 2 presents the *first isolated* free-standing centered icosahedra,  $[\text{M}@\text{Pb}_{12}]^{2-}$  (M = Pt, Pd, Ni), without any attendant ligands. The chapter also presents the first experimental measure of the  $\sigma$ -aromaticity for the centered icosahedral clusters by way of  $^{207}\text{Pb}$  NMR analysis. The characterization and dynamic behavior of this new type of Zintl ion,  $[\text{Ni}@\text{Pb}_{10}]^{2-}$ , are described in Chapter 3. It is a rare example of the endohedral naked metal clusters and represents highly fluxional dynamic behavior on NMR time scale. Chapter 4 discusses synthesis, structure and surprising dynamic properties of two focus Zintl ion cluster,  $[\text{Ni}_2\text{Sn}_{17}]^{4-}$ . Chapter 5

presents the synthesis and characterization of the  $[\text{Ni}_6\text{Ge}_{13}(\text{CO})_5]^{4-}$  and  $[\text{Ge}_9\text{Ni}_2(\text{PPh}_3)]^{2-}$  Zintl ion clusters. The chapter also describes interconversion of these complexes and their relationships to other transition metal group 14 Zintl complexes.

## Chapter 2

### $[\text{M}@\text{Pb}_{12}]^{2-}$ (M = Pt, Pd, Ni)

#### 2.1. Introduction

The discovery of the celebrated  $\text{C}_{60}$ -fullerene triggered an interest in preparing new nanomaterials from small, high symmetry molecular clusters such as icosahedral clusters. The geometric definition of an icosahedron is a regular polyhedron possesses  $I_h$  point symmetry and comprises 12 vertices and 20 equilateral triangle faces. The icosahedral clusters of atoms are relatively common<sup>101</sup> among organometallic complexes,<sup>102-104</sup> inorganic clusters,<sup>105-108</sup> boranes and carboranes,<sup>109-111</sup> intermetallics and other solid state materials.<sup>112-114</sup> However, homoatomic naked icosahedral clusters are relatively rare, and especially the ones with perfect  $I_h$  point symmetry are quite sparse. One of the well-known icosahedra is the free-standing non-centered,  $\text{B}_{12}\text{H}_{12}^{2-}$ .<sup>115</sup> The  $\text{Tl}_{13}^{11-}$  and  $\text{Tl}_{12}\text{Cd}^{12-}$  are examples of centered, symmetrical homoleptic icosahedra found in solid state compounds.<sup>112, 114, 116</sup> Other structurally characterized clusters with  $I_h$  point symmetry include dodecahedrane ( $\text{C}_{20}\text{H}_{20}$ ),<sup>117</sup>  $\text{C}_{60}$  and its derivatives,<sup>118, 119</sup> and  $[\text{As}@\text{Ni}_{12}@\text{As}_{20}]^{3-}$ .<sup>57</sup>

The centered icosahedra ( $\text{M}_{13}$ ) are particularly interesting as being the smallest member of the growth sequence of the full-shell, ‘magic number’ clusters.

They serve as a nucleation site for nanoparticle growth by successive accumulation of layers around.<sup>25</sup> The two prominent ligand stabilized nano-size clusters,  $[\text{Au}_{55}(\text{PPh}_3)_{12}\text{Cl}_6]$  and  $[\text{Pd}_{145}(\text{CO})_{60}(\text{PEt}_3)_{30}]$  are constructed on centered icosahedra as a template.<sup>120, 121</sup>  $\text{Al}_{13}^-$  ( $\text{Al}@\text{Al}_{12}^-$ ) is one of the most famous magic number clusters, which is identified in gas phase.<sup>122</sup> Another example is recently reported, Pb-based  $\text{Al}@\text{Pb}_{12}^+$ , which could not be isolated in condensed phase.<sup>39</sup> A variety of other centered icosahedral clusters have been studied theoretically to explore their stability and electronic properties.<sup>31, 33, 123</sup> However, only some gas phase studies suggest their existence, and very few structural data have been reported.<sup>33, 34, 37, 38</sup>

Here, the synthesis, structure and properties of free standing, naked  $\text{Pb}_{12}$  icosahedral clusters encapsulating Group 10 transition metals are presented.  $[\text{M}@\text{Pb}_{12}]^{2-}$  ( $\text{M} = \text{Pt}, \text{Pd}, \text{Ni}$ ) ions comprise a metal centered *closo*- $[\text{Pb}_{12}]^{2-}$  icosahedral Zintl ion and possess virtual  $I_h$  point symmetry. The anions are the *first isolated* free-standing ligand free centered icosahedral clusters. They have the  $\text{M}_{13}$  type structure, smallest possible subunit in nanoparticle growth, and are models for core-shell structures without any interference of ligands.

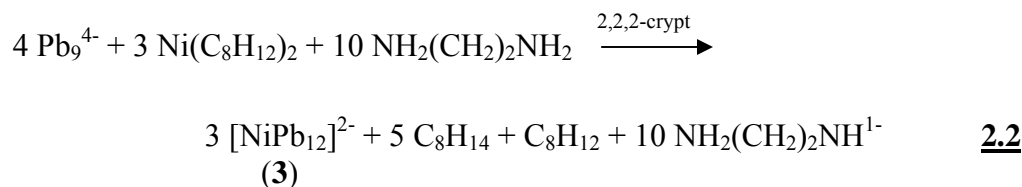
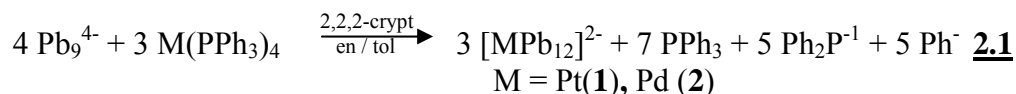
## 2.2. Results

### 2.2.1. Synthesis

Ethylenediamine (en) solutions of  $\text{K}_4\text{Pb}_9$  react with toluene solutions of  $\text{ML}_4$  ( $\text{M} = \text{Pt}, \text{Pd}, \text{L} = \text{PPh}_3; \text{M} = \text{Ni}, \text{L}_2 = \text{COD}$ ) in the presence of 4 equivalence of 2,2,2-crypt to give  $[\text{M}@\text{Pb}_{12}]^{2-}$  cluster anions ( $\text{M} = \text{Pt}$  (**1**),  $\text{Pd}$  (**2**),  $\text{Ni}$  (**3**)) as the  $[\text{K}(2,2,2\text{-crypt})]^+$  salts. The salts have been characterized by single crystal XRD, energy

dispersive X-Ray (EDX) analysis,  $^{207}\text{Pb}$  NMR,  $^{195}\text{Pt}$  NMR (for anion **1**) and laser desorption/ionization-time-of-flight mass spectrometry (LDI-TOF MS).

The formation of the cluster anions requires a net oxidation of the starting materials that is accompanied by a reduction of the displaced ligands as shown in eq 1 and 2.



In reaction **2.1**, the phenyl and  $\text{Ph}_2\text{P}^{1-}$  byproducts were identified by GC-MS and  $^{31}\text{P}$  NMR studies, respectively. The reductive decomposition of the  $\text{PPh}_3$  ligand is directly analogous to the well-known reductive cleavage of  $\text{PPh}_3$  by alkali metals to give alkali- $\text{PPh}_2$  salts and biphenyl.<sup>124</sup> For reaction **2.2**, the en solvent molecules are reduced with the formal generation of  $\text{H}_2$  and  $\text{NH}_2(\text{CH}_2)_2\text{NH}^{1-}$  ions. The eliminated equivalents of  $\text{H}_2$  are effectively trapped through the hydrogenation of COD to form cyclooctene, which was identified in the reaction mixture by GC-MS analysis. The  $[\text{Ni@Pb}_{10}]^{2-}$  forms competitively with the  $[\text{Ni@Pb}_{12}]^{2-}$ , but the former is described as in the following chapter. The crystals of both salts are very similar in appearance (thin red-brown plates) and difficult to differentiate in the solid state. Product ratios were estimated from  $^{207}\text{Pb}$  NMR analysis. Attempts to exchange the central metal

atom of the three icosahedra were unsuccessful. The  $^{207}\text{Pb}$  NMR spectroscopy was used to monitor the experiments, and it is not clear the identity of the product after the reaction.

### 2.2.2. Solid State Structure

Each of the crystal unit cells contains a non-interacting  $[\text{M}@\text{Pb}_{12}]^{2-}$  ( $\text{M} = \text{Pt}$ ,  $\text{Pd}$ ,  $\text{Ni}$ ) anion with two  $[\text{K}(2,2,2\text{-crypt})]^+$  cations. There are solvent molecules in the crystal lattice of the anion **2** and **3**, and there is no significant interaction of them with the anions. The  $[\text{K}(2,2,2\text{-crypt})]_2[\text{Pt}@\text{Pb}_{12}]$  salt belongs to the trigonal space group  $\text{P}\bar{3}$ , and is surprisingly devoid of disorder. Both the  $\text{Pt}@\text{Pb}_{12}^{2-}$  anion and the  $[\text{K}(2,2,2\text{-crypt})]^+$  cations have crystallographically-imposed 3-fold symmetry and reside on  $\bar{3}$  inversion and 3-fold rotation axes, respectively. (Figure 2.1) The  $[\text{K}(2,2,2\text{-crypt})]_2[\text{M}@\text{Pb}_{12}] \cdot \text{solvent}$  salts ( $\text{M} = \text{Pd}$  and  $\text{Ni}$ , solvent = toluene and ethylenediamine, respectively) crystallize in the triclinic space group  $\text{P}\bar{1}$  but are not

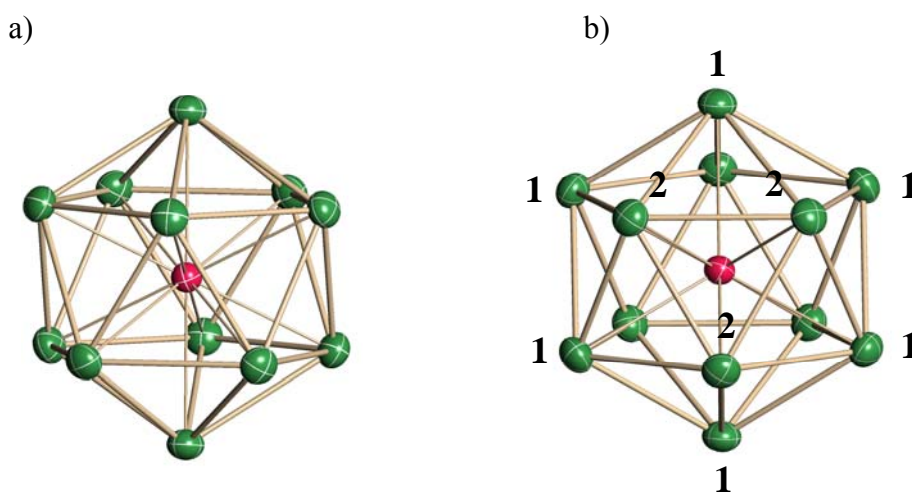


**Figure 2.1.** ORTEP drawings of the  $[\text{Pt}@\text{Pb}_{12}]^{2-}$  ion showing a) the icosahedral structure and b) a view down the  $\bar{3}$  axis. Pt is red, Pb is green, thermal ellipsoids are set at the 50% probability level.

isomorphous. The three anions are well ordered in the crystal lattices. Summaries of the crystallographic data and selected bond distances and angles for the three clusters are given in Table 2.1, Table 2.2, and Table 2.3, respectively.

The  $[M@Pb_{12}]^{2-}$  anions have twelve surface Pb atoms that form an icosahedral cage encapsulating the transition metal (Pt, Pd, Ni) at the center. (Figure 2.2) The anions possess virtual molecular  $I_h$  point symmetry, though the structures of Pd and Ni centered anions are slightly distorted from their ideal symmetry. The Pt atom is placed in the equivalent distance from all Pb atoms which form a highly symmetric icosahedron. For anion **2**, the Pd metal resides on the inversion center of the icosahedron. On the other hand, Ni atom sits on the general position and does not have symmetry. The Pb-Pb contacts for all three anions are in agreement with the ones reported from polyplumbide clusters  $MPb_9(CO)_3^{4-}$  ( $M = Cr, Mo, W$ )<sup>79, 125</sup>  $Pb_9^{4-}$ <sup>126</sup>  $Pb_9^{3-}$ <sup>82</sup> and  $Pb_5^{2-}$ <sup>127</sup>, where the distances vary between 3.03 Å and 3.41 Å. To our knowledge, there is no similar Pt, Pd and Ni compound reported in the literature

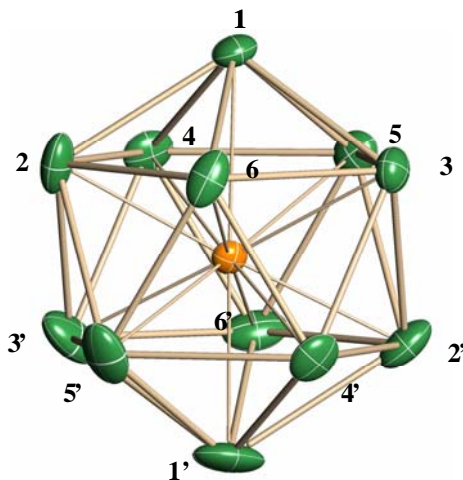


**Figure 2.2.** ORTEP drawing of fully labeled  $[M@Pb_{12}]^{2-}$  ( $M=Pt, Pd, Ni$ ) anions showing the icosahedral structure. Thermal ellipsoids are set at the 50% probability level.

**Table 2.1.** Crystallographic data for the  $[M@Pb_{12}]^{2-}$  (M = Pt, Pd, Ni) ions.

	[PtPb <sub>12</sub> ]	[PdPb <sub>12</sub> ]	[NiPb <sub>12</sub> ]
	[K(2,2,2-crypt)] <sub>2</sub>	[K(2,2,2-crypt)] <sub>2</sub> •tol	[K(2,2,2-crypt)] <sub>2</sub> •en
Empirical formula	PtPb <sub>12</sub> C <sub>36</sub> H <sub>72</sub> K <sub>2</sub> N <sub>4</sub> O <sub>12</sub>	PdPb <sub>12</sub> C <sub>43</sub> H <sub>80</sub> K <sub>2</sub> N <sub>4</sub> O <sub>12</sub>	NiPb <sub>12</sub> C <sub>38</sub> H <sub>80</sub> K <sub>2</sub> N <sub>6</sub> O <sub>12</sub>
Formula weight	3512.55	3515.99	3436.17
Temperature (K)	173(2)	173(2)	173(2)
Wavelength (Å)	0.71073	0.71073	0.71073
Crystal system	Trigonal	Triclinic	Triclinic
Space group	P-3	P-1	P-1
Unit cell dimensions			
a (Å)	13.041(6)	13.5900(11)	14.566(4)
b (Å)	13.041(6)	13.9389(11)	15.469(5)
c (Å)	11.672(11)	22.1236(17)	16.400(5)
α (deg)	90	72.1144(15)	62.914(5)
β (deg)	90	85.2884(16)	64.289(5)
γ (deg)	120	64.1532(15)	87.127(5)
volume (Å <sup>3</sup> )	1719.1(19)	3582.8(5)	2913.8(15)
Z	1	2	2
D <sub>calc</sub> (Mg/m <sup>3</sup> )	3.393	3.259	2.427
Abs coeff (mm <sup>-1</sup> )	31.448	28.485	17.622
Crystal size (mm)	0.15×0.09×0.07	0.25×0.09×0.002	0.35×0.09×0.01
Reflections collected	11000	17417	16141
Independent reflections	2022 [R(int) = 0.0839]	17424 [R(int) = 0.0000]	16144 [R(int) = 0.0000]
Goodness of fit on F <sup>2</sup>	1.055	0.996	1.013
Final R indices [ <i>I</i> > 2σ( <i>I</i> )] <sup>a</sup>			
R1	0.0352	0.0596	0.1199
wR2	0.0825	0.1560	0.2976
R indices (all data) <sup>a</sup>			
R1	0.0730	0.1014	0.2025
wR2	0.0959	0.1671	0.3289

a. The function minimized during the full-matrix least-squares refinement was  $\sum w(F_o2 - F_c2)$  where  $w = 1/[\sigma^2(F_o2) + (0.0380 * P)^2 + 5.4664 * P]$  and  $P = \max(F_o2, 0) + (2 * F_c2) / 3$ .

**Table 2.2.** Selected bond lengths [Å] for [M@Pb<sub>12</sub>] [K(2,2,2-crypt)]<sub>2</sub> (M = Ni, Pd, Pt).

<b>M</b>	<b>Pt</b>	<b>Pd</b>	<b>Ni</b>
M-Pb(1)	3.056(2)	3.076(2)	3.033(2)
M-Pb(1')	3.056(2)	3.004(2)	3.033(2)
M-Pb(2)	3.056(2)	3.092(2)	2.982(2)
M-Pb(2')	3.056(2)	3.021(2)	2.982(2)
M-Pb(3)	3.056(2)	3.034(2)	2.999(2)
M-Pb(3')	3.056(2)	3.038(2)	2.999(2)
M-Pb(4)	3.060(2)	3.038(2)	2.957(2)
M-Pb(4')	3.060(2)	3.010(2)	2.957(2)
M-Pb(5)	3.060(2)	3.014(2)	2.923(3)
M-Pb(5')	3.060(2)	3.023(2)	2.923(3)
M-Pb(6)	3.060(2)	3.071(2)	2.992(2)
M-Pb(6')	3.060(2)	2.980(2)	2.992(2)
Pb(1)-Pb(2)	3.222(2)	3.163(1)	3.185(3)
Pb(1)-Pb(3)	3.206(2)	3.204(1)	3.143(4)
Pb(1)-Pb(4)	3.206(2)	3.188(1)	3.118(3)
Pb(1')-Pb(5')	3.210(2)	3.185(2)	3.050(4)
Pb(1')-Pb(6')	3.234(2)	3.135(2)	3.194(3)
Pb(5)-Pb(3)	3.234(2)	3.165(2)	3.019(4)
Pb(5)-Pb(4)	3.222(2)	3.174(1)	3.097(4)
Pb(5)-Pb(2')	3.205(2)	3.204(2)	3.148(2)
Pb(5)-Pb(6')	3.205(2)	3.206(2)	3.127(4)

**Table 2.3.** Selected bond angles [°] for [M@Pb<sub>12</sub>] [K(2,2,2-crypt)]<sub>2</sub> (M = Pt, Pd, Ni).

Metal (M)	Pb-M-Pb			Pb-Pb-Pb		
	Average (Å)	Range (Å)	Variance (σ <sup>2</sup> ) <sup>a</sup>	Average (Å)	Range (Å)	Variance (σ <sup>2</sup> ) <sup>a</sup>
Pt	63.44	0.68	0.07	60.00	1.02	0.11
	116.56	0.68	0.07	108.00	1.08	0.11
	180.00	0	0	-	-	-
Pd	63.44	2.98	0.51	60.00	2.17	0.24
	116.56	3.44	1.08	108.00	2.70	0.35
	178.48	0.97	0.13	-	-	-
Ni	63.44	9.40	4.22	60.00	10.80	4.70
	116.56	9.50	4.21	107.98	12.20	2.05
	180.00	0	0	-	-	-
<b>Perfect Icosahedron</b>						
	63.44			60.00		
	116.57			108.00		
	180.00					

$$^a \text{variance is defined as: } \sigma^2 = \left[ \sum_{i=1}^N (x_i - \bar{x})^2 \right] / (N-1)$$

**Table 2.4.** Diagonal and Pb-M, Pb-Pb distances of the [M@Pb<sub>12</sub>]<sup>2-</sup> (M = Pt, Pd, Ni) anions.

Metal (M)	Covalent Radii of M (Å)	Diagonal dist. (avg (Å))	Pb-M distances			Pb-Pb distances		
			Average (Å)	Range (Å)	Variance (σ <sup>2</sup> x10 <sup>3</sup> )	Average (Å)	Range (Å)	Variance (σ <sup>2</sup> x10 <sup>3</sup> )
Pt	1.29	6.116(6)	3.058(7)	0.003	0.0044	3.216(12)	0.028	0.14
Pd	1.28	6.067(5)	3.033(7)	0.112	1.1	3.189(9)	0.080	0.33
Ni	1.15	5.983(4)	3.001(24)	0.112	1.3	3.078(9)	0.214	3.1

which could be used for comparison of the Pb-M bond distances. The [M@Pb<sub>12</sub>]<sup>2-</sup> clusters are 12-vertex 26-electron polyhedron with a highly-regular *closo* icosahedral structure as expected from a Wade-Mingos analysis<sup>86</sup> In this analysis, the Pb atoms donate two electrons and Pt, Pd and Ni atoms donate zero electrons to the cluster bonding, that give 26-electron, 2n+2 clusters with *closo* geometries when the -2

charge is taken into consideration. The alternative way to count the cluster electrons is the topological electron count theory, introduced by B. Teo.<sup>128</sup> The number of skeletal electron pairs are determined by the equation,  $B = N/2 - (V_n + 6V_m)$ , where  $N$  is number of total cluster valence electrons,  $V_n$  is number of surface main group atoms and  $V_m$  is number of surface transition metal atoms. For the anions **1**, **2** and **3**,  $N = 10 e^-$  (Pt, Pd or Ni) +  $12 \times 4 e^-$  (Pb) +  $2 e^-$  (charge) =  $60 e^-$ . Therefore,  $B = 60/2 - (12 + 6 \times 0) = 18$  pair  $e^-$ , which is considered as characteristic of electron rich icosahedral clusters and common for transition metal centered icosahedral clusters.<sup>128</sup>

The bond distances of the anions **1**, **2**, and **3** change according to the atomic radius of the center atom. As the radius of the center atom gets smaller, The Pb-Pb, Pb-M and diagonal distances of the icosahedra decrease as expected, and the cluster gets distorted. The relative distortion of the icosahedra can be judged by the distribution of the Pb-Pb and Pb-M bond distances and variance. The range and variance along with the average bond distances of Pb-Pb, and Pb-M contacts for all three anions are summarized in Table 2.4. As an indication of almost perfect symmetry, the anion **1** has a very narrow Pb-Pb bond distance range with remarkably small variance ( $1.4 \times 10^{-4}$ ). However, compared to the anion **1**, the Pb-Pb contacts in the anions **2** and **3** vary in the broader range,  $0.08 \text{ \AA}$  and  $0.214 \text{ \AA}$ , respectively. The variance for the anions **2** and **3** are higher than that of the anion **1**. It is also important to compare the range and variance of Pb-M distances for all the three anions in order to identify potential distortions in the icosahedra. In anion **1**, all of the Pb-Pt bonds are quite symmetrical and equivalent within the experimental error. Compared to the anion **1**, the range of Pb-M separations for the anions **2** and **3** are significantly larger,

0.112 Å. The Pb-Pb and Pb-M bond distance ranges indicate that while the  $[\text{Pt}@\text{Pb}_{12}]^{2-}$  demonstrate almost no distortion, the degree of distortion is higher in  $[\text{Ni}@\text{Pb}_{12}]^{2-}$  than  $[\text{Pd}@\text{Pb}_{12}]^{2-}$ .

### 2.2.3. NMR Spectroscopic Studies

The  $^{207}\text{Pb}$  NMR data of the  $[\text{M}@\text{Pb}_{12}]^{2-}$  (M= Pt, Pd, Ni) are summarized in Table 2.5. The anions have chemical shifts moved significantly downfield when they are compared to other lead clusters such as  $[\text{Ni}@\text{Pb}_{10}]^{2-}$ ,  $[\text{Pb}_9]^{4-}$ , and  $[\text{Pb}_9\text{Mo}(\text{CO})_3]^{4-}$ .<sup>125, 129, 130</sup> The  $^{207}\text{Pb}$  NMR spectrum of the anion **1** shows a singlet at 1780 ppm flanked by Pt satellites ( $^1J_{207\text{Pb}-195\text{Pt}} \approx 3440$  Hz, 34% rel. int.) indicating strong coupling to the central Pt atom. (Figure 2.3a) The  $^{195}\text{Pt}$  NMR spectrum (Table 2.2) contains a single resonance at -4527 ppm with a satellite pattern consistent with coupling to 12 equivalent Pb atoms ( $^1J_{207\text{Pb}-195\text{Pt}} \approx 3440$  Hz, see inset of Figure 2.3 for simulated intensities). Both spectra are consistent with the nuclearity of the cluster and its solid-state structure.

**Table 2.5.** The  $^{207}\text{Pb}$  NMR chemical shifts.

Anions	$\delta$ (ppm)
$[\text{Pt}@\text{Pb}_{12}]^{2-}$	+ 1780
$[\text{Pd}@\text{Pb}_{12}]^{2-}$	+ 1520
$[\text{Ni}@\text{Pb}_{12}]^{2-}$	+ 1167
$[\text{Ni}@\text{Pb}_{10}]^{2-}$	- 996
$[\text{Pb}_9]^{4-}$	- 4098

The  $^{209}\text{Pb}$  NMR spectra for  $[\text{Pd}@\text{Pb}_{12}]^{2-}$  and  $[\text{Ni}@\text{Pb}_{12}]^{2-}$  reveal single, broad resonances at 1520 ppm ( $\Delta\nu_{1/2} = 285$  Hz, at 15 °C) and 1167 ppm ( $\Delta\nu_{1/2} = 240$  Hz, at 25 °C), respectively. (Figure 2.4) In comparison,  $\text{Pb}_9^{4-}$  shows a relatively sharp resonance at -4098 ppm ( $\Delta\nu_{1/2} = 47$  Hz, at 25 °C) under the same conditions (104.7 MHz) due to a fast exchange on the NMR time scale. The measured longitudinal relaxation time ( $T_1$ ) values for the resonances observed in  $^{209}\text{Pb}$  NMR spectra of the anion **1** and **2** are quite short at 1.5 msec, which is over an order of magnitude shorter than the  $T_1$  value of  $\text{Pb}_9^{4-}$  (39.8 msec) under the same conditions (dmf solvent, 11 °C, 107.5 MHz).

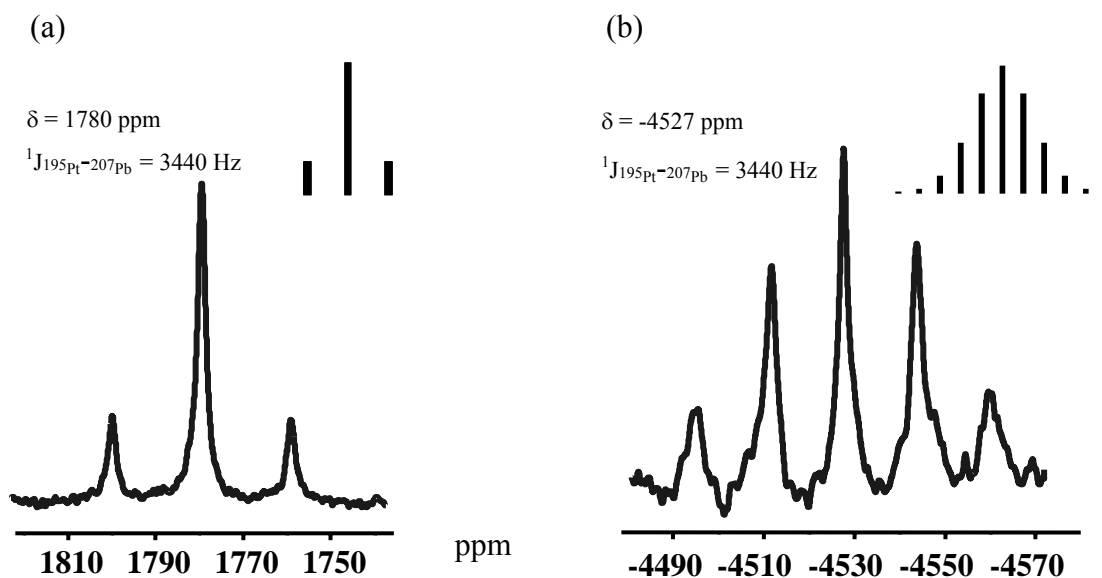


**Figure 2.3.** (a) The  $^{207}\text{Pb}$  NMR spectrum of  $[\text{Pt}@\text{Pb}_{12}]^{2-}$  ion recorded in dmf @ 11 °C and 83.7 MHz., (b) The  $^{195}\text{Pt}$  NMR spectrum of  $[\text{Pt}@\text{Pb}_{12}]^{2-}$  ion recorded in dmf @ 11 °C and 107.5 MHz.

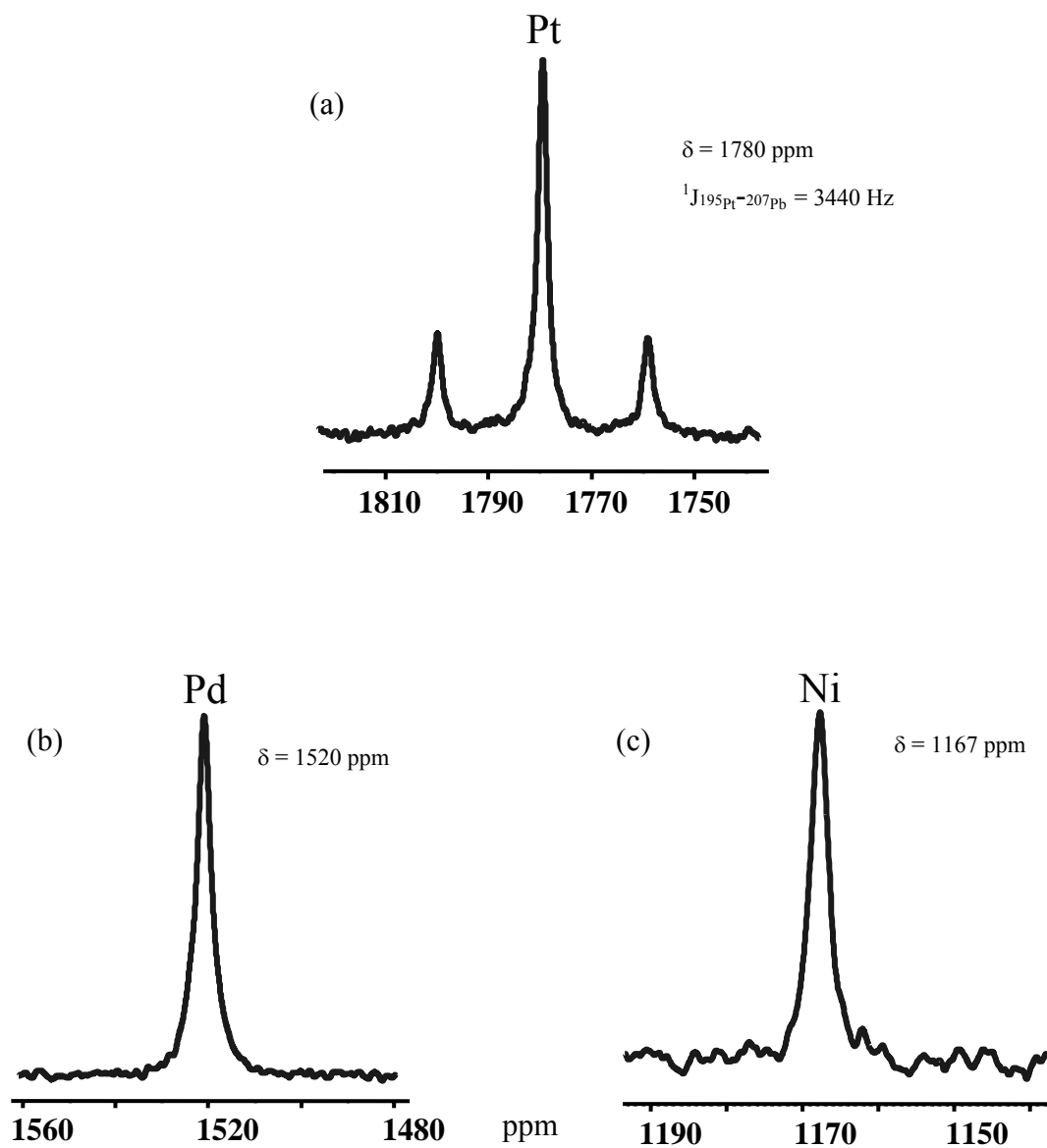


**Figure 2.4.** The  $^{207}\text{Pb}$  NMR spectrum of (a)  $[\text{Pt}@\text{Pb}_{12}]^{2-}$  ion recorded in dmf @ 11 °C and 83.7 MHz., (b)  $[\text{Pd}@\text{Pb}_{12}]^{2-}$  ion recorded in dmf @ 15 °C and 104.7 MHz, (c)  $[\text{Ni}@\text{Pb}_{12}]^{2-}$  ion recorded in dmf @ 25 °C and 104.7 MHz.

#### 2.2.4. Laser Desorption Ionization Time-of-Flight Mass Spectrometry

The laser desorption ionization time-of-flight (LDI-TOF) mass spectra were recorded in the negative ion mode from dried, pure, single crystal samples of the  $[\text{K}(2,2,2\text{-crypt})]_2[\text{M}@\text{Pb}_{12}]$  ( $\text{M} = \text{Pt}, \text{Pd}, \text{Ni}$ ) crystals. The spectrum of  $[\text{K}(2,2,2\text{-crypt})]_2[\text{Pt}@\text{Pb}_{12}]$  crystal is shown in Figure 2.5. The spectra show monoanions of each compound. Similar patterns have been observed for  $[\text{K}(2,2,2\text{-crypt})]_2[\text{M}@\text{Pb}_{12}]$  ( $\text{M} = \text{Pd}, \text{Ni}$ ) crystals. Each of the spectra reveal strong signals of  $[\text{M}@\text{Pb}_{12}]^{1-}$  ( $\text{M} = \text{Pt}, \text{Pd}, \text{Ni}$ ) ions with mass envelopes arising from the multiple isotopes of Pb and M (Figure 2.6). As is common for Zintl clusters,<sup>95, 131</sup> potassium coordinated ion pairs,  $[\text{M}@\text{Pb}_{12}\text{K}]^{1-}$ , appears as a parent ion. The spectra of crystals also show  $[\text{M}@\text{Pb}_{10}]^{1-}$  ions for all three metals as well as their potassium coordinated ion pairs. (Figure 2.7) Although their crystals have not been isolated, they are expected to be isostructural to  $[\text{Ni}@\text{Pb}_{10}]^{2-}$ . The results will be presented in the next chapter.

It is also interesting to identify non-metallated anions,  $[\text{Pb}_{10}]^{1-}$ ,  $[\text{Pb}_{12}]^{1-}$  and their  $\text{K}^+$ -coordinated ion pairs by mass spectroscopy. The anions appear with their spectacular mass envelopes in the spectra for all three compounds. (Figure 2.8) They are most likely fragments of the metallated  $[\text{M}@\text{Pb}_{10}]^-$  and  $[\text{M}@\text{Pb}_{12}]^-$  anions formed during ionization process. Solution stabilities of these gas phase ions are not clear and attempts to prove their existence by way of the  $^{207}\text{Pb}$  NMR spectroscopy were unsuccessful. Even though they are gas phase products, it is surprising to observe these clusters without metal stabilization. To our knowledge, formation of these types of clusters in the gas phase has never been reported.

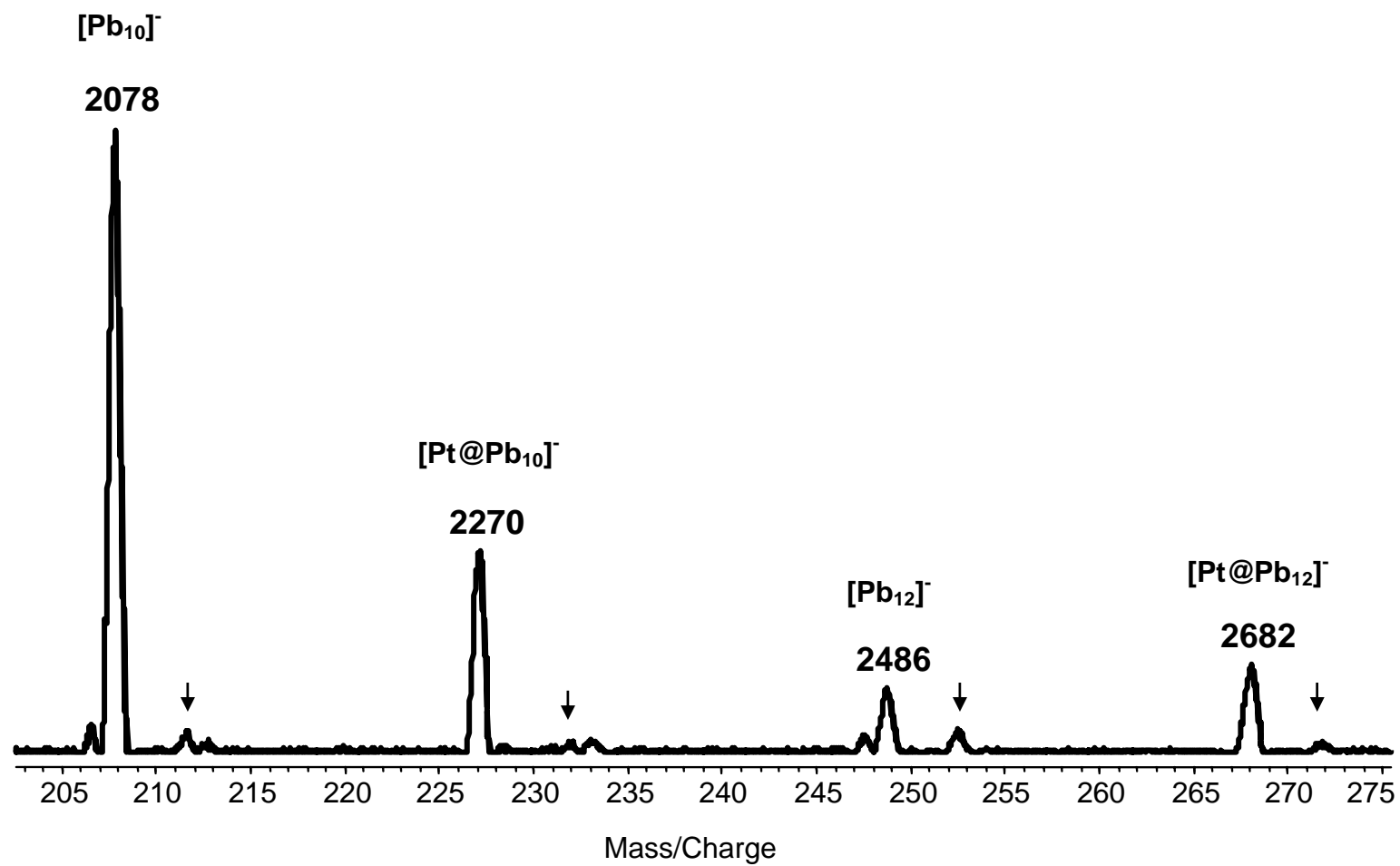


**Figure 2.5.** LDI-TOF mass spectrum of  $[\text{K}(2,2,2\text{-crypt})]_2[\text{Pt}@\text{Pb}_{12}]$  crystals. Arrows denote the potassium coordinated ion pairs.

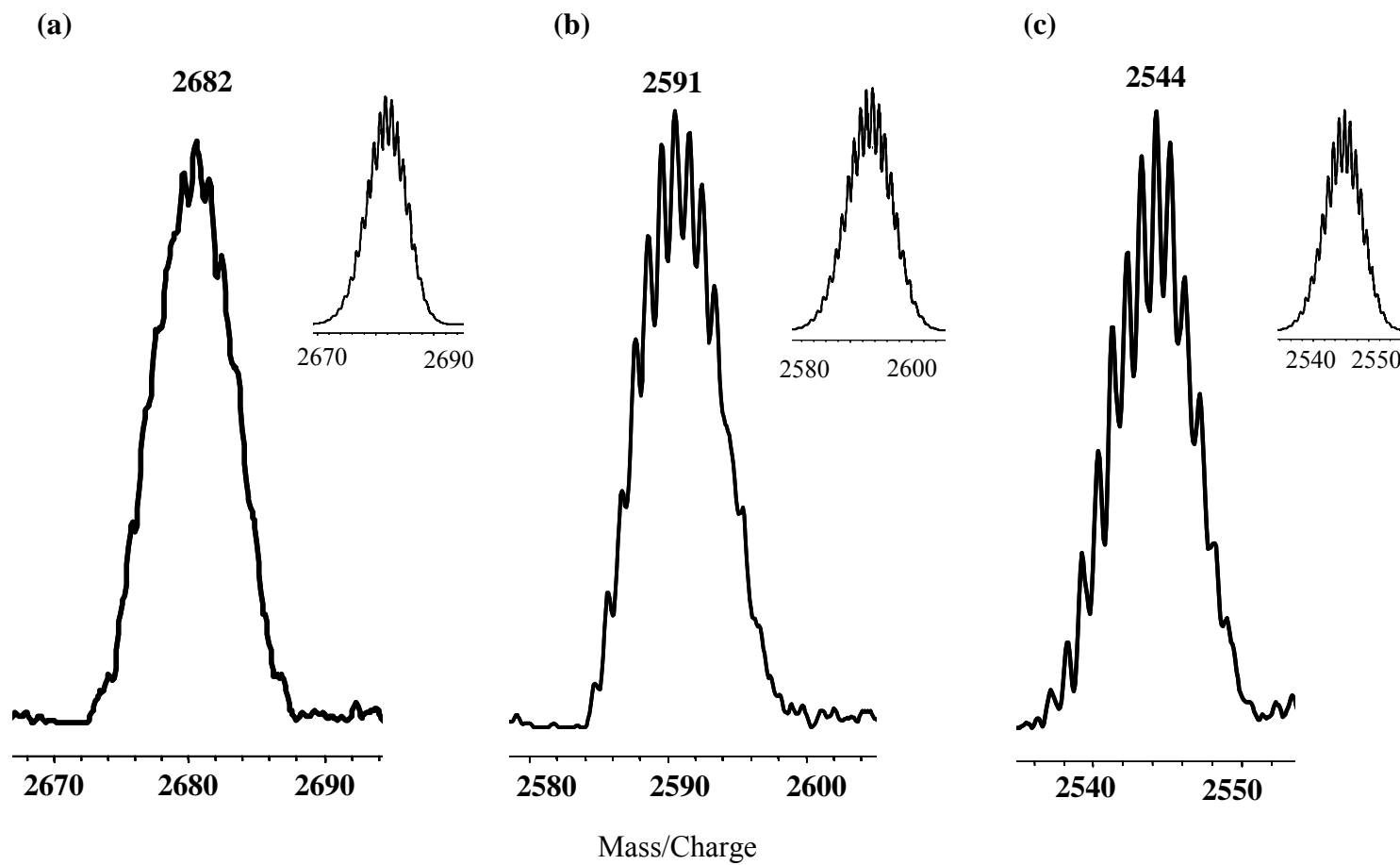


**Figure 2.6.** The LDI-TOF mass spectrum of the (a)  $[\text{Pt}@\text{Pb}_{12}]^{-1}$ , (b)  $[\text{Pd}@\text{Pb}_{12}]^{-1}$ , and (c)  $[\text{Pt}@\text{Pb}_{12}]^{-1}$  ions. The insets show the calculated mass envelope of the corresponding ions.

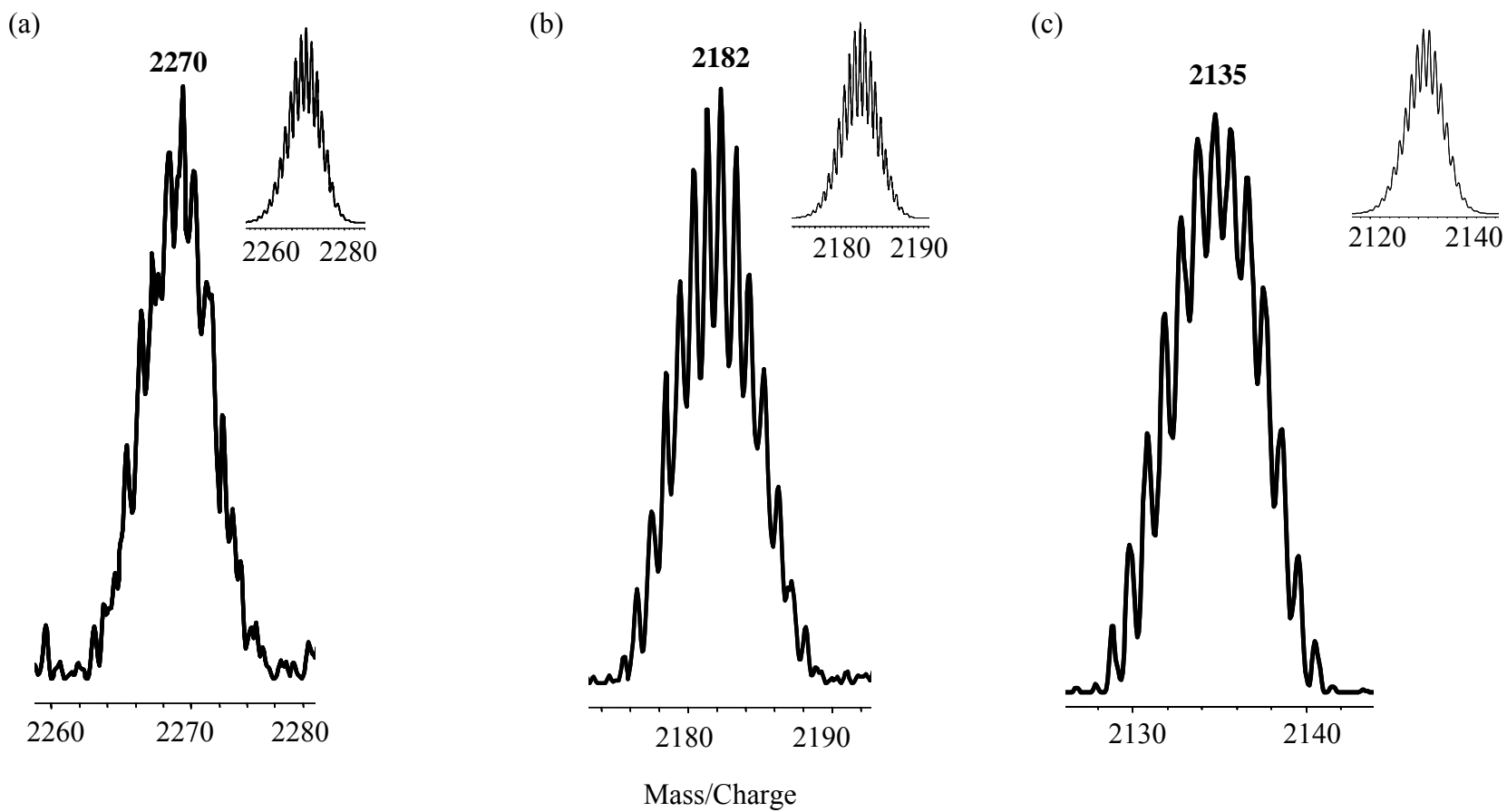


**Figure 2.7.** The LDI-TOF mass spectrum of the (a)  $[\text{Pt}@Pb_{10}]^{-1}$ , (b)  $[\text{Pd}@Pb_{10}]^{-1}$ , and (c)  $[\text{Pt}@Pb_{10}]^{-1}$  ions. The insets show the calculated mass envelope of the corresponding ions.

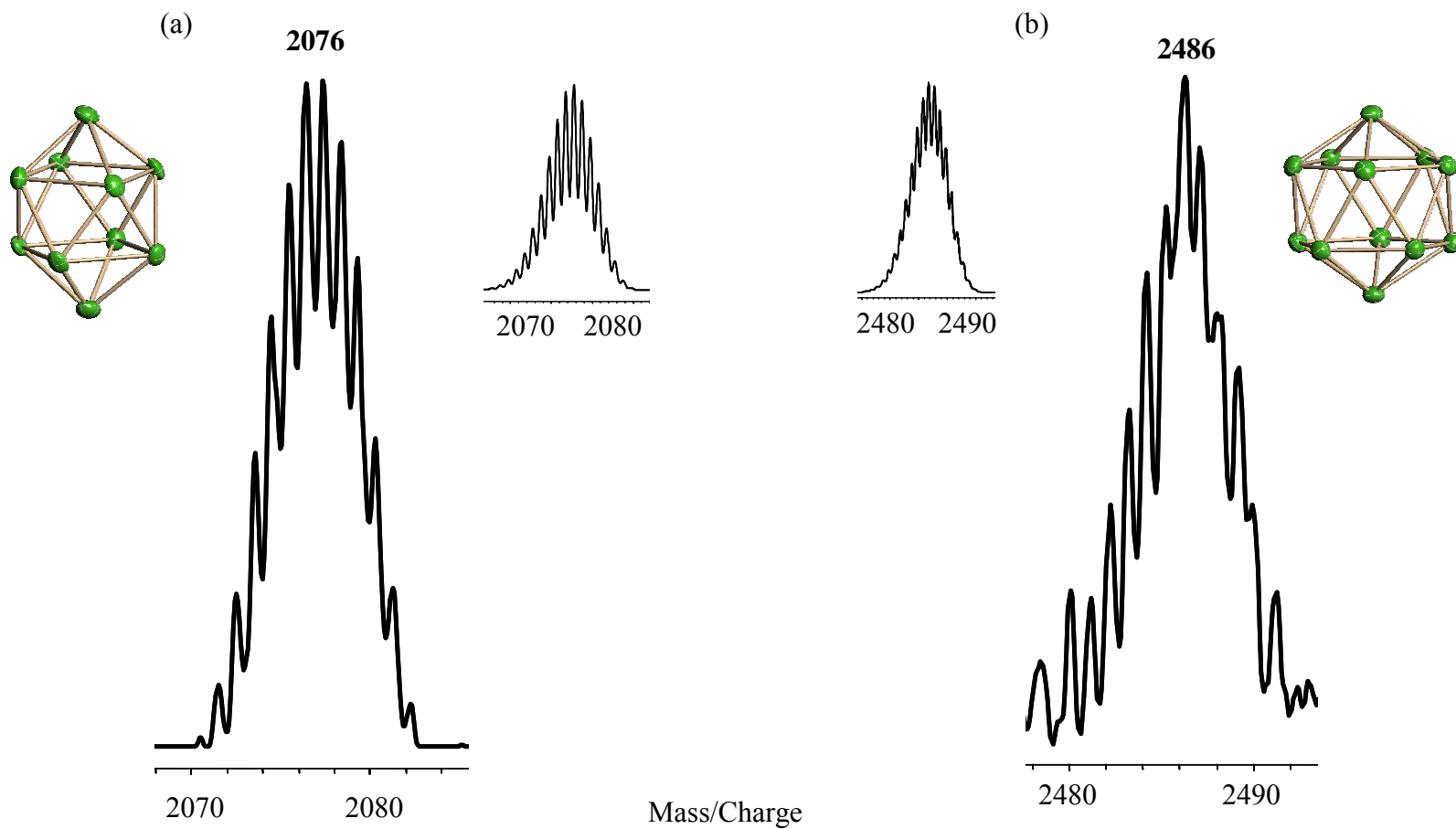


**Figure 2.8.** The LDI-TOF mass spectrum of the (a)  $[\text{Pb}_{12}]^{-1}$ , (b)  $[\text{Pb}_{10}]^{-1}$  ions. The insets show the calculated mass envelope of the corresponding ions and their proposed structures.

### 2.2.5. Extended Hückel Molecular Orbital Calculations

The qualitative Molecular Orbital (MO) diagram for the highly symmetric  $[\text{Pt}@\text{Pb}_{12}]^{2-}$  cluster ion was constructed with the aid of the Extended Hückel (EH) method in conjunction with an extensive group theory analysis. (Figure 2.9) The ordering of electronic states of the molecular orbitals may not be precise because of the low level of accuracy associated with the Extended Hückel method. The cluster has virtual  $I_h$  point symmetry, thus, the average bond distances were used to construct a cluster with perfect  $I_h$  on which to run the calculations.

An important ramification of the  $I_h$  point symmetry of the present compound is that the centered Pt atom experiences a cubic ligand field which makes the 5 d-orbitals degenerate. The qualitative molecular orbital diagram shows the interaction of the valence  $\text{Pb}_{12}^{2-}$  orbitals with the Pt-based s, p and d orbitals, which transform under the  $a_{1g}$ ,  $t_{1u}$  and  $h_g$  irreducible representations, respectively. The primary interactions between the Pt atom and  $\text{Pb}_{12}$  cage involve the Pt s ( $a_{1g}$ ) and p ( $t_{1u}$ ) atomic orbitals, therefore, the lines that correspond to the interactions involving the d-orbitals have been omitted from Figure 2.9 for clarity. The general electronic structure is quite similar to that of related centered icosahedra, such as  $[\text{CdTl}_{12}]^{12-}$  and sigma aromatic  $[\text{AlPb}_{12}]^+$ .<sup>39, 112</sup> The HOMO and LUMO frontier orbitals are primarily lead-based states and are presumably associated with the lowest energy electronic “intraligand” charge transfer transition that is responsible for the intense color of the compound.



### 2.3. Discussion

The presented family of metal clusters,  $[M@Pb_{12}]^{2-}$  ( $M = Pt, Pd, Ni$ ), are rare examples of endohedral naked metal clusters with near perfect icosahedral structures. The growth of  $Pb_{12}$  clusters from the parent anion,  $Pb_9$ , requires extensive fragmentation due to disproportionation between starting compound and product ( $Pb_9 \rightarrow Pb_{12}$ ). Despite that, icosahedral clusters form in moderate to high yields. In contrast to related Pt-Zintl ion chemistry,<sup>95</sup> oxidation of the  $Pb_9^{4-}$  Zintl ion to form the  $[M@Pb_{12}]^{2-}$  ( $M = Pt, Pd$ ) complexes does not result in  $H_2$  gas evolution. Instead, net oxidation of starting materials is accompanied by a reductive decomposition of the  $PPh_3$  ligand to give phenyl and  $Ph_2P^{1-}$  byproducts. On the other hand, in the formation of  $[Ni@Pb_{12}]^{2-}$  complex two-electron reduction of en solvent molecules result in the generation of  $H_2$ , which is effectively trapped through the hydrogenation of COD ligand to form cyclooctane.

Icosahedra of the 12 Pb atoms are stabilized by incorporation of the metal to the center of the cluster. Going up in the group, the atomic radius of the central metal atom decrease as do the diagonal distances. Thus, the  $Pb_{12}$  cluster gets more distorted. Since Pt atoms fit perfectly to the center of the icosahedra of lead atoms, almost no distortion in the cluster is observed. On the other hand, relatively small atomic radii of Pd and Ni atoms lead to a decrease in diagonal distances and distortion of the  $Pb_{12}$  cluster. Relative distortions of the cluster can be judged by comparing the ranges in Pb-Pb and Pb-M distances. (Table 2.4) The ranges increase as the central atom gets smaller and become maximized for the Ni centered cluster. The large deviations in

bond distances of  $[\text{Ni}@\text{Pb}_{12}]^{2-}$  anion might be an indication of instability of the cluster compared to  $[\text{M}@\text{Pb}_{12}]^{2-}$  ( $\text{M} = \text{Pt}, \text{Pd}$ ) anions. Therefore,  $[\text{K}(2,2,2)\text{-crypt}]_2$   $[\text{Ni}@\text{Pb}_{12}]$  form as a minor product in crystalline mixture and co-crystallize with  $[\text{K}(2,2,2)\text{-crypt}]_2$   $[\text{Ni}@\text{Pb}_{10}]$ .

One of the most substantial characteristics of these anions is that their general electronic structures are quite similar to that of aromatic clusters such as  $[\text{Al}@\text{Pb}_{12}]^+$ . For example, the comparison of the extended Hückel calculations revealed that  $[\text{Pt}@\text{Pb}_{12}]^{2-}$  has almost an identical molecular orbital diagram to that of the  $\sigma$ -aromatic  $[\text{Al}@\text{Pb}_{12}]^+$  with the exception of an extra  $h_g$  molecular orbital from Pt metal d orbitals of the  $[\text{Pt}@\text{Pb}_{12}]^{2-}$  anion. (Figure 2.10) Thus, while  $[\text{Pt}@\text{Pb}_{12}]^{2-}$  having total of 60 electrons, the number of total electrons is 50 for the  $\sigma$ -aromatic  $[\text{Al}@\text{Pb}_{12}]^+$  and extra 10 electrons of  $[\text{Pt}@\text{Pb}_{12}]^{2-}$  anion occupies the  $h_g$  orbitals.

The aromatic nature of the centered and noncentered cage clusters has been studied extensively with nuclear independent chemical shift (NICS) calculations. The study by Hirsch et al reported that the  $[\text{Pb}_9]^{4-}$  anion has aromatic nature with negative NICS value showing a diatropic chemical shift.<sup>132</sup> Schleyer, King, Lievens and co-workers predicted the antiaromatic property of the yet unknown icosahedral  $[\text{Si}_{12}]^{2-}$  cluster with its paratropic chemical shift. In addition, the  $[\text{Al}@\text{Pb}_{12}]^+$  ion, which has been identified by mass spectroscopy, showed aromatic nature with the diatropic chemical shift.<sup>39</sup> However, there is no reported experimental proof of the  $\sigma$ -aromaticity of the compound. To our knowledge, the first experimental measure of  $\sigma$ -aromaticity of centered icosahedral systems,  $[\text{M}@\text{Pb}_{12}]^{2-}$ , have been performed, and the result conflicts with that of the calculation.<sup>133</sup>

The aromatic nature of the  $[\text{Pt}@\text{Pb}_{12}]^{2-}$  anion has been investigated by Schleyer et.al by NICS method.<sup>133</sup> The calculations showed that the anion has aromatic character because of the negative NICS value (-20 ppm) similar to  $[\text{Al}@\text{Pb}_{12}]^+$ . Although the isolated  $[\text{M}@\text{Pb}_{12}]^{2-}$  (M = Pt, Pd, Ni) anions have similar electronic properties to  $[\text{Al}@\text{Pb}_{12}]^+$  ion, the results of the  $^{207}\text{Pb}$  NMR studies conflict

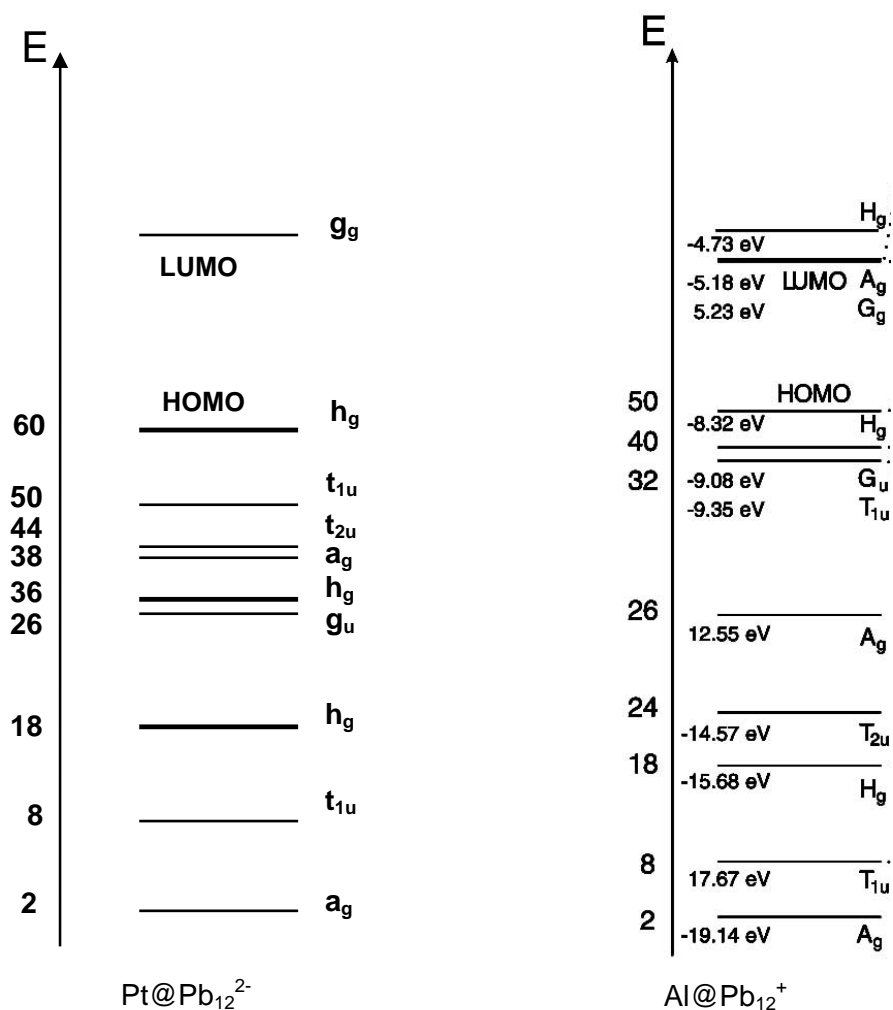


**Figure 2.10.** Qualitative MO diagram for the  $[\text{Pt}@\text{Pb}_{12}]^{2-}$  and  $[\text{Al}@\text{Pb}_{12}]^+$  ions (figure is taken from reference<sup>39</sup>).

with their findings. All three  $[M@Pb_{12}]^{2-}$  anions revealed paratropic (positive) chemical shifts, which are +1780, +1520, and +1167 ppm, respectively. Their chemical shifts are downfield and their extraordinary values become more pronounced when they are compared to other Pb clusters such as  $[Ni@Pb_{10}]^{2-}$ ,  $[Pb_9]^{4-}$ , and  $[Pb_9Mo(CO)_3]^{2-}$ .<sup>125, 129, 130</sup> (Table 2.6)

**Table 2.6.** The  $\sigma$ -Aromaticity in centered lead clusters.

Compound	$\delta$ (ppm) ( <sup>207</sup> Pb NMR)	NICS (ppm)	Aromaticity
$[Al@Pb_{10}]^+$ <sup>39</sup>	-	- 20	Aromatic
$[Al@Pb_{12}]^+$ <sup>39</sup>	-	- 26	Aromatic
$[Pt@Pb_{12}]^{2-}$ <sup>134</sup>	+ 1780	- 20 <sup>133</sup>	Antiaromatic ?
$[Pd@Pb_{12}]^{2-}$	+ 1520	-	Antiaromatic ?
$[Ni@Pb_{12}]^{2-}$	+ 1167	-	Antiaromatic ?
$[Ni@Pb_{10}]^{2-}$ <sup>130</sup>	- 996	-	Aromatic ?
$[Pb_9]^{4-}$ <sup>129</sup>	- 4098	-	-
$[Pb_9Mo(CO)_3]^{4-}$ <sup>125</sup>	-1934, -3450, +27	-	-

The clusters with enhanced stabilities are referred to as ‘magic number’ clusters.<sup>25</sup> One of the criteria to explain special stability of these clusters is the gap between highest occupied molecular orbital (HOMO) and lowest unoccupied molecular orbital (LUMO).<sup>135</sup> The well-known magic number cluster,  $Al_{13}^-$  ( $Al@Al_{12}^-$ ), is considered highly stable based on its large HOMO-LUMO gap (1.87

eV).<sup>122</sup> Another example is the recently reported Pb based centered icosahedra,  $[\text{Al}@\text{Pb}_{12}]^+$ . It is also reported as magic number cluster because of its high stability, determined by its highly symmetric structure and large HOMO-LUMO gap (calculated 3.1 eV).<sup>39</sup> Despite the high stabilities of  $\text{Al}_{13}^-$  and  $[\text{Al}@\text{Pb}_{12}]^+$  in gas phase, neither could be prepared in condensed phase.  $[\text{M}@\text{Pb}_{12}]^{2-}$  (M = Pt, Pd, Ni) anions are the first isolated ligand free icosahedral clusters. Due to their high HOMO-LUMO gaps (calculated 2.71 eV for  $[\text{Pt}@\text{Pb}_{12}]^{2-}$ ) and highly symmetric closed-packed geometry, the anions appear to be ‘magic’ as well.

The  $[\text{M}@\text{Pb}_{12}]^{2-}$  (M = Pt, Pd, Ni) anions show remarkable similarities with endohedral fullerenes due to their highly symmetric, homoatomic frameworks and bonding natures. The presence of five-fold degenerate d-states in a Pt complex is unusual and is also reminiscent of the electronic structures of gas phase atoms and endohedral complexes. The endohedral fullerenes (*e.g.*  $\text{La}@\text{C}_{60}$ ) have received significant attention due to their unusual physical, electronic and spectroscopic properties.<sup>136-139</sup> The centered Zintl clusters should prove to be equally interesting.<sup>140</sup>

## 2.4. Experimental Section

### 2.4.1. General Data

All reactions were performed in a nitrogen atmosphere drybox (Vacuum Atmosphere Co.). The  $^{207}\text{Pb}$  NMR and  $^{195}\text{Pt}$  NMR spectrum were recorded on a Bruker DRX500 Avance spectrometer operating at 104.5 and 107.5 MHz. The LDI-TOF\_MS studies were performed on a Kompact Maldi Axima-CFR instrument with a purged glove bag over sample chamber. The system uses a nitrogen laser light at 337

nm with a 3ns pulsewidth. Longitudinal relaxation time ( $T_1$ ) for Pb nuclei was measured by inversion recovery experiment at 285 K on a Bruker DRX500 Avance spectrometer operating at 107.5 MHz. The pulse sequence for inversion recovery experiment is  $180^\circ$ - $\tau$ - $90^\circ$ -acquisition. Data interpreted by the software program plotting  $M_z$  (magnetization vector on z axis) vs  $t$  (delay for inversion recovery), where  $M_z = (1-2\exp(-t/T_1))M_0$ , ( $M_0$  = magnetization at thermal equilibrium).<sup>[51]</sup>  $M_z$  gets zero signal intensity at time  $\tau_0 = T_1 \ln 2 \approx 0.7T_1$ . The  $T_1$  measurements were repeated three times for twelve different  $t$  ( $t = 0.0001s, 0.002s, 0.005s, 0.0008, 0.0009s, 0.001s, 0.0015s, 0.002s, 0.003s, 0.005s, 0.01s, 0.1s$ ) with  $d_1$  (relaxation delay) 2s. The result was obtained as 1.5 ms with the  $1.433 \times 10^{-2}$  uncertainties. AMRAY 1820K scanning electron microscope with a potential of 20 kV was used for energy dispersive X-ray (EDX) studies. Extended Hückel calculations were performed using a CACHE<sup>®</sup> software package.

#### 2.4.2. Chemicals

Melts of nominal composition  $K_4Pb_9$  was made by fusion (at high temperature) of stoichiometric ratios of the elements. The chemicals were sealed in evacuated, silica tubes and heated carefully with a natural gas/oxygen flame. 4,7,13,16,21,24-Hexaoxa-1,10-diazobicyclo[8,8,8]-hexacosane (2,2,2-crypt) were purchased from Aldrich.  $Ni(COD)_2$ ,  $Pd(PPh_3)_4$  and  $Pt(PPh_3)_4$  were purchased from Strem. Anhydrous ethylenediamine (en) and dimethylformamide (DMF) were purchased from Fisher, vacuum distilled from  $K_4Sn_9$ , and stored under dinitrogen. Toluene was distilled from sodium/benzophenone under dinitrogen and stored under dinitrogen.

### 2.4.3. Synthesis

#### 2.4.3.1. Preparation of [K(2,2,2-crypt)]<sub>2</sub>[Pt@Pb<sub>12</sub>]:

In vial 1, K<sub>4</sub>Pb<sub>9</sub> (80mg, 0.039 mmol) and 2,2,2-crypt (59.6 mg, 0.156 mmol) were dissolved in en (~ 2ml) and stirred for ~5 min., yielding a dark green solution. In vial 2, Pt(PPh<sub>3</sub>)<sub>4</sub> (49 mg., 0.039 mmol) was dissolved in tol (~ 1ml.) yielding a pale yellow solution. The solution from vial 2 was added drop wise to vial 1 and mixture was stirred ~2 h. yielding a reddish brown solution. The solution was then filtered through tightly packed glass wool. After a day, big black crystals of [K(2,2,2-crypt)]<sub>2</sub>[Pt@Pb<sub>12</sub>] precipitated. Yield: ~ 48mg (~60 %). EDX analysis on crystals showed presence of Pb, K, Pt atoms. <sup>207</sup>Pb NMR (dmf) δ(ppm): 1780, <sup>1</sup>J<sub>Pt-Pb</sub> ≈ 3432 Hz. <sup>195</sup>Pt NMR (dmf) δ(ppm): -4427, <sup>1</sup>J<sub>Pt-Pb</sub> ≈ 3445 Hz. T<sub>1</sub> = 1.5 msec. LDI-TOF MS, m/z = 2271 [Pt@Pb<sub>10</sub>]<sup>1-</sup>; 2310 [Pt@Pb<sub>10</sub>K]<sup>1-</sup>; 2683 [Pt@Pb<sub>12</sub>]<sup>1-</sup>; 2720 [Pt@Pb<sub>12</sub>K]<sup>1-</sup>; 2076 [Pb<sub>10</sub>]<sup>1-</sup>; 2488 [Pb<sub>12</sub>]<sup>1-</sup>; 2528 [Pb<sub>12</sub>K]<sup>1-</sup>.

#### 2.4.3.2. Preparation of [K(2,2,2-crypt)]<sub>2</sub>[Pd@Pb<sub>12</sub>].tol :

In vial 1, K<sub>4</sub>Pb<sub>9</sub> (80mg, 0.039 mmol) and 2,2,2-crypt (59.6 mg, 0.156 mmol) were dissolved in en (~ 2ml) and stirred for ~5 min., yielding a dark green solution. In vial 2, Pd(PPh<sub>3</sub>)<sub>4</sub> ( 29 mg., 0.020 mmol) was dissolved in tol (~ 1ml.) yielding a pale yellow solution. The solution from vial 2 was added drop wise to vial 1 and mixture was stirred ~2 h. yielding a reddish brown solution. The solution was then filtered through tightly packed glass wool. After two days, dark red crystals of [K(2,2,2-crypt)]<sub>2</sub>[Pd@Pb<sub>12</sub>] precipitated. Yield: ~20mg (~30 %). <sup>207</sup>Pb NMR (DMF, 15 °C) δ(ppm): 1520 (Δ<sub>1/2</sub>: 285 Hz). LDI-TOF MS, m/z = 2182 [Pd@Pb<sub>10</sub>]<sup>1-</sup>; 2220

[Pd@Pb<sub>10</sub>K]<sup>1-</sup>; 2592 [Pd@Pb<sub>12</sub>]<sup>1-</sup>; 2526 [Pd@Pb<sub>12</sub>K]<sup>1-</sup>; 2076 [Pb<sub>10</sub>]<sup>1-</sup>; 2486 [Pb<sub>12</sub>]<sup>1-</sup>; 2527 [Pb<sub>12</sub>K]<sup>1-</sup>.

#### 2.4.3.3. Preparation of [K(2,2,2-crypt)]<sub>2</sub>[Ni@Pb<sub>12</sub>]<sup>• en</sup>:

In a vial 1, K<sub>4</sub>Pb<sub>9</sub> (50 mg, 0.024 mmol), 2,2,2-crypt (37.2 mg, 0.096 mmol), and were dissolved in en (ethylenediamine) (~2 mL) yielding a brown mixture. In vial 2, Ni(COD)<sub>2</sub> (10.9 mg, 0.024 mmol) was dissolved in toluene (~1 mL) producing a yellow solution. The contents of vial 2 were added to the contents of 1 and the reaction mixture was stirred for 2 h yielding dark red-brown solution. The reaction mixture was filtered through tightly packed glass wool in a pipet. Dark red crystals formed in the reaction vessel after 4-5 days (~25mg, ~90:10 mixture of [Ni@Pb<sub>10</sub>]<sup>2-</sup>: [Ni@Pb<sub>12</sub>]<sup>2-</sup> crystals). <sup>207</sup>Pb NMR (DMF, 25 °C): δ (ppm): -996 (Δ<sub>1/2</sub>: 280 Hz) for [Pb<sub>10</sub>Ni]<sup>2-</sup> and 1167 (Δ<sub>1/2</sub>: 240Hz) for [Ni@Pb<sub>12</sub>]<sup>2-</sup>. LDI-TOF MS, m/z = 2135 [Ni@Pb<sub>10</sub>]<sup>1-</sup>; 2174 [Ni@Pb<sub>10</sub>K]<sup>1-</sup>; 2544 [Ni@Pb<sub>12</sub>]<sup>1-</sup>; 2584 [Ni@Pb<sub>12</sub>K]<sup>1-</sup>; 2076 [Pb<sub>10</sub>]<sup>1-</sup>; 2486 [Pb<sub>12</sub>]<sup>1-</sup>; 2527 [Pb<sub>12</sub>K]<sup>1-</sup>.

#### 2.4.3.4. Attempted Exchange of Central Metal Atom of Icosahedra:

In a dry box, ~ 20 mg of [K(2,2,2-crypt)]<sub>2</sub>[M@Pb<sub>12</sub>] (M = Pt (**1**), Pd (**2**), Ni (**3**)) crystals were dissolved in ~ 1 mL dmf. <sup>207</sup>Pb NMR data were recorded to confirm the presence of Pb<sub>12</sub> resonance before the exchange of central metal atom experiment. For the conversion of **1** to **3**, 4 mg of Ni(COD)<sub>2</sub>; for the conversion of **2** to **3**, 5.5 mg of Ni(COD)<sub>2</sub>; and finally for the conversion of **1** to **2** 5.6 mg of Pt(PPh<sub>3</sub>)<sub>4</sub> was dissolved in ~ 0.5 mL toluene and added to the starting solution. The reaction solution

was stirred for 2 hr at room temperature. The resulting  $^{207}\text{Pb}$  NMR spectra showed neither the signal of starting compound nor the formation of target compound.

#### **2.4.3.5. Crystallographic Studies**

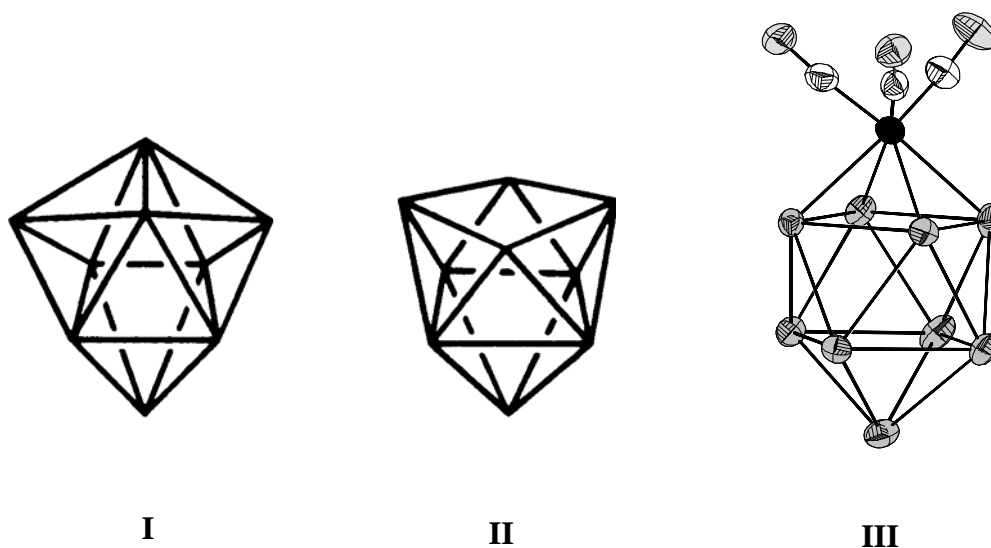
The crystal structures of the complexes were determined at single crystal X-ray facility at Chemistry and Biochemistry Department, University of Maryland, by Dr. James Fettingner.

## Chapter 3

### The closo-Pb<sub>10</sub><sup>2-</sup> Zintl ion in the [Ni@Pb<sub>10</sub>]<sup>2-</sup> cluster

#### 3.1. Introduction

The chemistry of the group 14 polyatomic anions (Zintl ions) is dominated by nine-atom clusters with boron-hydride-like structures. Examples include the naked [E<sub>9</sub>]<sup>x-</sup> ions where E = Si-Pb, x = 3,4 (see Scheme 3.1 I, II),<sup>78</sup> the [(Ge<sub>9</sub>)<sub>2</sub>]<sup>6-</sup> dimer, [(Ge<sub>9</sub>)<sub>3</sub>]<sup>6-</sup> trimer and <sub>1∞</sub>[(Ge<sub>9</sub>)<sup>2-</sup>] polymer formed by oxidative coupling of *nido*-[Ge<sub>9</sub>]<sup>4-</sup> clusters.<sup>87, 88, 90</sup> These anions have been studied extensively due to their simplicity,



Scheme 3.1.

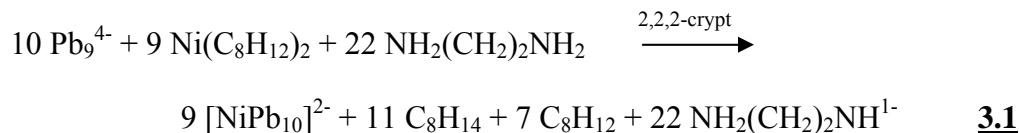
high reactivity and their potential utility in the preparation of nanomaterials.<sup>78</sup> The *closo*-[Sn<sub>9</sub>M(CO)<sub>3</sub>]<sup>4+</sup> complexes where M = Cr, Mo, W (see Scheme 3.1 III) are transition metal derivatives of the *nido*-Sn<sub>9</sub><sup>4+</sup> ion with virtually unperturbed Sn<sub>9</sub><sup>4+</sup> subunits capped by M(CO)<sub>3</sub> fragments. However, most transition metal derivatives of the E<sub>9</sub><sup>4+</sup> ions contain main group fragments with different structures and/or nuclearities. Structurally modified 9-atom clusters include the tricapped trigonal prismatic Sn<sub>9</sub> cluster in [Sn<sub>9</sub>Pt<sub>2</sub>(PPh<sub>3</sub>)<sub>2</sub>]<sup>2-</sup> complex<sup>94</sup> and the open Sn<sub>9</sub> framework in the *closo*-[Sn<sub>9</sub>W(CO)<sub>3</sub>]<sup>4+</sup> isomer. New Zintl ions are also stabilized by transition metal fragments as exemplified by the complexes *closo*-[Sn<sub>6</sub>{Cr(CO)<sub>5</sub>}<sub>6</sub>]<sup>2-</sup>, {Sn<sub>6</sub>[Nb(tol)]<sub>2</sub>}<sup>2-</sup> and [M@Pb<sub>12</sub>]<sup>2-</sup> (M = Pt, Pd, Ni) that contain the previously unknown Sn<sub>6</sub><sup>2-</sup>, Sn<sub>6</sub><sup>12-</sup> and Pb<sub>12</sub><sup>2-</sup> ions, respectively.<sup>96, 134, 141</sup> The latter complex represents a rare example of an endohedral naked metal cluster, and due to their high symmetry and potential σ-aromaticity, this class of clusters has received much attention of late.<sup>31, 142-146</sup> Extensive theoretical studies<sup>32, 147-150</sup> have been performed on hypothetical members of this class, but only a few gas phase studies<sup>36, 39, 151</sup> suggested their existence and structural data are sparse. Here, the synthesis, structure and properties of a new member of this class of endohedral clusters, [Ni@Pb<sub>10</sub>]<sup>2-</sup>, will be presented. The anion contains a Ni atom centered in a *closo*-[Pb<sub>10</sub>]<sup>2-</sup> bicapped square antiprism, and the cluster is a new type Zintl ion with virtual D<sub>4d</sub> point symmetry. Interesting gas phase products, Pt and Pd analogs of [Ni@Pb<sub>10</sub>]<sup>2-</sup> will also be presented.

## 3.2. Results and Discussion

### 3.2.1. Synthesis

Solutions of  $K_4Pb_9$  in ethylenediamine (en) react with solutions of  $Ni(COD)_2$  in toluene (tol) in the presence of 2,2,2-crypt to give moderate yields of the  $[Pb_{10}Ni]^{2-}$  ion as the  $[K(2,2,2-crypt)]^+$  salt. Small quantities ( $< \sim 10\%$ ) of  $[K(2,2,2-crypt)]_2[Ni@Pb_{12}]$  co-crystallize with the  $[K(2,2,2-crypt)]_2[Ni@Pb_{10}]$ . However, the formation of the  $[Ni@Pb_{10}]^{2-}$  is described as in the equation 1. Since both anions crystallize as thin red-brown plates, it is difficult to differentiate in solid state. Therefore, product ratios were estimated from  $^{207}Pb$  NMR analysis.

The formation of the anion requires a net two-electron oxidation of the starting materials that is accompanied by a two-electron reduction of solvent molecules. The en solvent molecules are reduced with the formal generation of  $H_2$  and  $NH_2(CH_2)_2NH^{1-}$  ions. The eliminated equivalents of  $H_2$  are effectively trapped through the hydrogenation of COD to form cyclooctene, which was identified in the reaction mixture by GC-MS analysis.



The crystalline solid forms stable reddish brown solutions in DMF (dimethylformamide) and DMSO (dimethylsulfoxide). The compound is highly air and moisture sensitive in solution and the solid state. The salt has been characterized

by single crystal XRD, energy-dispersive X-ray (EDX) analysis,  $^{207}\text{Pb}$  NMR and laser desorption / ionization-time of-flight mass spectrometry (LDI-TOF MS).

### 3.2.2. Solid State Structure

The  $[\text{Ni}@\text{Pb}_{10}]^{2-}$  anion crystallizes with two  $[\text{K}(2,2,2\text{-crypt})]^+$  cations in the monoclinic system, space group  $C2/c$ . Summaries of the crystallographic data and selected bond distances and angles for the complex is given in Table 3.1 and Table 3.2, respectively.

The anion possesses virtual  $D_{4d}$  point symmetry and is defined by a 10-vertex  $\text{Pb}_{10}^{2-}$  bicapped square antiprism centered by a Ni atom. (Figure 3.1) According to the conventions for Wade's rules for electron counting,<sup>[23]</sup> the Pb and Ni atoms donate two electrons and zero electrons to the cluster bonding, respectively. That result in a 22 electron,  $2n+2$  framework with a *closo* geometry when the -2 charge of the cluster

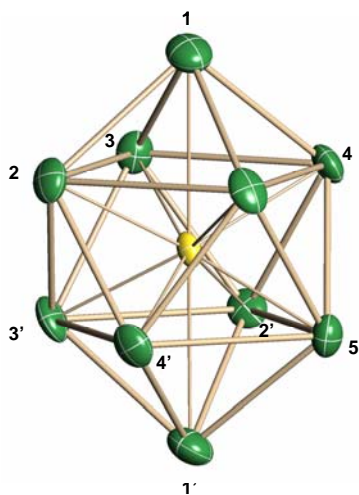


**Figure 3.1.** ORTEP drawing of the  $[\text{Ni}@\text{Pb}_{10}]^{2-}$  ion showing bicapped square antiprism structure. Ni is yellow, Pb is yellow. Thermal ellipsoids are set at the 50% probability level.

**Table 3.1.** Crystallographic data for the [Ni@Pb<sub>10</sub>]<sup>2-</sup> ion.

	[NiPb <sub>10</sub> ] [K(2,2,2-crypt)] <sub>2</sub>
Empirical formula	NiPb <sub>10</sub> C <sub>36</sub> H <sub>72</sub> K <sub>2</sub> N <sub>4</sub> O <sub>12</sub>
Formula weight	2961.79
Temperature (K)	173(2)
Wavelength (Å)	0.71073
Crystal system	monoclinic
Space group	C2/c
Unit cell dimensions	
a (Å)	25(2)
b (Å)	11.940(4)
c (Å)	21.400(2)
α (deg)	90
β (deg)	96.91
γ (deg)	90
Volume (Å <sup>3</sup> )	6304(507)
Z	4
D <sub>calc</sub> (Mg/m <sup>3</sup> )	3.120
Abs coeff (mm <sup>-1</sup> )	27.067
Crystal size (mm)	0.41×0.13×0.06
Reflections collected	5757
Independent reflections	5758 [R(int) = 0.0000]
Data/restraints/parameters	5758 / 0 / 295
Goodness of fit on F <sup>2</sup>	1.060
Final R indices [I > 2σ(I)] <sup>a</sup>	
R1	0.0582
wR2	0.1645
R indices (all data) <sup>a</sup>	
R1	0.0827
wR2	0.1764

a. The function minimized during the full-matrix least-squares refinement was  $\Sigma w(\text{Fo}2 - \text{Fc}2)$  where  $w = 1/[\sigma^2(\text{Fo}2) + (0.0380 * P)^2 + 5.4664 * P]$  and  $P = \max(\text{Fo}2, 0) + (2 * \text{Fc}2) / 3$ .

**Table 3.2.** Selected bond lengths [Å] and angles [°] for [NiPb<sub>10</sub>] [K(2,2,2-crypt)]<sub>2</sub>

Ni(1)-Pb(1)	3.209(17)	Pb(1)-Pb(2)	3.10(7)
Ni(1)-Pb(2)	2.72(18)	Pb(2)-Pb(3)	3.4(2)
Ni(1)-Pb(3)	2.720(10)	Pb(2)-Pb(3')	3.13(9)
Ni(1)-Pb(4)	2.72(9)	Pb(3)-Pb(4)	3.41(3)
Ni(1)-Pb(5)	2.73(4)	Pb(4)-Pb(2')	3.141(13)
<hr/>			
Pb(1)-Ni(1)-Pb(1')	179.59(8)	Pb(1)-Pb(3)-Pb(4)	55.89(2)
Pb(2)-Ni(1)-Pb(3)	78.65(5)	Pb(1)-Pb(3)-Pb(2')	109.00(2)
Pb(3')-Ni(1)-Pb(1)	117.78(6)	Ni(1)-Pb(2)-Pb(1)	66.56(2)
Pb(4)-Ni(1)-Pb(1)	61.67(2)	Pb(4)-Pb(1)-Pb(2)	102.15(2)
Pb(4)-Ni(1)-Pb(2)	124.14(2)	Pb(4)-Pb(1)-Ni(1)	51.21(2)
Pb(4)-Ni(1)-Pb(4')	138.92(9)	Pb(5)-Pb(4)-Pb(3)	90.80(2)

is taken into consideration. The two axial Pb-Ni bonds are elongated (3.210(3) Å (av)) in comparison with the other eight Pb-Ni bonds in the complex (2.722(2) Å). The 24 Pb-Pb contacts of the Pb<sub>10</sub> deltahedron can be categorized into three different types. The average distances to the capping Pb atom (Pb1) are the shortest at 3.094(2) Å. The Pb-Pb contacts between square planes are intermediate at 3.135(3) Å (av) whereas the distances between Pb atoms within the square planes are longest at 3.405(2) Å (av). A recent theoretical study by Schrodtr *et al.* of stable binary metal atom clusters suggested that the neutral bicapped tetragonal antiprism anion, Pb<sub>10</sub>Ni, with D<sub>4d</sub> point symmetry is the most stable isomer compared to other isomers.<sup>[24]</sup> Their DFT calculations predicted Pb-Pb bond distances of 3.12 – 3.21 Å and Pb-Ni distances of 2.89 – 2.99 Å that are reasonably close to the experimental results reported here. The discrepancies presumably result from the differences in

charge between the model and the isolated cluster, which finds the latter in a more axially-elongated structure.

### 3.2.3. NMR Spectroscopic Studies

Despite the two distinct chemical environments of lead in the title complex, its  $^{207}\text{Pb}$  NMR spectrum (Figure 3.2) shows a single, broad resonance at -996 ppm ( $\Delta\nu_{1/2} = 280$  Hz, at 25 °C) due to dynamic exchange. For comparison,  $[\text{Pb}_9]^{4-}$  shows a relatively sharp resonance ( $\Delta\nu_{1/2} = 47$  Hz, at 25 °C) under the same conditions (104.7 MHz) as a result of fast exchange on the NMR time scale. When the temperature is decreased gradually, the line width of the  $\text{Pb}_{10}$  signal increases to 2310 Hz at -45 °C, which is interpreted as slowing intramolecular exchange on the NMR time scale. However, we have yet to observe the limiting spectrum with the expected two

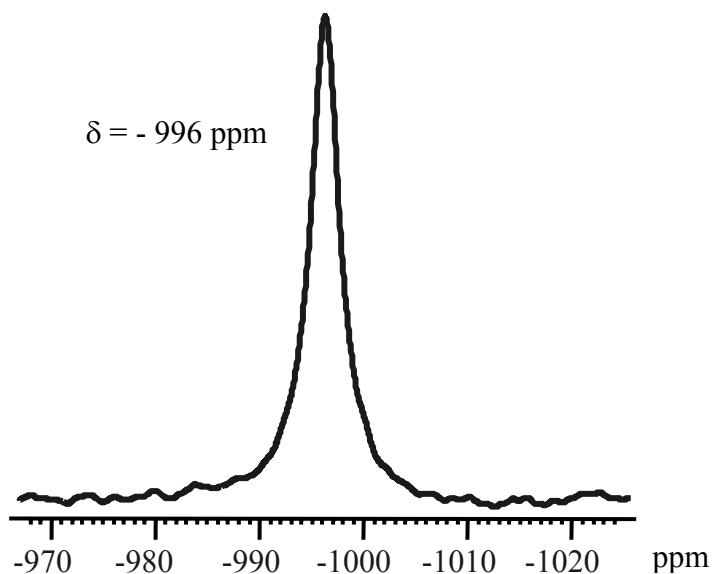


**Figure 3.2.** The  $^{207}\text{Pb}$  NMR spectrum of the  $[\text{Ni}@\text{Pb}_{10}]^{2-}$  ion recorded in dmf at 25 °C and 104.7 MHz. Table show change in line width ( $\nu\Delta_{1/2}$ ) with temperature.

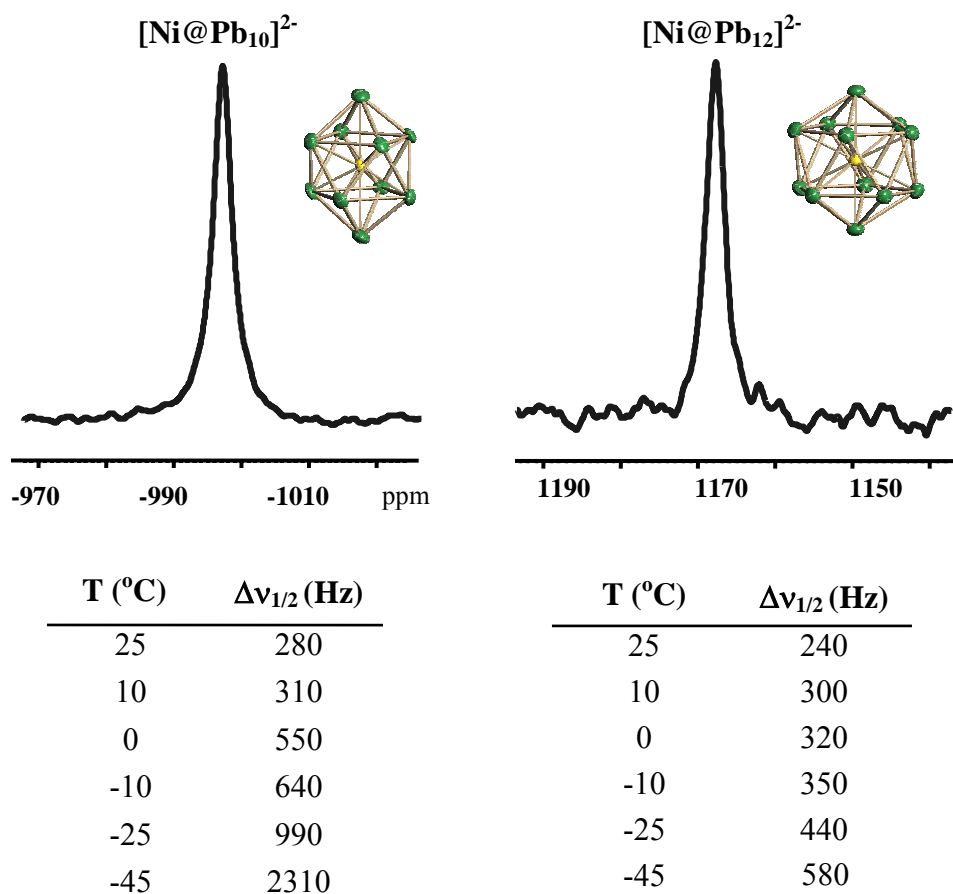


**Figure 3.3.** Temperature dependence of the  $^{207}\text{Pb}$  NMR line widths of  $[\text{Ni}@\text{Pb}_{10}]^{2-}$  and  $[\text{Ni}@\text{Pb}_{12}]^{2-}$ .

mutually coupled resonances. On the other hand, because of the high symmetry of  $[\text{Ni}@\text{Pb}_{12}]^{2-}$ , all lead atoms experience same chemical environment. Therefore,  $^{207}\text{Pb}$  NMR reveals single broad resonance as expected. A slight increase in the line width of  $\text{Pb}_{12}$  resonance upon decreasing temperature is interpreted as a result of tumbling of the molecule associated with chemical shift anisotropy. (Figure 3.3) The  $^{207}\text{Pb}$  NMR spectrum showed that the intensity of the  $[\text{Ni}@\text{Pb}_{10}]^{2-}$  signal is approximately an order of magnitude higher than the intensity of  $[\text{Ni}@\text{Pb}_{12}]^{2-}$ . The possible conversion between  $[\text{Ni}@\text{Pb}_{10}]^{2-}$  and  $[\text{Ni}@\text{Pb}_{12}]^{2-}$  anions has been investigated by

1D-selective EXSY experiment. The study revealed no conversion between anions in solution.

### 3.2.4. LDI-TOF Mass Spectrometry

The LDI-TOF mass spectrum (negative ion mode) of the  $[\text{Ni}@\text{Pb}_{10}]^{2-}$  complex shows distinctive mass envelopes associated with the  $[\text{Ni}@\text{Pb}_{10}\text{K}]^{1-}$  and  $[\text{Ni}@\text{Pb}_{10}]^{1-}$  ions (Figure 3.4). The observation of the oxidized parent ion and  $\text{K}^+$  ion pairs are common to Zintl clusters.<sup>131</sup> The isotopic envelopes seen in the spectrum is in excellent agreement with the simulated pattern for the coordinated and non-

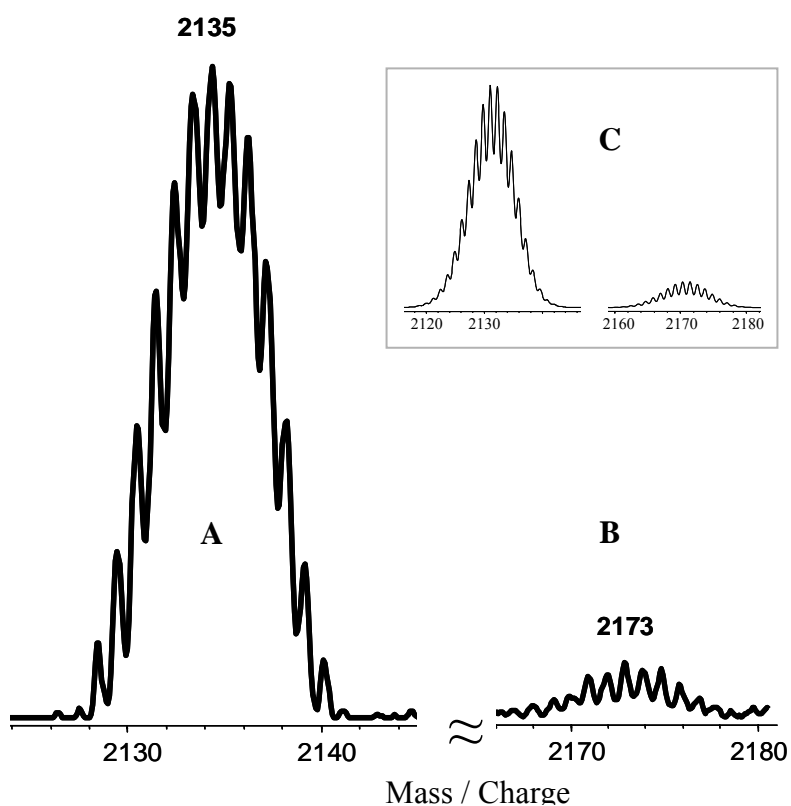


**Figure 3.4.** The LDI-TOF mass spectrum of a) the  $[\text{Pb}_{10}\text{Ni}]^{1-}$  and b)  $[\text{Pb}_{10}\text{Ni K}]^{1-}$  ions. c) The insets show the calculated mass envelope of the  $[\text{Pb}_{10}\text{Ni}]^{1-}$  and  $[\text{Pb}_{10}\text{Ni K}]^{1-}$  ions.

coordinated anions. Other peaks observed in the spectra, which are presented in the previous chapter, are  $[\text{Ni}@\text{Pb}_{12}]^{1-}$ ,  $[\text{Ni}@\text{Pb}_{12}\text{K}]^{1-}$  and the interesting, non-metallated gas phase products,  $[\text{Pb}_{10}]^{1-}$  and  $[\text{Pb}_{12}]^{1-}$ ,  $[\text{Pb}_{12}\text{K}]^{1-}$ .

Surprisingly, the LDI-TOF mass spectrum (negative ion mode) of the  $[\text{K}(2,2,2\text{-crypt})]_2[\text{M}@\text{Pb}_{12}]$  (M = Pt, Pd) crystals show Pt and Pd analogs of the  $[\text{Ni}@\text{Pb}_{10}]^{1-}$  anion. Between these three only Ni centered  $\text{Pb}_{10}$  cluster have been isolated in solid state. (Figure 3.5) The structural comparison of these gas phase products with isolated  $[\text{Ni}@\text{Pb}_{10}]^{2-}$  anion will be discussed in the next section.

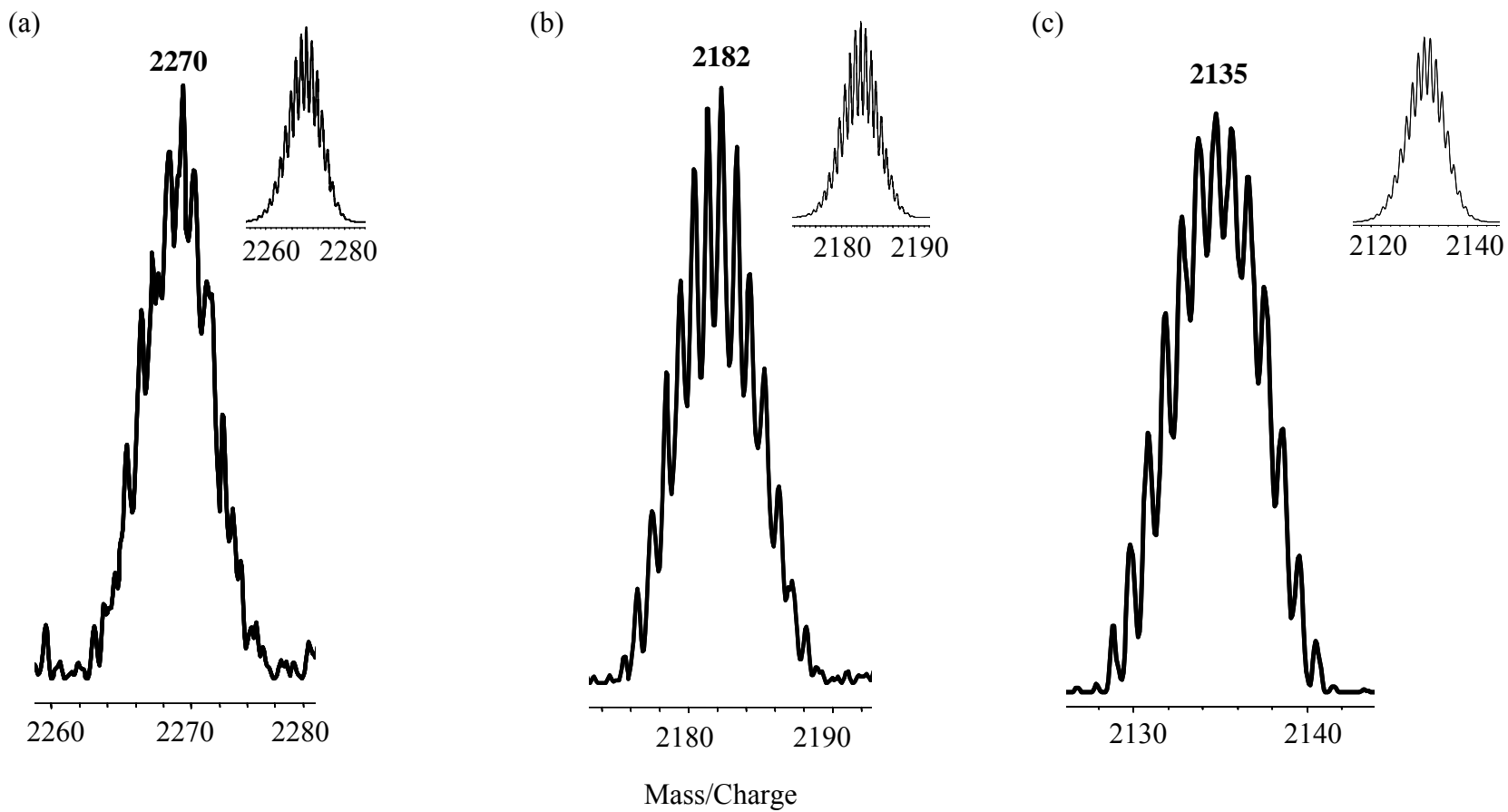


**Figure 3.5.** The LDI-TOF mass spectrum of the a)  $\text{Pt@Pb}_{10}]^{-1}$ , b)  $[\text{Pd@Pb}_{10}]^{-1}$ , and c)  $[\text{Ni@Pb}_{10}]^{-1}$  ions. The insets show the calculated mass envelope of the corresponding ions.

### 3.2.5. DFT Analysis on $[M@Pb_{10}]^{2-}$ (M = Ni, Pd, Pt) Clusters.

DFT calculations have been performed on  $[M@Pb_{10}]^{2-}$  (M = Ni, Pd, Pt) anions with  $D_{4d}$  point symmetry, and the bicapped square antiprism structure.<sup>152</sup> X-Ray crystal structural data for the  $[Ni@Pb_{10}]^{2-}$  anion was used as starting geometry for the all three anions. The starting geometries were then optimized. The calculated M-Pb and Pb-Pb bond distances are listed in Table 3.

The calculations showed that Ni atom fits very well to the center of the  $Pb_{10}$  cluster and Pt and Pd centered clusters appear to require distortion in the bond distances in order to accommodate the relatively bigger size Pt and Pd atoms. This conclusion is based on the following analysis. The geometry optimized structures of the  $[M@Pb_{10}]^{2-}$  (M = Pt, Pd, Ni) anions reveal larger size of Pt and Pd centered  $Pb_{10}$  clusters compared to the  $[Ni@Pb_{10}]^{2-}$  anion as expected. The Pb-M and Pb-Pb contacts increase as the size of the central metal atom gets larger. For all three anions, the two axial Pb-M contacts are elongated compared to the other eight Pb-M bonds in the complexes. However,  $Pb_{10}$  cluster become slightly more axially elongated as the size of the central atom decrease.

There are three different types of Pb-Pb distances for all three centered  $Pb_{10}$  clusters. The shortest Pb-Pb distances are the ones to the capping Pb atoms and the longest distances are the ones within the square planes. Due to the unavailability of the single crystal X-ray data for an empty  $Pb_{10}$  cluster, the Pb-Pb bond distances are compared with the distances in the  $Pb_9^{4-}$  anion, which has monocapped square antiprismatic structure.<sup>126</sup> Between the three clusters,  $[Ni@Pb_{10}]^{2-}$ , which has the

calculated bond distances that match almost perfectly with the ones obtained from X-ray data, has relatively closer Pb-Pb distances to the ones of  $\text{Pb}_9^{4-}$  anion. While the average Pb-Pb distances to the capping Pb atom is 3.067(3) Å for  $\text{Pb}_9^{4-}$  anion, it is 3.094(2) Å for the  $[\text{Ni}@\text{Pb}_{10}]^{2-}$  anion. The contacts within the capped square plane are 3.374(4) Å and 3.405(2) Å for the  $\text{Pb}_9^{4-}$  and  $[\text{Ni}@\text{Pb}_{10}]^{2-}$  anions, respectively. Finally, the distances between the square planes are 3.104(2) Å for the  $\text{Pb}_9^{4-}$  and it is 3.135(3) Å for the  $[\text{Ni}@\text{Pb}_{10}]^{2-}$  anion. For the Pt and Pd centered  $\text{Pb}_{10}$  clusters, these values are approximately one tenth of an angstrom larger compared to  $\text{Pb}_9^{4-}$  and  $[\text{Ni}@\text{Pb}_{10}]^{2-}$ , suggesting that there is a strain on Pb-Pb bond distances because of the size of the central atoms.

**Table 3.3.** Calculated bond lengths [Å] for  $[\text{M}@\text{Pb}_{10}]^{2-}$  (M = Ni, Pd, Pt).

M	Pt	Pd	Ni (calc.)	Ni (exp.)
<b>Pb-M distances to the capping (axial) Pb atoms</b>				
M-Pb(1)	3.256	3.276	3.266	3.210(1)
M-Pb(1')	3.257	3.276	3.266	3.210(1)
<b>Pb-M distances to the square planes (equatorial Pb atoms)</b>				
M-Pb(2)	2.826	2.804	2.741	2.720(1)
M-Pb(2')	2.826	2.804	2.741	2.720(1)
M-Pb(3)	2.824	2.801	2.736	2.720(2)
M-Pb(3')	2.824	2.801	2.736	2.720(2)
M-Pb(4)	2.829	2.807	2.745	2.720(1)
M-Pb(4')	2.828	2.807	2.744	2.720(1)
M-Pb(5)	2.830	2.810	2.750	2.732(2)
M-Pb(5')	2.830	2.810	2.750	2.732(2)
Avg.	2.827	2.806	2.743	2.722(2)
<i>Avg. (overall)</i>	<i>2.913</i>	<i>2.900</i>	<i>2.848</i>	<i>2.820(9)</i>

**Table 3.3.** Continued.

<b>M</b>	<b>Pt</b>	<b>Pd</b>	<b>Ni (calc.)</b>	<b>Ni (exp.)</b>
<b>Pb-Pb distances to the capping (axial) Pb atoms</b>				
Pb(1)-Pb(2)	3.155	3.153	3.122	3.103(1)
Pb(1)-Pb(3)	3.152	3.153	3.123	3.109(1)
Pb(1)-Pb(4)	3.160	3.153	3.118	3.067(1)
Pb(1)-Pb(5)	3.164	3.163	3.130	3.095(1)
Avg.	3.158	3.155	3.123	3.094(2)
<b>Pb-Pb distances between the square planes</b>				
Pb(2)-Pb(3')	3.266	3.247	3.175	3.128(1)
Pb(2)-Pb(4')	3.267	3.252	3.183	3.141(1)
Pb(3)-Pb(2')	3.267	3.247	3.174	3.128(1)
Pb(3)-Pb(3')	3.269	3.252	3.180	3.145(1)
Pb(4)-Pb(5')	3.264	3.245	3.175	3.126(1)
Pb(4)-Pb(2')	3.267	3.253	3.174	3.141(1)
Pb(5)-Pb(4')	3.265	3.245	3.175	3.126(1)
Pb(5)-Pb(5')	3.263	3.249	3.182	3.141(1)
Avg.	3.266	3.249	3.177	3.135(3)
<b>Pb-Pb distances within the square planes</b>				
Pb(3)-Pb(4)	3.537	3.506	3.425	3.411(1)
Pb(4)-Pb(5)	3.518	3.484	3.404	3.374(1)
Pb(2)-Pb(5)	3.526	3.490	3.410	3.390(1)
Pb(2)-Pb(3)	3.549	3.525	3.447	3.445(1)
Avg.	3.533	3.501	3.422	3.405(2)
<i>Avg.(overall)</i>	<i>3.310</i>	<i>3.290</i>	<i>3.225</i>	<i>3.192(4)</i>

### 3.3. Conclusion

A new member of endohedral cluster family has been isolated in this study. The  $[\text{Ni}@\text{Pb}_{10}]^{2-}$  anion has intriguing highly symmetric,  $D_{4d}$  *closo* structure. Similar 10-atom, transition metal centered Zintl ion clusters have been reported, such as  $[\text{Ni}@\text{Sn}_9\text{Ni}(\text{CO})]^{3-}$  possessing  $C_{4v}$  *closo* structure. However, the  $[\text{Ni}@\text{Pb}_{10}]^{2-}$  is the *first* ten-atom endohedral naked Zintl ion cluster with its homoatomic framework.

$[\text{Ni}@\text{Pb}_{10}]^{2-}$  is not the only complex formed in the reaction solution.  $[\text{K}(2,2,2\text{-crypt})]_2[\text{Ni}@\text{Pb}_{12}]$  co-crystallize with  $[\text{K}(2,2,2\text{-crypt})]_2[\text{Ni}@\text{Pb}_{10}]$ , which is a major product in the crystalline mixture ( $\sim 10 : 90$ ). It is difficult to determine exact quantities of the compounds in solid state since both anions form thin, plate-like red-brown crystals. Therefore, approximate product ratios were estimated from  $^{207}\text{Pb}$  NMR analysis in which the intensity of  $[\text{Ni}@\text{Pb}_{10}]^{2-}$  signal is approximately an order of magnitude higher than the intensity of  $[\text{Ni}@\text{Pb}_{12}]^{2-}$ .

The Pt and Pd analogs of  $[\text{Ni}@\text{Pb}_{10}]^{2-}$  have been observed in the gas phase by matrix-free MALDI-TOF-MS (see chapter 2). They have never been isolated in solid state, but they are expected to be isostructural to the anion **1**. The solution stability of them has been studied by means of  $^{207}\text{Pb}$  NMR spectroscopy. According to this investigation, either they do not exist in solution or they form in very small quantities that they can not be observed.

The bonding natures of both the isolated Ni analog and the gas phase anions (Pt and Pd analogs) have been investigated by means of DFT calculations. The calculated bond distances for the  $[\text{Ni}@\text{Pb}_{10}]^{2-}$  are in remarkable agreement with the

experimental (single crystal X-ray data) values. The results reveal that Ni atom fits very well in the  $\text{Pb}_{10}$  cluster and the cluster size increases as the radius of central atom increases, as expected. The axial elongation is observed for all three anions. It has been reported that the knowledge of the axial distances become more important for the design of magnetic materials.<sup>153</sup>

The existence and stability of the Ni analog in solution was verified by  $^{207}\text{Pb}$  NMR spectroscopy. Despite the asymmetric nature of  $[\text{Ni}@\text{Pb}_{10}]^{2-}$  cluster,  $^{207}\text{Pb}$  NMR spectrum shows a single broad resonance. Temperature dependence studies of NMR line-widths of  $[\text{Ni}@\text{Pb}_{10}]^{2-}$  and  $[\text{Ni}@\text{Pb}_{12}]^{2-}$  signals revealed significantly different behavior in solution. (Figure 3.3) At low temperatures, the  $[\text{Ni}@\text{Pb}_{10}]^{2-}$  anion showed intramolecular exchange of the equatorial and capping Pb atoms on the NMR time scale. Due to the high symmetry of the  $[\text{Ni}@\text{Pb}_{12}]^{2-}$  anion, the broadening of the  $\text{Pb}_{12}$  resonance is most likely because of tumbling of the molecule associating with chemical shift anisotropy.

The  $^{207}\text{Pb}$  NMR analysis gives important knowledge about dynamic behavior of the cluster anions described here. The study shows that despite the anisotropic structure, the  $[\text{Ni}@\text{Pb}_{10}]^{2-}$  cluster does not remain static and demonstrate global atomic exchange. The fluxional nature of the anion is analogous to other single focus clusters (having one centered atom) such as  $[\text{Sn}_9\text{Pt}_2(\text{PPh}_3)]^{2-}$ . This suggests the existence of the extensive atomic mobility of a variety of small metallic particles.

## 3.4. Experimental Section

### 3.4.1. General Data

All reactions were performed in a nitrogen atmosphere drybox (Vacuum Atmosphere Co.).  $^{207}\text{Pb}$  NMR was recorded on Bruker DRX500 Avance spectrometer operating at 104.7 MHz. An AMRAY 1820K scanning electron microscope with a potential of 20 kV was used for energy dispersive X-ray (EDX) studies. LDI-TOF-MS studies were performed on a Kompact Maldi Axima-CFR instrument with a purged glove bag over sample chamber. The system uses a nitrogen laser light at 337 nm and a 3ns pulse width.

*1D-Selective EXSY Experiments* have been performed at 283 K on Bruker DRX500 Avance spectrometer operating at 104.6 MHz to investigate possible exchange between  $[\text{Ni}@\text{Pb}_{10}]^{2-}$  and  $[\text{Ni}@\text{Pb}_{12}]^{2-}$  anions. The pulse sequence for the experiment is *selective 180° -  $\tau$  - 90° - acquisition*. The frequencies of  $[\text{Ni}@\text{Pb}_{10}]^{2-}$  and  $[\text{Ni}@\text{Pb}_{12}]^{2-}$  resonances were defined as -102471 and 122147 MHz, respectively. The former resonance is irradiated and the change in the latter is observed. The experiment was done for four different  $t$  ( $t = 0.05\text{s}, 0.25\text{s}, 0.45\text{s}, 0.65\text{s}$ ) with  $d_1$  (relaxation delay) 0.8s and no exchange was observed.

*DFT calculations:* The program package PRIRODA<sup>154, 155</sup> was used for all DFT calculations with specifically functional PBE. Relativistic Stevens-Bausch-Krauss (SBK) effective core potentials were used in PBE calculations. The basis set was 311-split for main group elements. The X-ray diffraction data of the  $[\text{Ni}@\text{Pb}_{10}]^{2-}$  anion is used as starting coordinates for all the three anions. Coordinates used for

bond order and charge calculations were first optimized by the PRIRODA program without constraints on symmetry. A multiplicity 1 was used for the anions for convergence to occur.

### 3.4.2. Chemicals

Melts of nominal composition  $K_4Pb_9$  was made by fusion (at high temperature) of stoichiometric ratios of the elements. The chemicals were sealed in evacuated, silica tubes and heated carefully with a natural gas/oxygen flame. 4,7,13,16,21,24-Hexaoxa-1,10-diazobicyclo[8,8,8]-hexacosane (2,2,2-crypt) were purchased from Aldrich.  $Ni(COD)_2$  was purchased from Strem. Anhydrous ethylenediamine (en) and dimethylformamide (DMF) were purchased from Fisher, vacuum distilled from  $K_4Sn_9$ , and stored under dinitrogen. Toluene was distilled from sodium/benzophenone under dinitrogen and stored under dinitrogen.

### 3.4.3. Synthesis

#### 3.4.3.1. Preparation of $[K(2,2,2-crypt)]_2[Ni@Pb_{10}]$

In a drybox,  $K_4Pb_9$  (80mg, 0.04 mmol) and 2,2,2-crypt (59.6 mg, 0.158 mmol) were dissolved in en (~ 2mL) in vial 1 yielding a dark green solution. In vial 2,  $Ni(COD)_2$  (10.9 mg, 0.024 mmol) was dissolved in toluene (~1 mL) yielding a yellow solution. The solution from vial 2 was added drop wise to vial 1 and mixture was stirred ~2 h yielding a reddish brown solution. The solution was then filtered through tightly packed glass wool. Dark red crystals formed in the reaction vessel after 4-5 days (in moderate yield). EDX analysis on crystals showed presence of Pb, K, Ni atoms.  $^{207}Pb$  NMR (dmf, 25 °C):  $\delta$  (ppm): -996 (vs.  $Pb(NO_3)_2$ ,  $\delta = -2961.2$  ppm ),

$\Delta\nu_{1/2} = 280$  Hz . LDI-TOF MS,  $m/z = 2174$   $\text{K}[\text{Pb}_{10}\text{Ni}]^{1-}$ ,  $2135$   $[\text{Pb}_{10}\text{Ni}]^{1-}$ . LDI-TOF MS,  $m/z = 2135$   $[\text{Ni}@\text{Pb}_{10}]^{1-}$ ;  $2174$   $[\text{Ni}@\text{Pb}_{10}\text{K}]^{1-}$ ;  $2544$   $[\text{Ni}@\text{Pb}_{12}]^{1-}$ ;  $2584$   $[\text{Ni}@\text{Pb}_{12}\text{K}]^{1-}$ ;  $2076$   $[\text{Pb}_{10}]^{1-}$ ;  $2486$   $[\text{Pb}_{12}]^{1-}$ ;  $2527$   $[\text{Pb}_{12}\text{K}]^{1-}$ .

#### **3.4.3.2. Crystallographic Studies**

The crystal structures of the complexes were determined at single crystal X-ray facility at Chemistry and Biochemistry Department, University of Maryland, by Dr. James Fettingner.

## Chapter 4

### Synthesis, Structure and Dynamic Properties of $[\text{Ni}_2\text{Sn}_{17}]^{4-}$

#### 4.1. Introduction

Bimetallic nanoparticles with variety of architectures, i.e. alloys and core-shell particles, have received a great deal of attention due to their unusual catalytic, optical and magnetic properties. New synthetic methods are continuing to be developed to prepare uniform, monodispersed bimetallic particles in the nanoscale. The quest to prepare increasingly large molecular bimetallic clusters is a promising avenue in the study of bimetallic nanoparticles.<sup>156-159</sup> Such clusters reported to date are often coated by ligand shells that prevent aggregation into larger particles and provide fixed nuclearity and monodispersity. However, the ligand spheres can alter or eliminate the reactivity and properties of the nanoparticle core.

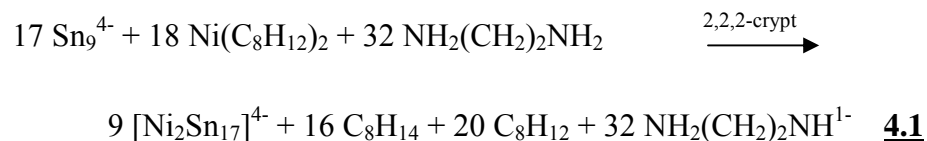
Transition metal derivatives of the polyatomic main group anions (Zintl ions) are the potential bridge between the chemistry of large clusters and nanoparticles.<sup>78,</sup>  
<sup>140</sup> As described in Chapter 2, the highly symmetric ligand-free  $[\text{M}@\text{Pb}_{12}]^{2-}$  icosahedral anions (M = Pt, Pd, Ni) are the smallest possible subunits in a nanoparticle close-packed crystal lattice and are models for core-shell structures without ligand spheres.<sup>134</sup> Besides having interesting electronic and spectroscopic

properties, the molecular nature of these clusters allow for the study of solution dynamics by way of dynamic multinuclear NMR spectroscopy. The asymmetric  $[\text{Ni}@\text{Pb}_{10}]^{2-}$  cluster demonstrated that intramolecular exchange of the equatorial and capping Pb atoms is fast on the NMR time scale at very low temperatures.<sup>130</sup> Similar fluxionality has also been observed for other one focus clusters (i.e. those having one centered atom),<sup>95</sup> indicating possible atomic mobility of small metallic particles. The recently reported two focus clusters,  $[\text{Pd}_2@\text{Ge}_{18}]^{4-}$  and  $[\text{Ni}_3@\text{Ge}_{18}]^{4-}$ ,<sup>99, 100</sup> raise the question of whether atomic exchange can occur in larger, more separated regions of clusters and nanoparticles. In this study, we describe the synthesis, characterization, and surprising dynamic exchange in  $[\text{Ni}_2\text{Sn}_{17}]^{4-}$ ; a two-focus cluster with  $\text{NiSn}_8$  subunits linked by a single Sn atom.

#### 4.1.1. Results

#### 4.1.2. Synthesis

Ethylenediamine(en) solution of  $\text{K}_4\text{Sn}_9$  reacts with toluene solution of  $\text{Ni}(\text{COD})_2$  in the presence of 2,2,2-crypt to give  $[\text{Ni}_2\text{Sn}_{17}]^{4-}$ , **1**, in ca. 20 % crystalline yield as the  $[\text{K}(2,2,2\text{-crypt})]^+$  salt. The anion results from oxidation of starting materials, which is facilitated by reduction of en solvent molecules and subsequent  $\text{H}_2$  elimination. The generated  $\text{H}_2$  was trapped through the hydrogenation of COD ligands and results in the formation of cyclooctene, which was verified by GC-MS analysis of the reaction mixture. The reaction is similar to the  $\text{H}_2$  formation in the synthesis<sup>95</sup> of  $[\text{Sn}_9\text{Pt}_2(\text{PPh}_3)]^{2-}$  and the proposed balanced equation is summarized in eq. 1.



The crystalline solid of the anion forms very dark red-brown blocks. The complex is air and moisture sensitive in solution and the solid state. The salt is sparingly soluble in en, dimethyl formamide (DMF), acetonitrile (CH<sub>3</sub>CN) and dimethyl sulfoxide (DMSO) to form dark red-brown solutions. The salt has been characterized by single crystal X-ray diffraction, Energy Dispersive X-ray analysis (EDX), <sup>119</sup>Sn NMR spectroscopy, Electrospray Ionization Mass Spectrometry (ESI-MS).

### 4.1.3. Solid State Structure

[K(2,2,2-crypt)]<sub>4</sub>[Ni<sub>2</sub>Sn<sub>17</sub>] salt crystallizes in the monoclinic system, space group I2/a, with an ethylenediamine solvate molecule in the crystal lattice. A summary of the crystal data is given in Table 4.1, and selected bond distances and angles are given in Table 4.2.

The [Ni<sub>2</sub>Sn<sub>17</sub>]<sup>4-</sup> anion (Figure 4.1) possesses crystallographic C<sub>2</sub> symmetry but has virtual D<sub>2d</sub> point symmetry with a mirror plane defined by Sn<sub>8</sub>, Sn<sub>5</sub>, Sn<sub>2</sub>. The anion is defined by 17-vertex Sn atom cluster with two interstitial Ni atoms. The

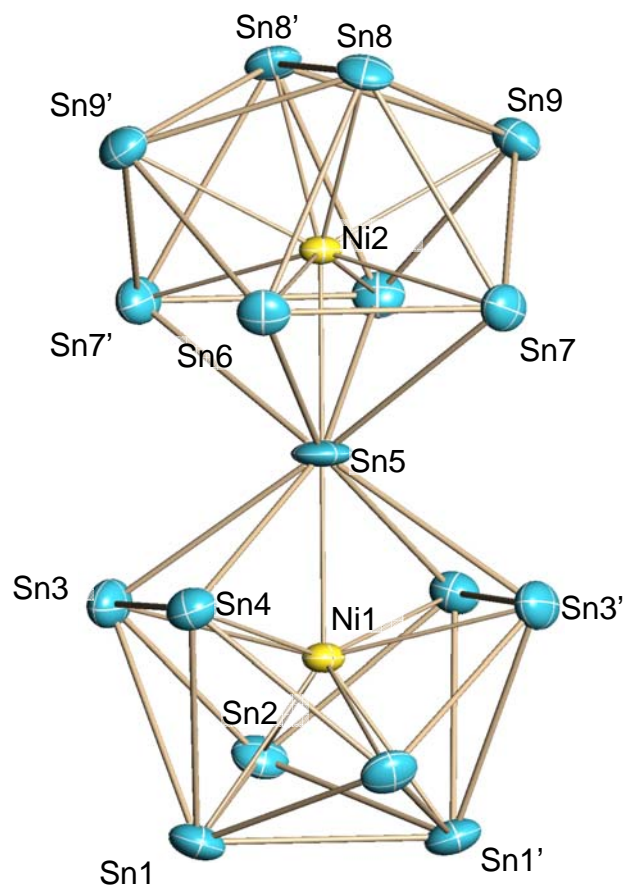


**Figure 4.1.** ORTEP drawing of the  $[\text{Ni}_2\text{Sn}_{17}]^{4+}$  ion. Ni is yellow, Sn is blue, thermal ellipsoids are set at the 50 % probability level.

anion is formed by coupling of two  $\text{Ni}@\text{Sn}_9^{2-}$  clusters that share a common vertex (Sn5). The  $\text{Ni}@\text{Sn}_9^{2-}$  subunits are quite similar to the  $C_{3v}$  structures of related  $[\text{M}@\text{E}_9\text{M}(\text{PPh}_3)]^{2-}$  clusters (M = Ni, E = Ge; M = Pt, E = Sn)<sup>95, 160</sup> but differ from the  $C_{4v}$  structure of  $[\text{Ni}@\text{Sn}_9\text{Ni}(\text{CO})]^{3-}$ . Each  $\text{Ni}@\text{Sn}_9^{2-}$  subunit is a 20 electron,  $2n+2$  cluster and should adopt a *closo*- type architecture according to Wades rules. However, they do not show the expected deltahedral geometry and violate Wades predictions, which is common among centered Zintl anions.<sup>95, 160</sup>

**Table 4.1.** Crystallographic data for the  $[\text{Ni}_2\text{Sn}_{17}]^{4+}$  ion.

<b>Ni<sub>2</sub>Sn<sub>17</sub></b> C76H160K4N12O24	
Compound formula	$[\text{Ni}_2\text{Sn}_{17}]$ $[\text{K}(2,2,2\text{-crypt})_4] \cdot 2 \text{ en}$
Formula weight	3917.71
Temperature (K)	173(2) K
Wavelength (Å)	0.71073
Crystal system	Monoclinic
Space group	I2/a
Unit cell dimensions	
a (Å)	28.7930(14)
b (Å)	16.7444(8)
c (Å)	29.2296(14)
α (deg)	90
β (deg)	116.0240(10)
γ (deg)	90
Volume (Å <sup>3</sup> )	12663.4(11)
Z	4
Dcalc (g/cm <sup>3</sup> )	2.055
Abs coeff (mm <sup>-1</sup> )	3.765
Crystal size (mm <sup>3</sup> )	0.43×0.36×0.11
Reflections collected	44725
Independent reflections	14517 [R(int) = 0.0174]
goodness of fit on F <sup>2</sup>	1.072
Final R indices [ $I > 2\sigma(I)$ ] <sup>a</sup>	
R1	0.0223
wR2	0.0543[12962 Data]
R indices (all data) <sup>a</sup>	
R1	0.0271
wR2	0.0563

a. The function minimized during the full-matrix least-squares refinement was  $\Sigma w(\text{Fo}2 - \text{Fc}2)$  where  $w = 1/[\sigma^2(\text{Fo}2) + (0.0380 * \text{P})^2 + 5.4664 * \text{P}]$  and  $\text{P} = \max(\text{Fo}2, 0) + (2 * \text{Fc}2) / 3$ .

**Table 4.2.** Selected bond lengths [Å] and angles [o] for [Ni<sub>2</sub>Sn<sub>17</sub>] [K(2,2,2-crypt)]<sub>4</sub>• 2en

Ni(1)-Sn(1)	2.6363(4)	Ni(2)-Sn(5)	2.3822(5)
Ni(1)-Sn(2)	2.7315(4)	Ni(2)-Sn(6)	2.6704(3)
Ni(1)-Sn(3)	2.6671(3)	Ni(2)-Sn(7)	2.6784(2)
Ni(1)-Sn(4)	2.6782(2)	Ni(2)-Sn(8)	2.6236(4)
Ni(1)-Sn(5)	2.3865(5)	Ni(2)-Sn(9)	2.7403(3)
Sn(1)-Sn(1')	3.1395(4)	Sn(6)-Sn(8)	3.1872(3)
Sn(1)-Sn(2)	3.0265(3)	Sn(8)-Sn(8')	3.0715(4)
Sn(1)-Sn(3)	3.1565(3)	Sn(6)-Sn(7)	2.9713(3)
Sn(1)-Sn(4)	3.2086(3)	Sn(7)-Sn(9)	3.0089(3)
Sn(2)-Sn(3)	3.0038(3)	Sn(9)-Sn(8')	3.0198(3)
Sn(3)-Sn(4)	2.9767(3)	Sn(9)-Sn(6')	2.9755(3)
Sn(4)-Sn(5)	3.1177(3)	Sn(5)-Sn(7)	3.1396(3)
Sn(5)-Sn(3')	3.1386(3)	Sn(5)-Sn(6)	3.1364(3)
Ni(2)-Sn(5)-Ni(1)	180.0	Sn(5)-Ni(1)-Sn(1')	143.456(8)
Ni(2)-Sn(5)-Sn(4)	123.635(6)	Sn(1')-Ni(1)-Sn(1)	73.089(16)
Ni(1)-Sn(5)-Sn(4)	56.365(6)	Sn(1')-Ni(1)-Sn(3)	131.675(14)
Sn(4)-Sn(5)-Sn(4')	112.729(12)	Sn(3)-Ni(1)-Sn(3')	153.13(2)
Sn(4)-Sn(5)-Sn(6')	162.362(6)	Sn(3')-Ni(1)-Sn(4')	67.682(8)
Sn(4)-Sn(1)-Sn(4)	55.758(7)	Sn(3)-Ni(1)-Sn(4')	105.384(9)
Sn(4)-Sn(3)-Sn(2)	108.835(9)	Sn(5)-Sn(3)-Sn(1)	98.534(8)
Ni(1)-Sn(3)-Sn(5)	47.695(11)	Sn(3)-Sn(4)-Sn(2')	107.898(9)
Sn(2)-Sn(3)-Sn(5)	90.668(8)	Ni(2)-Sn(6)-Sn(7)	56.384(6)
Sn(4)-Sn(3)-Sn(1)	63.007(7)	Sn(8')-Sn(8)-Sn(7)	101.117(7)

The shared vertex Sn5 is in an unusual pseudo-cubic Sn<sub>8</sub> coordination environment with slightly longer Sn-Sn contacts of 3.133 Å, av. Excluding the distances to the Sn5, the Sn-Sn contacts within the cluster average 3.05(8) Å and are similar to other tin complexes (e.g. Sn<sub>9</sub><sup>4+</sup>, d<sub>Sn-Sn</sub> = 2.93 – 3.31 Å, Sn<sub>5</sub><sup>2-</sup>, d<sub>Sn-Sn</sub> = 2.901 – 3.128 Å) and metallated Zintl ions (e.g. [Sn<sub>9</sub>Cr(CO)<sub>3</sub>]<sup>4-</sup>, d<sub>Sn-Sn</sub> = 2.97 – 3.31 Å, [Sn<sub>9</sub>Ni<sub>2</sub>(CO)]<sup>3-</sup>, d<sub>Sn-Sn</sub> = 2.83 – 3.25 Å )<sup>15,18-20</sup> The long contacts to the Sn5 are due to its high coordination number that is more akin to solid state compounds.

The Ni atoms bonding to the central Sn atom (Sn5) for both polymers have same Ni-Sn distance (2.384(3) Å, av). These distances are shorter than other 16 Ni-Sn contacts in the anion (2.68(4) Å, av) indicating compression of the cluster along the Ni2-Sn5-Ni1 vector. The latter distances are similar to those of [Ni@Sn<sub>9</sub>Ni(CO)]<sup>3-</sup> (2.619(4) and 2.681(2) Å) and the predicted distances in [Ni@Sn<sub>10</sub>]<sup>2-</sup> (2.61 - 2.93 Å).<sup>15,22</sup>

#### 4.1.4. NMR Spectroscopic Studies

The low temperature limiting <sup>119</sup>Sn NMR spectrum of [Ni<sub>2</sub>Sn<sub>17</sub>]<sup>4-</sup> at -64 °C (Figure 4.2a) contains four resonances in an approximate 4: 8: 4: 1 integral ratio at δ<sub>1</sub> = -1713, δ<sub>2</sub> = -1049, δ<sub>3</sub> = -1010, δ<sub>4</sub> = 228 ppm, respectively. The number of peaks and their intensities are consistent with the D<sub>2d</sub> structure of the cluster with four different Sn environments. The resonance at δ<sub>2</sub> has the highest peak intensity and is due to the eight equivalent Sn atoms bonded to the central Sn5 atom. The resonance with the lowest intensity, δ<sub>4</sub>, is assigned to the Sn5. Since δ<sub>1</sub> and δ<sub>3</sub> have the same

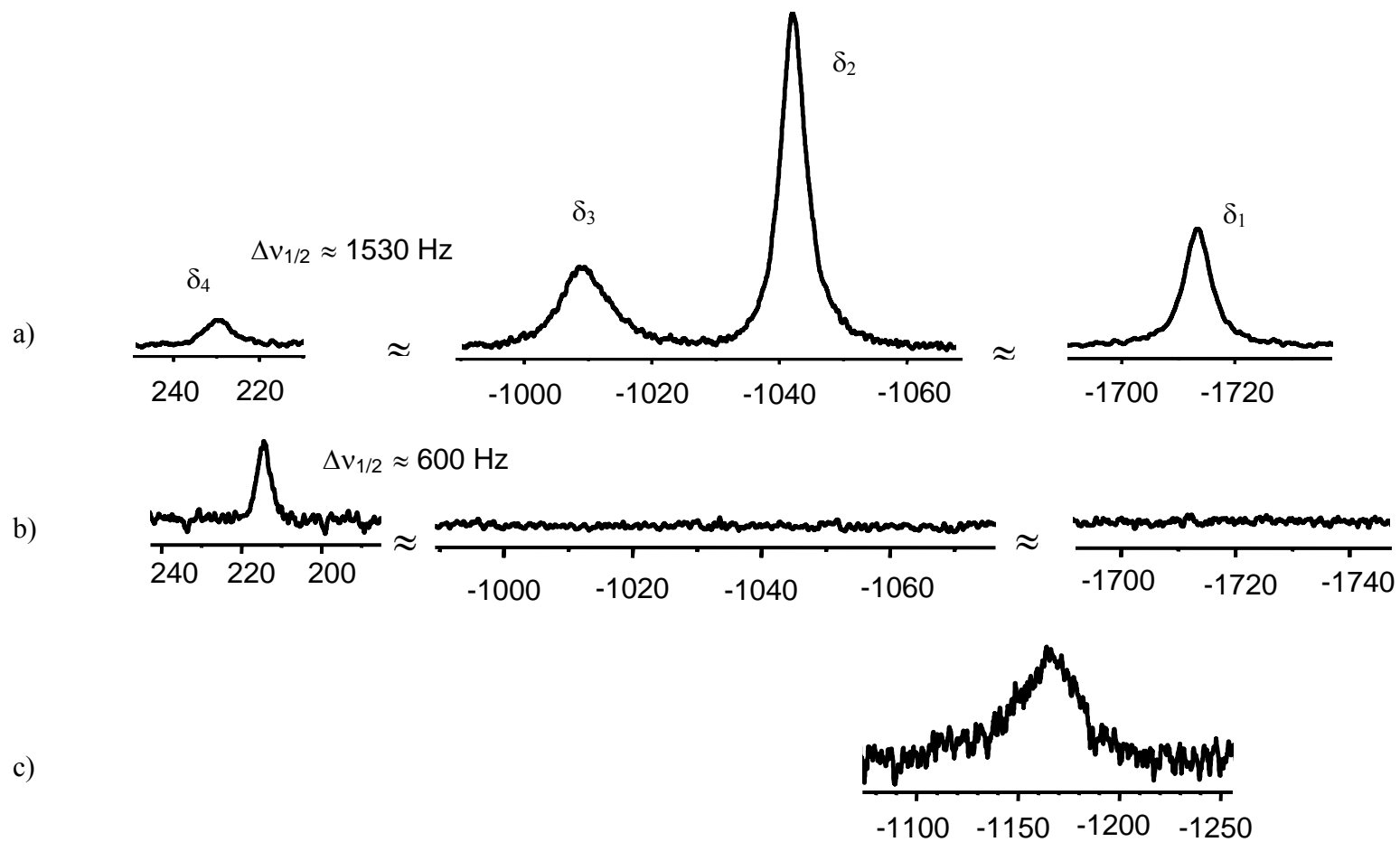


**Figure 4.2.** The  $^{119}\text{Sn}$  NMR spectrum of the  $[\text{Ni}_2\text{Sn}_{17}]^{4+}$  ion recorded in dmf at a)  $-64$  °C b)  $0$  °C and c)  $60$  °C.

integrated area, it is not possible to assign these peaks based on the intensities alone. However, previous studies<sup>18,19</sup> have shown that 4-coordinate capping Sn atoms in Sn9 polyhedra have anomalous downfield chemical shifts. As such, we tentatively assign the 4-coordinate Sn atoms (Sn2 and Sn9) to the downfield resonance  $\delta_3$ .

Upon increasing the temperature to -50 °C, the line widths of the peaks at  $\delta_1$ ,  $\delta_2$ ,  $\delta_3$  increase, while the peak at  $\delta_4$  sharpens. At 0°C,  $\delta_1$ ,  $\delta_2$ ,  $\delta_3$ , disappear into the baseline while  $\delta_4$  remains sharp (Figure 4.2b). At 44 °C, a time averaged exchange peak emerges at -1176 ppm while  $\delta_4$  is broadened but still clearly visible. The exchange peak is close to the expected weighted average of  $\delta_1$ ,  $\delta_2$ ,  $\delta_3$  (-1205 ppm). Increasing the temperature to 60 °C results in the disappearance of the resonance  $\delta_4$  and a shift of the exchange peak downfield to -1167 ppm. (Figure 4.2c) The expected time averaged peak for total exchange is -1120 ppm. The data suggest that an intramolecular exchange process is occurring at low temperature that does not involve the central Sn5 atom. At higher temperatures, global exchange is observed indicating that all Sn atoms, including the unusually coordinated Sn5, are in rapid exchange on the NMR time scale.

#### 4.1.5. Electrospray Mass Spectrometry

The electrospray mass spectrum of **1** was recorded in the negative ion mode from dmf solutions of a crystalline  $[\text{K}(2,2,2\text{-crypt})]_4[\text{Ni}_2\text{Sn}_{17}]$  sample. The spectrum (Figure 4.3) shows the oxidized molecular ion,  $[\text{Ni}_2\text{Sn}_{17}]^{1-}$  (peak P), as well as a strong signal of the  $[\text{K}(2,2,2\text{-crypt})]^+$ -coordinated molecular ion (peak 17). An enlarged view of this peak showing its distinctive mass envelope, and the simulated

pattern is marked as 17'. The spectrum also shows the sequential degradation products of **1**,  $[\text{K}(2,2,2\text{-crypt})\text{Ni}_2\text{Sn}_n]^{1-}$  where  $n = 16$  to  $12$ , due to systematic loss of Sn atoms. This phenomenon was also observed<sup>23</sup> in the gas phase degradation of  $[\text{As}@\text{Ni}_{12}@\text{As}_{20}]^{3-}$  and illustrates the ability of these clusters to fragment and re-nucleate in alternative structures.

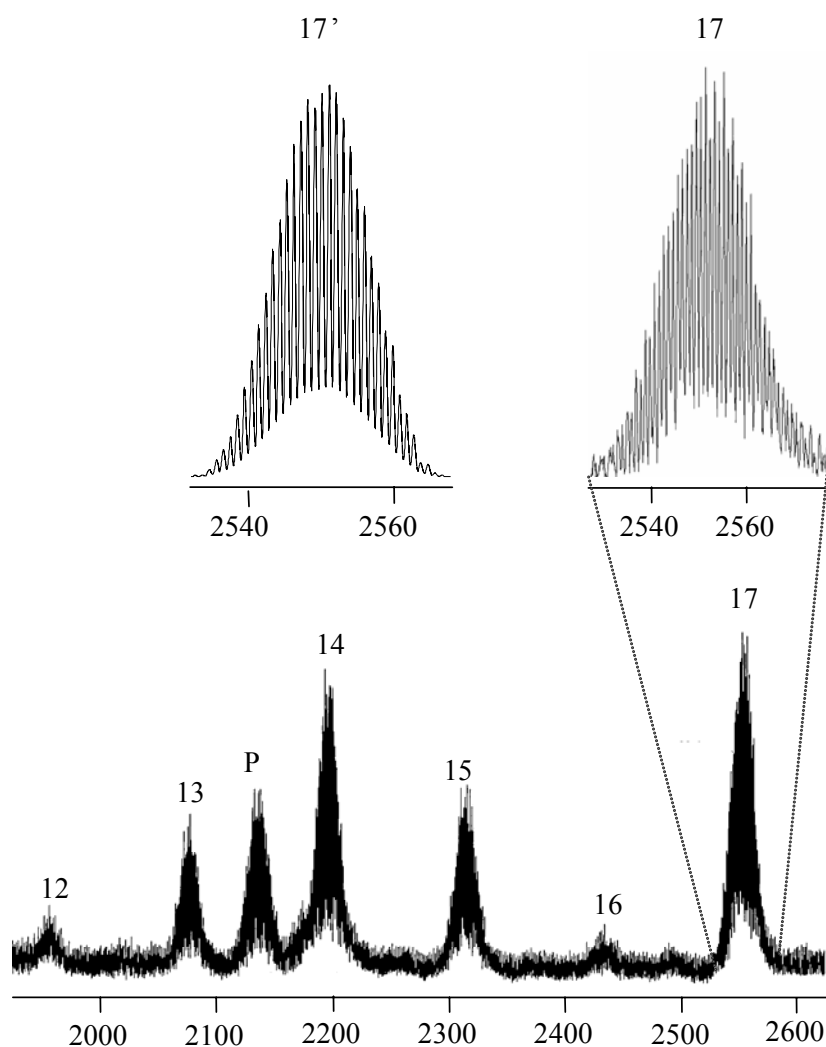


**Figure 4.3.** Negative ion ESI mass spectrum of  $[\text{K}(2,2,2\text{-crypt})]_4[\text{Ni}_2\text{Sn}_{17}]$ . The labels represent the number of Sn atom ( $n$ ) in the  $[\text{K}(2,2,2\text{-crypt})\text{Ni}_2\text{Sn}_n]^{1-}$  series of ions. P is the oxidized  $[\text{Ni}_2\text{Sn}_{17}]^{1-}$  parent ion. The insets show the  $[\text{K}(2,2,2\text{-crypt})]_4[\text{Ni}_2\text{Sn}_{17}]^{1-}$  peak (17) and its simulated pattern (17').

## 4.2. Discussion

The  $[\text{Ni}_2\text{Sn}_{17}]^{4-}$  ion described here is very intriguing with its structure, bonding and surprising dynamic properties. The formation of the anion can be described as an initial incorporation of Ni atom into the nido- $\text{Sn}_9^{4-}$  cluster, presumably followed by coupling of an  $\text{NiSn}_9$  fragment to another by sharing a vertex to form the  $[\text{Ni}_2\text{Sn}_{17}]^{4-}$  complex. For comparison, the dimer and polymers of group 14 Zintl ions formed by oxidative coupling of nine atom deltahedra ( $\text{E}_9^{4-}$ ).<sup>87, 90</sup> They have very different connectivities of the  $\text{E}_9^{4-}$  cluster. For example, the  $[\text{Ge}_9\text{-Ge}_9]^{6-}$  dimer is connected via a 2 center - 2 electron exo bond between the vertices of the two  $\text{Ge}_9$  clusters that have undistorted *closo* geometry.

Similar to  $[\text{Ni}_2\text{Sn}_{17}]^{4-}$ , the formation of complexes encapsulating more than one transition metal inside (two-focus cluster) has been reported in the related studies such as  $[\text{Pd}_2@\text{Ge}_{18}]^{4-}$  and  $[\text{Ni}_3\text{Ge}_{18}]^{4-}$  in different architectures.<sup>99, 100</sup> The former is a single-cage deltahedron, made of 18 Ge atoms centered by a dimer of palladium atoms. The latter anion has two Ni centered  $\text{Ge}_9$  clusters connected by third Ni atom which positioned at an inversion center and forms the tenth shared vertex for each cluster. In contrast, the anion **1** has a structure in which main group metal (Sn) placed at the inversion center and plays the role of shared vertex.

Many of the Zintl clusters of group 14 elements and their transition metal derivatives have been reported to date possess structures that comply Wade-Mingos electron counting rules. There are now several examples that do not. When the charge of the  $[\text{Ni}_2\text{Sn}_{17}]^{4-}$  complex evaluated by the sum of the charges of  $[\text{Ni}@\text{Sn}_9]^{2-}$

subunits, each subunit is a 20 electrons,  $2n+2$  cluster types. However, they do not show a close geometry and demonstrate deviations from Wade type electron counting similar to the other several examples of clusters that do not adopt classical Wadland like structure such as  $[\text{Sn}_9\text{Pt}_2(\text{PPh}_3)]^{2-}$  and  $[\text{Ge}_9\text{Ni}_2(\text{PPh}_3)]^{2-}$  complexes.<sup>15</sup>

The anion 1 comprises a Sn atom (shared vertex Sn5) having an extraordinary coordination number of 8. A tin atom usually exists in the  $\beta$  modification, in which tin atoms are surrounded by six other tin atoms.  $\beta$ -Sn transforms into thermodynamically more stable  $\alpha$ -Sn below 13.2 °C. An  $\alpha$ -Sn has diamond structure with coordination number four.<sup>161</sup> Higher-coordinated Sn atoms occur generally in solid state compounds like binary alkaline earth metal stannide,  $\text{BaSn}_5$ . The compound has Sn atoms coordinated to 12 other Sn atoms in graphite like layers. Coordination number greater than four is also observed in  $\text{Sn}_n^{x-}$  ( $n = 5, 6, 9$ ) Zintl anions. However, the highest coordinated Sn atom in these systems is five, as in  $\text{Sn}_9^{4-}$ <sup>162</sup> and  $[\text{Sn}_6\{\text{Cr}(\text{CO})_5\}_6]^{2-}$ <sup>96</sup>. Therefore, the  $[\text{Ni}_2\text{Sn}_{17}]^{4-}$  anion has the highest coordinated Sn atom in such Zintl ion systems.

One of the most important features of the anion 1 is its spectroscopic / dynamic properties. <sup>119</sup>Sn NMR studies demonstrated that unusual dynamic behavior associated with  $[\text{Ni}_2\text{Sn}_{17}]^{4-}$  ion which possesses capsule-like structure with  $D_{2d}$  point symmetry. The cluster has four distinct chemical environments of the Sn atoms. The <sup>207</sup>Sn NMR analysis at -64 °C revealed that the spectra are consistent with solid state structure of the compound, and it is static on NMR time scale. At 0 °C intramolecular exchange process is observed in between the two ends of the molecule excluding the central Sn5 atom. Upon increasing the temperature, all the seventeen Sn atoms are in

rapid exchange on the NMR time scale. This surprising global atomic mobility is consistent with the dynamic processes in single-focus clusters such as  $[\text{Ni}@\text{Pb}_{10}]^{2-}$  and  $[\text{Sn}_9\text{Pt}_2(\text{PPh}_3)]^{2-}$ , but is apparently operative in two-focus clusters as well. Since the 8-coordinate Sn5 atom has more like solid state Sn coordination environments, and all other 16 Sn atoms are more like surface Sn atoms of a Sn nanoparticle, this process serves as a model for different exchange rates between the surface and the bulk atoms in nanoparticle systems.

### **4.3. Experimental Section**

#### **4.3.1. General Data**

All reactions were performed in a nitrogen atmosphere drybox (Vacuum Atmosphere Co.).  $^{119}\text{Sn}$  NMR spectrum was recorded on a Bruker DRX500 Avance spectrometer operating at 186.5 MHz. Electrospray Mass Spectra (ESI-MS) was performed on a Accu TOF CS TMS-T100CS instrument. Dmf solutions are directly injected into the instrument and samples were detected in the negative ion mode. An AMRAY 1820K scanning electron microscope with a potential of 20 kV was used for energy dispersive X-ray (EDX) studies. Single crystal X-ray analysis was performed by Dr. James Fettingner on a Bruker CCD system at  $-80\text{ }^\circ\text{C}$ . The SHELXTL program package was used for data processing, structure solution and refinement.

#### **4.3.2. Chemicals**

Melts of nominal composition  $\text{K}_4\text{Sn}_9$  was made by fusion ( $\sim 1000^\circ\text{C}$ ) of stoichiometric ratios of the elements. The chemicals were sealed in evacuated, silica

tubes and heated carefully with a natural gas/oxygen flame. 4,7,13,16,21,24-Hexaoxa-1,10-diazobicyclo[8,8,8]-hexacosane (2,2,2-crypt) was purchased from Aldrich. Bis-cyclooctadiene Nickel(0), Ni(COD)<sub>2</sub>, was purchased from STREM Chemicals. Anhydrous ethylenediamine (en) and dimethylformamide (DMF) were purchased from Fisher, vacuum distilled from K<sub>4</sub>Sn<sub>9</sub>, and stored under dinitrogen. Toluene was distilled from sodium under dinitrogen and stored under dinitrogen.

### 4.3.3. Synthesis

#### 4.3.3.1. Preparation of [K(2,2,2-crypt)]<sub>4</sub>[Ni<sub>2</sub>Sn<sub>17</sub>]·2en.

In vial 1 K<sub>4</sub>Sn<sub>9</sub> (80mg, 0.065 mmol), 2,2,2-crypt (98 mg, 0.26 mmol) were dissolved in en (ca. 2mL) and stirred for 5 min., yielding a dark red solution. In vial 2, Ni(COD)<sub>2</sub> (18 mg, 0.065 mmol) were dissolved in toluene (ca. 1mL) producing pale yellow solution. The contents of vial 2 were added to the contents of vial 1. The reaction mixture was stirred for 4h yielding red-brown solution. The reaction mixture was then filtered through tightly packed glass wool in a pipet. Dark red-brown, crystals formed in reaction vessel after 10 days. After 10 days big, pyramid shaped, dark red-brown crystals of [K(2,2,2-crypt)]<sub>4</sub>[Ni<sub>2</sub>Sn<sub>17</sub>]·2en are precipitated. Yield ; ~ 25 mg (~20 %). EDX Sn:Ni:K = 8.8 : 1 : 2. <sup>119</sup>Sn NMR (186.5 MHz, dmf, -64 °C): δ = -1713, -1046, -1010, 228 ppm. ESI-MS data: (m/z, ion) 2550.5 [K(2,2,2-crypt)Ni<sub>2</sub>Sn<sub>17</sub>]<sup>1-</sup>; 2136 [Ni<sub>2</sub>Sn<sub>17</sub>]<sup>1-</sup>; 2431 [K(2,2,2-crypt)Ni<sub>2</sub>Sn<sub>16</sub>]<sup>1-</sup>; 2314 [K(2,2,2-crypt)Ni<sub>2</sub>Sn<sub>15</sub>]<sup>1-</sup>; 2194 [K(2,2,2-crypt)Ni<sub>2</sub>Sn<sub>14</sub>]<sup>1-</sup>; 2076 [K(2,2,2-crypt)Ni<sub>2</sub>Sn<sub>13</sub>]<sup>1-</sup>; 1957 [K(2,2,2-crypt)Ni<sub>2</sub>Sn<sub>12</sub>]<sup>1-</sup>.

#### **4.3.3.2. Crystallographic Studies**

The crystal structures of the complexes were determined at single crystal X-ray facility at Chemistry and Biochemistry Department, University of Maryland, by Dr. James Fettingner.

## Chapter 5

# Synthesis and Characterization of the $[\text{Ni}_6\text{Ge}_{13}(\text{CO})_5]^{4-}$ and $[\text{Ge}_9\text{Ni}_2(\text{PPh}_3)]^{2-}$ Zintl ion Clusters

### 5.1. Introduction

Free standing, transition metal stabilized Zintl anions have attracted great interest due to their fullerene-like properties,<sup>140, 163-165</sup> their unusual molecular and electronic structures<sup>39, 42</sup> and their potential utility as precursors to bimetallic alloys and intermetallics.<sup>57, 166</sup> The reaction of nine atom clusters of group 14 Zintl ions (i.e.  $\text{Ge}_9^{4-}$ ,  $\text{Sn}_9^{4-}$ ,  $\text{Pb}_9^{4-}$ ) with labile transition metal precursors results in the formation of transition metal centered, highly symmetric clusters such as  $[\text{M}@\text{Pb}_{12}]^{2-}$  and  $[\text{M}@\text{Pb}_{10}]^{2-}$  ions where  $\text{M} = \text{Ni}, \text{Pd}, \text{Pt}$ ,<sup>130, 134, 167</sup> and the recently reported  $[\text{Pd}_2@\text{Ge}_{18}]^{4-}$  and  $[\text{Ni}_3@\text{Ge}_{18}]^{4-}$  clusters.<sup>99, 100</sup> The structures of these clusters rely on both the steric demands of the constituent elements and the cluster electron count. While most of them have structures, which are predicted by Wades rules, akin to boranes,<sup>86</sup> others, such as  $[\text{Sn}_9\text{Pt}_2(\text{PPh}_3)]^{2-}$ , seem to violate Wade's structure prediction principles.<sup>95</sup> The latter complex has 20 cluster electrons with 10 surface vertices, which corresponds to a hypo-*closo* system in a Wade type analysis. In contrast to the expected closed, deltahedral type, the observed structure is a more

open, *nido*-like framework<sup>168</sup> with fewer Sn-Sn contacts than predicted. This structural difference is most likely because of the steric demands of the centered Pt atom and the weak nature of the Sn-Sn bonds. On the other hand, the closely related  $[\text{Sn}_9\text{Ni}_2(\text{CO})]^{3-}$ , which has a smaller Ni interstitial, adopts the expected *closo* structure consistent with its 21 electrons,  $2n+1$  configuration.<sup>95</sup>

Early studies showed that group 14 Zintl ions involved  $\text{ML}_n$  fragments, which did not contribute electrons to the cluster bonding, were not expected to change the cluster electron count or Zintl ion precursor framework structure. For example, the 9-vertex, 22-electron *nido*- $\text{Sn}_9^{4-}$  complex forms the expected 10-vertex, 22-electron *closo*- $[\text{Sn}_9\text{M}(\text{CO}_3)]^{4-}$  series of complexes (M = Cr, Mo, W).<sup>169</sup> The first transition metal polygermanide was prepared from the reaction between  $\text{Ge}_9^{4-}$  and  $\text{Ni}(\text{CO})_2(\text{PPh}_3)_2$  in ethylenediamine solvent. The product was characterized as  $[\text{K}(2,2,2\text{-crypt})]_2[\text{Ge}_9(\mu_{10}\text{-Ge})\text{Ni}(\text{PPh}_3)]$  on the basis of X-ray analysis and Wade's electron counting principles.<sup>170</sup> By inserting an interstitial Ge instead of an interstitial Ni atom, one achieves a *nido* electron count that is consistent with the observed *nido*-like structure. The discovery<sup>95</sup> of the isostructural  $[\text{Sn}_9\text{Pt}_2(\text{PPh}_3)]^{2-}$  ion that violates Wades rules prompted us to reinvestigate the identity of the  $[\text{Ge}_9(\mu_{10}\text{-Ge})\text{Ni}(\text{PPh}_3)]^{2-}$  ion by way of electrospray mass spectrometry (ESI-MS) and a new single crystal X-ray analysis. During the course of the investigation, a new type of transition metal Zintl cluster,  $[\text{Ge}_{13}\text{Ni}_6(\text{CO})_5]^{4-}$ , was also discovered.<sup>171, 172</sup> This chapter presents synthesis and characterization of this new anion having an interpenetrating biicosahedral structure, and the correct structure and composition of the  $[\text{Ge}_9\text{Ni}_2(\text{PPh}_3)]^{2-}$  ion that was previously described<sup>170</sup> as the  $[\text{Ge}_9(\mu_{10}\text{-Ge})\text{Ni}(\text{PPh}_3)]^{2-}$

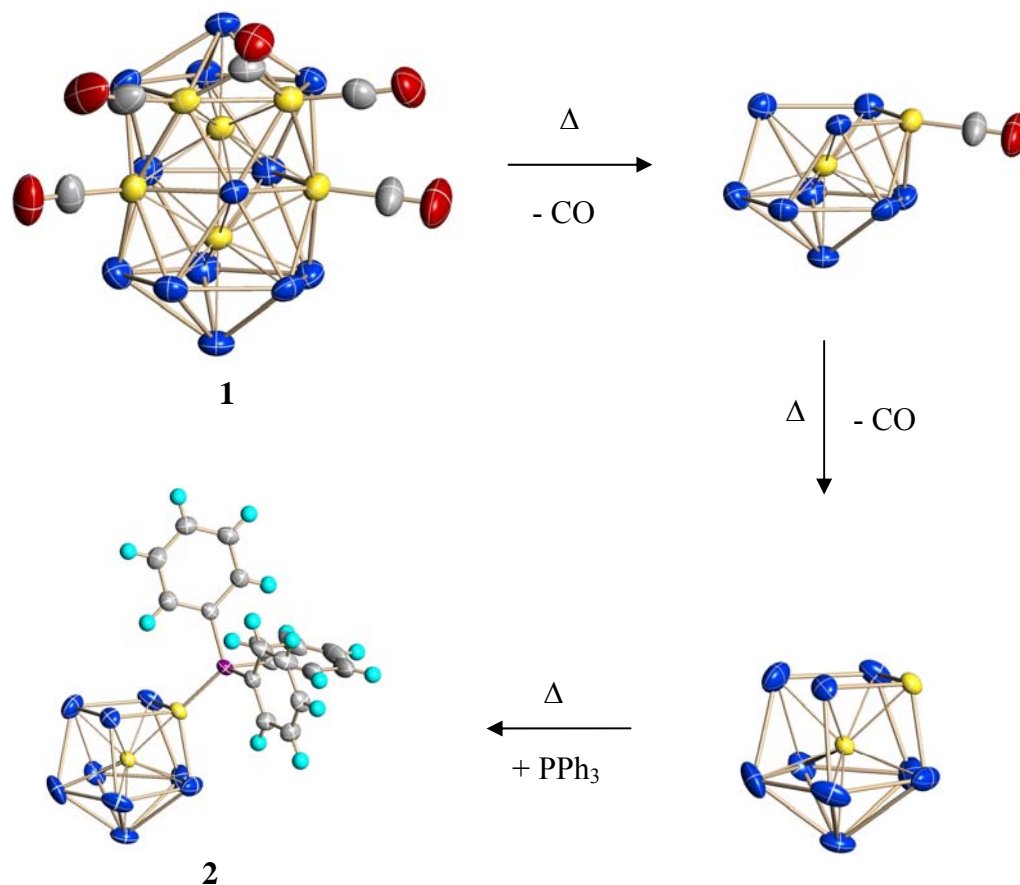
ion. The interconversion of these complexes and their relationships to other transition metal group 14 Zintl complexes are described.

## 5.2. Results and Discussion

### 5.2.1. Synthesis

The reaction of  $\text{K}_4\text{Ge}_9$ ,  $[\text{Ni}(\text{CO})_2(\text{PPh}_3)_2]$  and four equivalents of 2,2,2-crypt in ethylenediamine (en) gives two different products depending on reaction conditions. At moderate temperatures ( $30\text{ }^\circ\text{C} < T < 40\text{ }^\circ\text{C}$ ), small, dark brown crystals of  $[\text{Ni}_6\text{Ge}_{13}(\text{CO})_5]^{4-}$  (**1**) formed as the  $[\text{K}(2,2,2\text{-crypt})]^+$  salt in moderate yield. The  $[\text{K}(2,2,2\text{-crypt})]^+$  salt of **1** is air and moisture sensitive in solution and the solid state. The salt is highly soluble in DMF and  $\text{CH}_3\text{CN}$  and forms dark brown solutions. The 19-atom cluster has a fused biicosahedral capsule-like structure with 17 Ge/Ni vertices and 2 centered Ni atoms. The structure and properties of this cluster will be discussed in subsequent sections.

At higher temperatures ( $T \sim 118\text{ }^\circ\text{C}$ ), the same reaction yields the  $[\text{Ge}_9\text{Ni}_2(\text{PPh}_3)]^{2-}$  ion (**2**) in moderate yields, which crystallizes as large, block-like dark brown crystals of the  $[\text{K}(2,2,2\text{-crypt})]^+$  salt. The structure of the anion has 1 Ni and 9 Ge vertices with a centered Ni atom and will also be discussed in subsequent sections. Both complexes have been characterized by single-crystal X-ray diffraction, NMR spectroscopy ( $^{13}\text{C}$  and  $^{31}\text{P}$  where appropriate), Energy Dispersive X-ray analysis (EDX), electrospray ionization mass spectrometry (ESI-MS) and Infrared Spectroscopy.



**Scheme 5.1**

A proposed scheme for the interconversion of the anions **1** and **2** is illustrated in Scheme 5.1. The transformation involves the initial formation of the cluster anion  $[\text{Ni}_6\text{Ge}_{13}(\text{CO})_5]^{4-}$  (**1**) followed by an irreversible conversion to  $[\text{Ge}_9\text{Ni}_2(\text{PPh}_3)]^{2-}$  (**2**). This conclusion is based on the following results and observations:

i) The same Ni precursor,  $\text{Ni}(\text{CO})_2(\text{PPh}_3)_2$ , is used in the synthesis of **1** and **2**. However, the anion **1** is isolated from reactions conducted at relatively lower temperatures (35 - 40 °C) and short reaction times whereas the formation of **1** is favored at high temperatures and long reaction times.

ii) Electrospray mass spectra of DMF solutions of **1** (see section 5.2.4. ) show anion **1** as well as,  $[\text{Ge}_9\text{Ni}_2(\text{CO})]^-$  and  $[\text{Ge}_9\text{Ni}_2]^-$ , that result from fragmentation of the parent. These ions have the same  $\text{Ge}_9\text{Ni}_2$  core composition of **2**.

iii) Addition of  $\text{PPh}_3$  to en solutions of pure  $[\text{K}(2,2,2\text{-crypt})]_4[\text{Ni}_6\text{Ge}_{13}(\text{CO})_5]$  results in the formation of **2** after  $\sim 30$  min of reaction at  $118^\circ\text{C}$ . The ESI MS spectra of these solutions show signals corresponding to  $\text{K}[\text{Ge}_9\text{Ni}_2(\text{PPh}_3)]^{1-}$  and  $[\text{Ge}_9\text{Ni}_2(\text{PPh}_3)]^{1-}$  ions, that coincide with those of the authentic sample.

iv) Reactions between **2** and carbon monoxide result in cluster decomposition but do not regenerate **1** or result in the formation of  $[\text{Ge}_9\text{Ni}_2(\text{CO})]^-$  according to ESI MS analysis.

While these experiments show that **2** can be generated from **1** under appropriate conditions, they do not prevent the direct formation of **2** from  $\text{Ge}_9^{4-}$  and  $\text{Ni}(\text{CO})_2(\text{PPh}_3)_2$ . Indeed, the synthesis of closely related clusters such as  $[\text{Sn}_9\text{Pt}_2(\text{PPh}_3)]^{2-}$  appear to form directly from  $\text{Sn}_9^{4-}$  with sequential addition of Pt fragments (NMR analysis)<sup>95</sup> and do not seem to involve intermediates akin to **1**. Moreover, the proposed mechanism for the formation of the closely related  $[\text{Ni}_3@\text{Ge}_{18}]^{4-}$  involves direct insertion of Ni into a  $\text{Ge}_9$  cluster and a subsequent coupling.<sup>100</sup>

### 5.2.2. Solid State Structures

The  $[\text{Ni}_6\text{Ge}_{13}(\text{CO})_5]^{4-}$  (**1**) and  $[\text{Ge}_9\text{Ni}_2(\text{PPh}_3)]^{2-}$  (**2**) anions crystallize as the  $[\text{K}(2,2,2\text{-crypt})]^+$  salts with triclinic crystal symmetry, space group P-1. The former has 1.5 en solvate molecules per formula unit. A summary of the crystal data is given

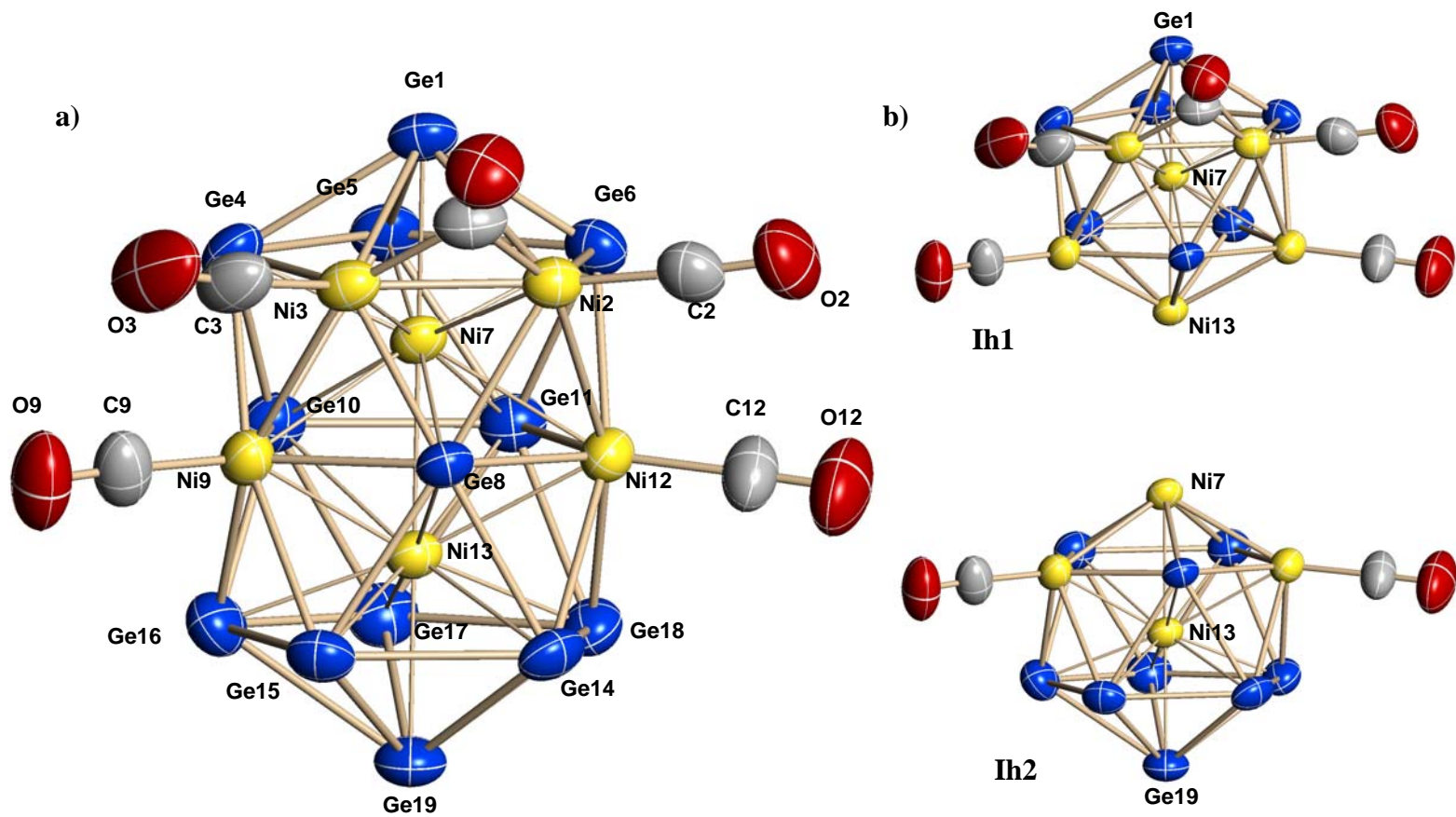


**Figure 5.1.** a) ORTEP drawing of the  $[\text{Ni}_6\text{Ge}_{13}(\text{CO})_5]^{4+}$  anion. Ni is yellow, Ge is blue, C is gray and oxygen is red. b) The two interpenetrating icosahedral subunits, Ih1 and Ih2.

in Table 5.1, and selected bond distances are given in Table 5.2 and Table 5.3, respectively. A previous report of the  $[\text{K}(2,2,2\text{-crypt})]_2[\text{Ge}_9\text{Ni}_2(\text{PPh}_3)]$  structure was incorrectly characterized as having an anion formula  $[\text{Ge}_{10}\text{Ni}(\text{PPh}_3)]^{2-}$ . This interpretation is corrected in this study and a new refinement of the crystal structure from new X-Ray data is presented.

The  $[\text{Ni}_6\text{Ge}_{13}(\text{CO})_5]^{4-}$  anion possesses  $C_s$  point symmetry with a symmetry plane defined by Ge1, Ge8, Ge19 and the bridging carbonyl (Figure 5.2). The anion is a 17-vertex deltahedral cluster defined by 13 Ge atoms and 4 Ni atoms. The cluster is centered by two additional interstitial Ni atoms. Each of the 4 vertex Ni atoms has a terminal CO ligand bound in a radial fashion with an additional bridging CO spanning the Ni2-Ni3 edge. The 17-atom deltahedron possesses 126 total valence electrons and has 32 cluster electrons according to Wades rules of electron counting.<sup>86</sup> According to Wades Rules, each of the Ge atoms contributes 2 electrons whereas each Ni(CO) vertex unit and interstitial Ni contributes zero electrons. The bridging CO ligand and the cluster charge contribute 2 and 4 electrons respectively to give 32 cluster electrons.

$$13 \times 2 (\text{Ge}) + 2 (\text{CO}) + 4 (\text{charge}) = 32e.$$

The 17-vertex, 32 electron cluster corresponds to a hypo-closo electron count and is consistent with the closed, deltahedral structure type.

The  $[\text{Ni}_6\text{Ge}_{13}(\text{CO})_5]^{4-}$  structure can be viewed as two interpenetrating icosahedral units (**Ih1** and **Ih2**) that share the central  $\text{Ge}_3\text{Ni}_2(\text{CO})_2$  pentagonal ring and the 2 interstitial Ni atoms of the biicosahedral cluster (see Figure 5.1b). **Ih1** has a composition  $\text{Ge}_7\text{Ni}_6(\text{CO})_5$  where Ni7 is interstitial and Ni13 occupies a vertex. **Ih2**

**Table 5.1.** Summary of Crystallographic Data for the  $[\text{Ni}_6\text{Ge}_{13}(\text{CO})_5]^{4+}$  and  $[\text{Ge}_9\text{Ni}_2(\text{PPh}_3)]^{2-}$  Ions.

	$[\text{Ni}_6\text{Ge}_{13}(\text{CO})_5]^{4+}$ [K(2,2,2-crypt)]2[2]•en	$[\text{Ge}_9\text{Ni}_2(\text{PPh}_3)]^{2-}$ [K(2,2,2-crypt)]4[1]•1.5en
Empirical formula	Ni6Ge13 C78.5H150 K4N9.5O29	Ge9Ni2 C56H95 K2N6O12P
Formula weight	3143.41	1924.28
Temperature (K)	193(2) K	173(2)
Wavelength (Å)	0.71073	0.71073
Crystal system	triclinic	triclinic
Space group	P-1	P-1
a (Å)	15.2287(4)	12.9083(11)
b (Å)	16.1988(4)	13.0373(11)
c (Å)	26.1824(7)	23.569(2)
$\alpha$ (deg)	92.7560(10)	96.546(2)
$\beta$ (deg)	91.3490(10)	104.757(2)
$\gamma$ (deg)	11.2730(10)	96.868(2)
Volume (Å <sup>3</sup> )	6006.0(3)	3764.7(6)
Z	2	2
Dcalc (g/cm <sup>3</sup> )	1.738	1.698
Abs coeff (mm <sup>-1</sup> )	4.319	4.212
Data/restraints/parameters	27463/2340/1437	17295/5/790
Goodness of fit on F <sup>2</sup>	1.118	1.029
Final R indices [I > 2 $\sigma$ (I)] <sup>a</sup>		
R1	0.0549	0.0428
wR2	0.1794	0.1007
R indices (all data) <sup>a</sup>		
R1	0.0839	0.0834
wR2	0.1936	0.1111

a. The function minimized during the full-matrix least-squares refinement was  $\sum w(\text{Fo}^2 - \text{Fc}^2)$  where  $w = 1/[\sigma^2(\text{Fo}^2) + (0.0380 * \text{P})^2 + 5.4664 * \text{P}]$  and  $\text{P} = \max(\text{Fo}^2, 0) + (2 * \text{Fc}^2) / 3$ .

has a  $\text{Ge}_9\text{Ni}_4(\text{CO})_2$  composition where Ni7 occupies a vertex and Ni13 occupies the interstitial site. This type of interpenetrating biicosahedral structure is new for transition metal Zintl clusters but is known in some of Teo's bimetallic Au-Ag and trimetallic Au-Ag-M; M = Pt, Pd, Ni supraclusters. In particular, the structure of **1** is highly reminiscent of the *sss* rotamer of the  $[(\text{PPh}_3)_{10}\text{Au}_{13}\text{Ag}_{12}\text{Br}_8]^+$  triicosahedral cluster.<sup>172</sup>

The Ge-Ge, Ni-Ni, and Ni-Ge bond distances are in the range of 2.658(1) to 2.894(1) Å (avg. 2.746(4) Å), 2.450(1) - 2.771(1) Å (avg. 2.624 (4) Å), and 2.381(1) - 2.668(1) Å (avg. 2.522 (5) Å), respectively (see Table 5.2). As expected, Ni- $\text{CO}_{(\text{terminal})}$  contacts (avg. 1.718(8) Å) are shorter than the Ni- $\text{CO}_{(\text{bridge})}$  contacts (avg. 1.879(8) Å). The structure is slightly flattened along the Ge8 – Ge17 and Ge8 – Ge5 vectors. This distortion is best illustrated by the differences between the 6 diagonal distances in each of the icosahedral subunit. In both of the icosahedral cages, diagonal distances involving Ge8, (Ge8 – Ge5 = 4.812(1) Å for **Ih1**, and Ge8 – Ge17 = 4.878(2) Å for **Ih2**) are shorter than the other 5 diagonals in the respective subunits (5.087(5) Å, avg. for **Ih1**, and 5.115(4) Å avg. for **Ih2**).

The Ge-Ge bond distances for the anion **1** (2.6335(9) – 2.9064(11); 2.750(6) Å avg.) are similar to those in other polygermenide clusters such as  $[\text{K}(2,2,2\text{-crypt})]_3$   $[\text{P}(\text{C}_6\text{H}_5)_3\text{Ge}_9]$ , where Ge-Ge distances vary from 2.53 to 3.27 Å.<sup>90, 173, 174</sup> The Ni-Ge (2.3808(9) - 2.6681(11) Å; 2.523(5) Å av.) and Ni-Ni (2.450(1) - 2.771(1) Å, 2.624(4) Å av.) contacts are similar to the reported compounds (2.470 to 2.691 Å and 2.553 to 2.721 Å, respectively).<sup>103</sup>

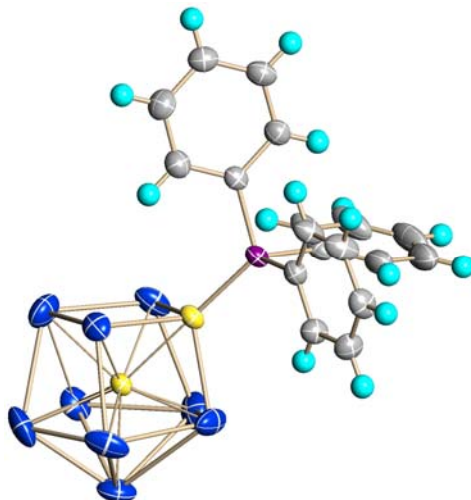


**Figure 5.2** ORTEP drawing of the  $[\text{Ge}_9\text{Ni}_2(\text{PPh}_3)]^{2-}$  anion, (2) Ni is yellow, Ge is blue, C is gray, P is purple and H is turquoise.

As mentioned previously, the structure of the  $[\text{Ge}_9\text{Ni}_2(\text{PPh}_3)]^{2-}$  ion, (2), was incorrectly reported as  $[\text{Ge}_{10}\text{Ni}(\text{PPh}_3)]^{2-}$  in which the interstitial atom was refined as Ge. The formula has been unequivocally established by ESI-MS studies and the structure re-determined. The structure (Figure 5.2) is identical to that previously reported except for the identity of the centered atom. The anion has virtual  $C_{3v}$  point symmetry and is isoelectronic and isostructural to  $[\text{Sn}_9\text{Pt}_2(\text{PPh}_3)]^{2-}$ .<sup>95</sup> It is defined by nine surface Ge atoms, one interstitial Ni atom and a capping  $[\text{Ni}(\text{PPh}_3)]$  fragment. The cluster is a 10-vertex 20-electron *hypo-closo* system that has an open, *nido*-like structure. For comparison, it is isostructural to the 24-electron 10-vertex  $[\text{Sb}_7\text{Ni}_3(\text{CO})_3]^{3-}$  ion that adopts a *nido*-type architecture.<sup>175</sup> Note that replacing the centered Ni atom with a Ge atom would add 4 electrons to cluster bonding and would be consistent with the observed structure. Although this does not occur, this electron counting rationale gave rise to the erroneous assignment in the original publication.<sup>170</sup>

**Table 5.2.** Selected bond distances [Å] and angles [°] for the  $[\text{Ge}_{13}\text{Ni}_6(\text{CO})_5]^{4-}$  ion.

Ge(1)-Ni(2)	2.668(1)	Ge(8)-Ni(9)	2.497(1)
Ge(1)-Ni(7)	2.474(1)	Ge(10)-Ni(7)	2.522(1)
Ge(4)-Ni(3)	2.610(1)	Ge(10)-Ni(9)	2.574(1)
Ge(4)-Ni(7)	2.438(1)	Ge(10)-Ni(13)	2.595(1)
Ge(4)-Ni(9)	2.557(1)	Ge(14)-Ni(12)	2.666(1)
Ge(5)-Ni(7)	2.431(1)	Ge(14)-Ni(13)	2.575(1)
Ge(8)-Ni(2)	2.508(1)	Ge(15)-Ni(9)	2.605(1)
Ge(8)-Ni(7)	2.381(1)	Ge(16)-Ni(13)	2.499(1)
Ge(1)-Ge(4)	2.658(1)	Ge(10)-Ge(16)	2.638(1)
Ge(1)-Ge(5)	2.906(1)	Ge(10)-Ge(17)	2.820(1)
Ge(4)-Ge(5)	2.892(1)	Ge(14)-Ge(15)	2.749(1)
Ge(4)-Ge(10)	2.735(1)	Ge(14)-Ge(19)	2.741(1)
Ge(5)-Ge(10)	2.659(1)	Ge(15)-Ge(16)	2.675(1)
Ge(5)-Ge(11)	2.706(1)	Ge(16)-Ge(17)	2.777(1)
Ge(8)-Ge(15)	2.703(1)	Ge(16)-Ge(19)	2.808(1)
Ge(10)-Ge(11)	2.862(1)	Ge(17)-Ge(19)	2.772(1)
Ni(2)-Ni(7)	2.606(1)	Ni(2)-C(2)	1.694(8)
Ni(2)-Ni(12)	2.742(1)	Ni(2)-C(23')	1.859(8)
Ni(3)-Ni(9)	2.771(1)	Ni(3)-C(3)	1.712(8)
Ni(7)-Ni(13)	2.564(1)	Ni(3)-C(23')	1.898(8)
Ni(7)-Ni(9)	2.637(1)	Ni(9)-C(9)	1.715(8)
Ni(9)-Ni(13)	2.610(1)	Ni(12)-C(12)	1.750(8)
Ni(2)-Ge(1)-Ni(3)	54.80(3)	Ge(8)-Ni(13)-Ge(15)	65.11(3)
Ge(4)-Ge(1)-Ge(5)	62.44(3)	Ge(16)-Ni(13)-Ni(12)	171.06(4)
Ge(4)-Ge(5)-Ge(6)	97.67(3)	Ge(19)-Ni(13)-Ni(7)	176.55(4)
Ge(1)-Ni(7)-Ni(13)	173.03(4)	Ge(16)-Ni(17)-Ge(18)	106.81(3)
Ge(5)-Ni(7)-Ge(8)	173.04(4)	C(23')-Ni(2)-Ge(6)	140.70(2)
Ge(6)-Ni(7)-Ni(9)	169.49(4)	C(3)-Ni(3)-C(23)	106.10(4)
Ge(4)-Ni(9)-Ge(16)	122.46(4)	C(9)-Ni(9)-Ge(8)	127.50(3)
Ge(6)-Ge(11)-Ge(17)	157.25(4)	Ni(3)-C(23')-Ni(2)	81.40(2)

**Table 5.3.** Selected bond distances [Å] and angles [°] for the [Ge<sub>9</sub>Ni<sub>2</sub>(PPh<sub>3</sub>)<sub>2</sub>]<sup>2-</sup> ion.

Ni(1)-P(1)	2.121(1)	Ge(2)-Ge(3)	2.634(1)
Ge(1)-Ni(1)	2.381(1)	Ge(2)-Ge(5)	2.722(1)
Ge(3)-Ni(1)	2.371(1)	Ge(2)-Ge(6)	2.733(1)
Ge(9)-Ni(1)	2.370(1)	Ge(3)-Ge(4)	2.594(1)
Ni(1)-Ni(2)	2.359(1)	Ge(4)-Ge(9)	2.633(1)
Ge(1)-Ni(2)	2.350(1)	Ge(4)-Ge(7)	2.692(1)
Ge(2)-Ni(2)	2.433(1)	Ge(4)-Ge(5)	2.788(1)
Ge(3)-Ni(2)	2.368(1)	Ge(5)-Ge(7)	2.642(1)
P(1)-C(1)	1.847(4)	Ge(5)-Ge(6)	2.656(1)
P(1)-C(2)	1.843(4)	Ge(6)-Ge(7)	2.657(1)
P(1)-C(3)	1.840(4)	Ge(6)-Ge(8)	2.808(1)
Ge(1)-Ge(2)	2.640(1)	Ge(7)-Ge(8)	2.692(1)
Ge(1)-Ge(8)	2.608(1)	Ge(8)-Ge(9)	2.635(1)
Ni(2)-Ge(1)-Ni(1)	59.82(2)	Ge(1)-Ni(2)-Ni(1)	60.75(2)
Ni(1)-Ge(1)-Ge(8)	92.35(3)	Ge(1)-Ni(2)-Ge(3)	103.73(3)
Ni(1)-Ge(1)-Ge(2)	82.29(2)	Ge(1)-Ni(2)-Ge(7)	128.30(3)
Ge(8)-Ge(1)-Ge(2)	108.20(2)	Ni(1)-Ni(2)-Ge(7)	148.06(3)
Ni(2)-Ge(2)-Ge(3)	55.56(2)	Ge(3)-Ni(2)-Ge(8)	157.16(3)
Ge(3)-Ge(2)-Ge(1)	89.45(2)	Ni(2)-Ni(1)-Ge(3)	60.08(2)
Ge(3)-Ge(2)-Ge(5)	68.03(2)	P(1)-Ni(1)-Ni(2)	177.23(4)
Ge(1)-Ge(2)-Ge(5)	107.92(2)	P(1)-Ni(1)-Ge(9)	122.79(4)
Ni(2)-Ge(4)-Ge(3)	56.16(2)	P(1)-Ni(1)-Ge(3)	117.45(4)
Ge(3)-Ge(4)-Ge(9)	82.94(2)	C(1)-P(1)-Ni(1)	119.34(1)
Ge(9)-Ge(4)-Ge(7)	76.38(2)	C(2)-P(1)-Ni(1)	112.37(1)
Ge(9)-Ge(4)-Ge(5)	109.40(2)	C(2)-P(1)-C(1)	100.69(2)
Ge(7)-Ge(4)-Ge(5)	57.60(2)	C(3)-P(1)-C(2)	102.21(2)
Ge(9)-Ni(2)-Ge(1)	94.80(3)	C(3)-P(1)-C(1)	117.79(1)

The centered Ni atom has nine Ni-Ge contacts in the range of 2.342(6) to 2.447(6) Å. The 3 Ni-Ge bonds to Ni1 average 2.37(2) Å. The Ge-Ge contacts are in the range 2.594(1) – 2.808(1) Å and are typical of polygerminide cages.

### 5.2.3. NMR Spectroscopic Studies

The  $^{13}\text{C}$  NMR spectrum of  $[\text{Ni}_6\text{Ge}_{13}(\text{CO})_5]^{4+}$  (DMSO- $d_6$ , 25 °C) shows carbonyl resonances at 194.6, 217.9, 224.9 ppm, which is consistent with the solid state structure.

Room temperature  $^{31}\text{P}$  NMR spectrum of  $[\text{Ge}_9\text{Ni}_2(\text{PPh}_3)]^{2-}$  crystals shows only free triphenylphosphine in DMF solution ( $\delta = -5.1$  ppm), suggesting that  $\text{PPh}_3$  ligand dissociation is fast on the NMR time scale. This observation is somewhat surprising in view of the static nature of the  $\text{PPh}_3$  ligand in the isoelectronic, isostructural  $[\text{Sn}_9\text{Pt}_2(\text{PPh}_3)]^{2-}$  ion <sup>[15]</sup> and the electron deficient nature of the cluster.

### 5.2.4. Electrospray Mass Spectrometry

The electrospray mass spectrum for each sample was recorded in the negative ion mode from dmf solutions of crystalline  $[\text{K}(2,2,2\text{-crypt})]^+$  salts. The distinctive mass envelopes arising from the multiple isotopes of Ge and Ni have been simulated to facilitate assignments and verify nuclearities. The spectrum for  $\text{K}[\text{Ge}_9\text{Ni}_2(\text{PPh}_3)]^{1-}$  is shown in Figure 5.3 as an example. The spectrum of **1** (Figure 5.3) shows weak signals of the  $[\text{K}(2,2,2\text{-crypt})]$ -coordinated molecular ion of  $[\text{Ni}_6\text{Ge}_{13}(\text{CO})_5]^-$  along with the decarbonyl loss products  $\text{Ni}_6\text{Ge}_{13}(\text{CO})_4^-$ ,  $\text{Ni}_6\text{Ge}_{13}(\text{CO})_2^-$  and ligand-free binary ion  $\text{Ni}_6\text{Ge}_{13}^-$ . Patterns of new compounds,  $\text{Ge}_9\text{Ni}_2(\text{CO})^-$  and  $\text{Ge}_9\text{Ni}_2^-$  are also

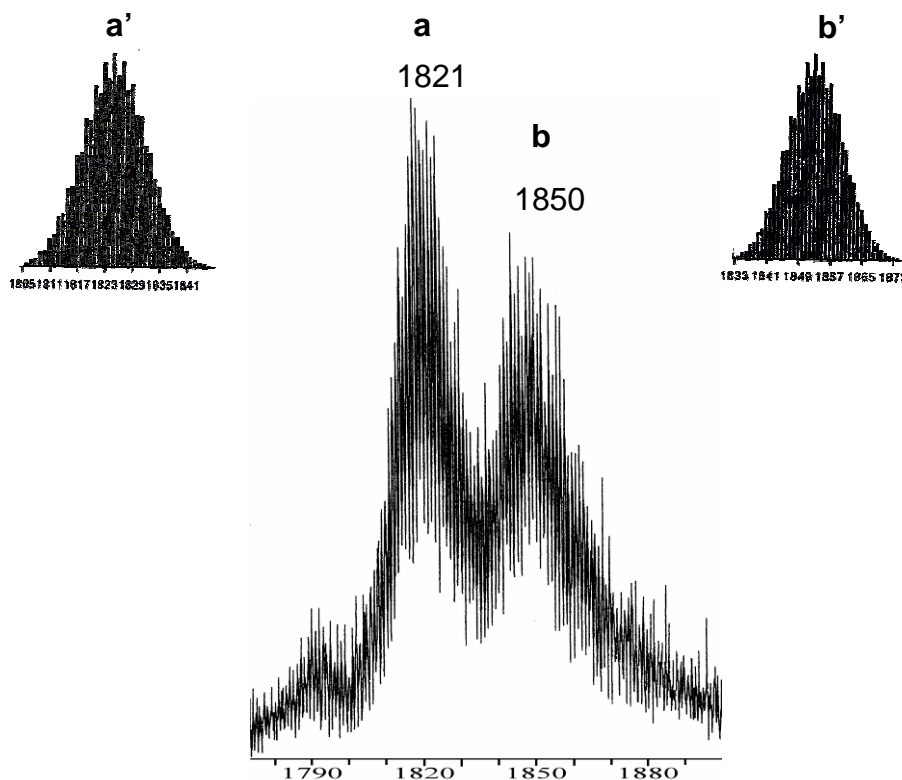


**Figure 5.3.** Experimental ESI-MS isotopic pattern of a)  $[\text{K}(2,2,2\text{-crypt}) \text{Ge}_{13}\text{Ni}_6(\text{CO})_4]^{1-}$  a') Simulated pattern of A, b)  $[\text{K}(2,2,2\text{-crypt}) \text{Ge}_{13}\text{Ni}_6(\text{CO})_5]^{1-}$ , b') Simulated pattern of b.

observed as well as peaks for the  $\text{Ge}_4\text{Ni}_4(\text{CO})_4^-$  cluster ion paired to  $\text{K}^+$  and  $[\text{K}(2,2,2\text{-crypt})]^{1+}$ .

The negative ion electrospray mass spectrum of dmf solution constituted from crystalline  $[\text{K}(2,2,2\text{-crypt})]_2[\text{Ge}_9\text{Ni}_2(\text{PPh}_3)]$  shows an intense signal for the  $\text{K}[\text{Ge}_9\text{Ni}_2(\text{PPh}_3)]^{1-}$  molecular ion with the expected mass envelope (Figure 5.4a). As is common for these types of Zintl ions, the potassium-coordinated ion pair,  $\text{K}[\text{Ge}_9\text{Ni}_2(\text{PPh}_3)]^{1-}$ , appears as the parent ion, ( $m/z$  1072.1) and the fully charged anion is not observed. The ligand free Ge-Ni cluster anion  $\text{K}[\text{Ge}_9\text{Ni}_2]^{1-}$  was also observed as well as the CO substituted cluster,  $[\text{K}(2,2,2\text{-crypt})\text{Ge}_9\text{Ni}_2(\text{CO})]^{1-}$ , (Figure 5.4b) which presumably results from a trace contamination in the sample.

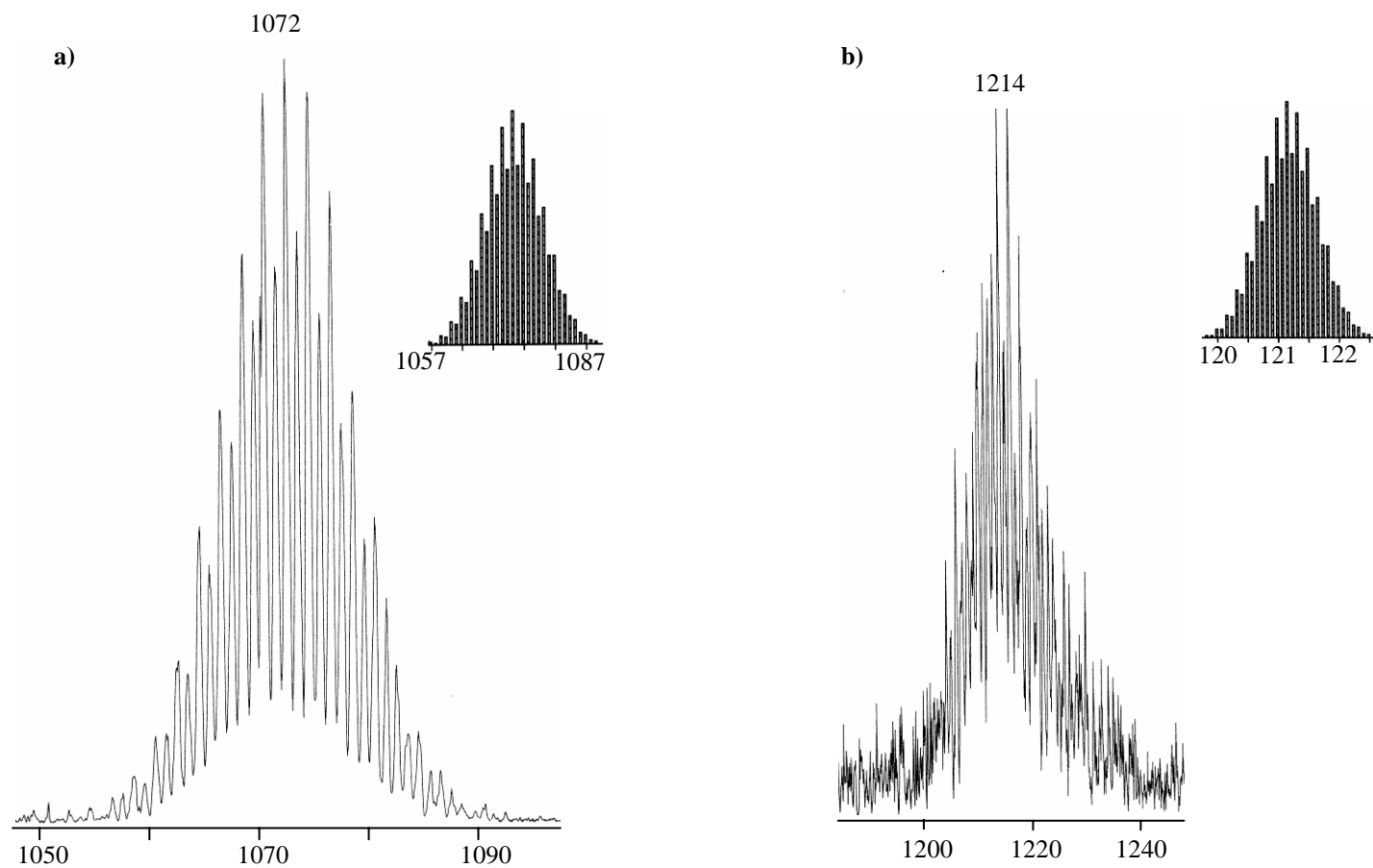


**Figure 5.4.** a) ESI-mass spectrum of the  $\text{K}[\text{Ge}_9\text{Ni}_2(\text{PPh}_3)]^{1-}$  molecular ion. The inset shows the simulated mass envelope, b) Observed and calculated ESI-MS mass envelope for  $[\text{K}(2,2,2\text{-crypt})\text{Ge}_9\text{Ni}_2(\text{CO})]^{1-}$ .

### 5.3. Conclusions

The centered atom of **2** was reported as Ge by Gardner et. al.<sup>170</sup> The evaluation of the compound by X-ray analysis is limited. Because of the similarities in the scattering factors of Ni and Ge atoms, the refinement of the data might not have allowed for differentiating the two atoms. The centered Ge atom was assigned by primarily relying on electron counting principles (Wades rules) and remarkable structural similarities to other clusters of the same nuclearity (e.g.  $[\text{Sb}_7\text{Ni}_3(\text{CO})_3]^{3-}$ ). The discovery of isostructural  $[\text{Sn}_9\text{Pt}_2(\text{PPh}_3)]^{2-}$  anion prompted us to re-investigate the Ni-Ge system and the identity of **2**. Here, the higher precision CCD data is reported. In addition, ESI-MS data unequivocally identify the ion as  $[\text{Ge}_9\text{Ni}_2(\text{PPh}_3)]^{2-}$  with a centered Ni atom. The non-deltahedral *nido*-like structures of these hypo-*closo* clusters are most likely because of steric demands of the centered metal atom.

A new type of Zintl ion  $[\text{Ni}_6\text{Ge}_{13}(\text{CO})_5]^{4-}$  ion, **1**, has been found during the re-investigation of the synthesis of **2**. The anion was formed at lower temperatures and shorter reaction times. It has been shown that **2** can be formed both from **1** (Scheme 1) and directly from the reactions of  $\text{Ge}_9^{4-}$  and the  $\text{Ni}(\text{CO})_2(\text{PPh}_3)_2$ . The biicosahedral structure of **1** is unique to Zintl ion chemistry but is a known feature in bimetallic clusters of the coinage metals.<sup>172</sup> Other examples of this general class of compounds are the recently reported  $[\text{Pd}_2@\text{Ge}_{18}]^{4-}$  and  $[\text{Ni}_3@(\text{Ge}_9)_2]^{4-}$  cluster anions. The former is an 18 vertex, 2-focus, 40 electrons cluster with the expected *closo* architecture ( $2n+2$  cluster electrons per focus). On the other hand, the latter does not easily fit into

a Wadian description. It is also interesting to see that neither forms icosahedral structures that are structurally distinct from **1**.

In this study, the ligand free, gas phase ions are identified by ESI-MS. They have similar compositions to the ligand-free deltahedral Pb cluster,  $[\text{Ni}@\text{Pb}_{10}]^{2-}$ , presented in the chapter 3.  $\text{Ge}_9\text{Ni}_2^{-1}$  (or  $[\text{Ni}@\text{Ge}_9\text{Ni}]^{-1}$ ) are centered 10-vertex clusters similar to the  $[\text{Ni}@\text{Pb}_{10}]^{2-}$  and the gas phase  $[\text{Ni}@\text{Pb}_{10}]^{1-}$  ions.<sup>130</sup> The former presumably adopts the *nido*- like  $\text{C}_{3v}$  structure of **2** despite having 5 fewer electrons than the 22-electron *closo* - $[\text{Ni}@\text{Pb}_{10}]^{2-}$  cluster. Whereas most of the Zintl clusters of the group 14 elements and their transition metal derivatives have Wadian like structures, there are now several examples that do not. It is certain that more exceptions will be discovered.

## 5.4. Experimental Section

### 5.4.1. General Data

All reactions were performed in a nitrogen atmosphere drybox (Vacuum Atmosphere Co.).  $^{31}\text{P}\{^1\text{H}\}$  NMR spectrum was recorded on a Bruker DRX400 spectrometer at 162 MHz. Electrospray Mass Spectra (ESI-MS) were obtained by direct injection of dmf solutions into a Finnigan mass spectrometer. Samples were detected in the negative ion mode. An AMRAY 1820K scanning electron microscope with a potential of 20 kV was used for energy dispersive X-ray (EDX) studies.

## 5.4.2. Chemicals

Melts of nominal composition  $K_4Ge_9$  was made by fusion (at high temperature) of stoichiometric ratios of the elements. The chemicals were sealed in evacuated, silica tubes and heated carefully with a natural gas/oxygen flame. **CAUTION:** the synthesis of polygermanides can result in explosive mixtures and all fusion reactions should be conducted behind a blast shield inside of a well functioning hood. 4,7,13,16,21,24-Hexaoxa-1,10-diazobicyclo[8,8,8]-hexacosane (2,2,2-crypt) and  $Ni(CO)_2(PPh_3)_2$  were purchased from Aldrich. Anhydrous ethylenediamine (en) and dimethylformamide (DMF) were purchased from Fisher, vacuum distilled from  $K_4Sn_9$ , and stored under dinitrogen.

## 5.4.3. Synthesis

### 5.4.3.1. Preparation of $[K(2,2,2-crypt)]_4[Ni_6Ge_{13}(CO)_5] \cdot 1.5en$

In a vial  $K_4Ge_9$  (54mg, 0.07 mmol), 2,2,2-crypt (100 mg, 0.27 mmol), and  $[Ni(CO)_2(PPh_3)_2]$  (84 mg, 0.14 mmol) were dissolved in 4 ml of en yielding a red/brown mixture. This mixture was heated ( $35\text{ }^\circ\text{C} < T < 45\text{ }^\circ\text{C}$ ) and stirred for about 15 min. and filtered through a hot filter. After a week small thin black crystals of  $[K(2,2,2-crypt)]_4[Ni_6Ge_{13}(CO)_5] \cdot 1.5en$  precipitated. Yield ; ~ 20 mg (~30%). EDX Ge:Ni:K = 3.8:1.7:1. ESI-MS data: (m/z, ion) 1850  $[K(2,2,2-crypt)Ni_6Ge_{13}(CO)_5]^{1-}$ ; 1821  $[K(2,2,2-crypt)Ni_6Ge_{13}(CO)_4]^{1-}$ ; 1296  $[Ni_6Ge_{13}]^{1-}$ ; 1214  $[K(2,2,2-crypt)Ge_9Ni_2(CO)]^{1-}$ ; 838  $K[Ge_9Ni_2(CO)]^{1-}$ ; 810  $K[Ge_9Ni_2]^{1-}$ ; 770  $[Ge_9Ni_2]^{1-}$ ; 677  $K[Ge_4Ni_4(CO)_4]^{1-}$ .

### 5.4.3.2. Preparation of $[\text{K}(2,2,2\text{-crypt})]_2[\text{Ni}_2\text{Ge}_9(\text{PPh}_3)]\cdot\text{en}$

In a vial  $\text{K}_4\text{Ge}_9$  (54mg, 0.007 mmol), 2,2,2-crypt (100 mg, 0.27 mmol), and  $[\text{Ni}(\text{CO})_2(\text{PPh}_3)_2]$  (84 mg, 0.14 mmol) were dissolved in 4 ml of en yielding a red/brown mixture. This mixture was boiled and stirred for about 25 min., and filtered through a hot filter. After 3-4 days block-shaped black crystals of  $[\text{K}(2,2,2\text{-crypt})]_2[\text{Ni}_2\text{Ge}_9(\text{PPh}_3)]\cdot\text{en}$  started to precipitate. Yield; ~ 20 mg (~30%). EDX analysis on crystals showed presence of K, P, Ge, and Ni. ESI-MS data: (m/z, ion) 1447  $[\text{K}(2,2,2\text{-crypt}) \text{Ni}_2\text{Ge}_9(\text{PPh}_3)]^{-1}$ , 1072  $\text{K}[\text{Ni}_2\text{Ge}_9(\text{PPh}_3)]^{-1}$ , 838  $\text{K}[\text{Ni}_2\text{Ge}_9(\text{CO})]^{-1}$ , 810  $\text{K}[\text{Ni}_2\text{Ge}_9]^{-1}$ .

### 5.4.4. Interconversion Studies

#### 5.4.4.1. Conversion of 1 to 2.

In a dry box, 36mg of  $[\text{K}(2,2,2\text{-crypt})]_4[\text{Ni}_6\text{Ge}_{13}(\text{CO})_5]$  crystals were dissolved in 4ml dmf. ESI-MS data were recorded to confirm the presence of  $[\text{Ni}_6\text{Ge}_{13}(\text{CO})_5]^{-}$  and  $[\text{K}(2,2,2\text{-crypt})] [\text{Ni}_6\text{Ge}_{13}(\text{CO})_5]^{-}$ ,  $[\text{Ni}_2\text{Ge}_9(\text{CO})]^{-}$  and  $[\text{Ni}_2\text{Ge}_9]^{-}$  ions before the interconversion experiments. 3mg of  $\text{PPh}_3$  was added to the starting solution and the reaction mixture was stirred for 30 min at ~118 °C. The resulting ESI-MS spectra showed signals of  $\text{K}[\text{Ni}_2\text{Ge}_9(\text{PPh}_3)]^{-}$  and  $[\text{Ni}_2\text{Ge}_9(\text{PPh}_3)]^{-}$  ions.

#### 5.4.4.2. Attempted conversion of 2 to 1

In dry box, 20mg of  $[\text{K}(2,2,2\text{-crypt})]_2[\text{Ni}_2\text{Ge}_9(\text{PPh}_3)]\cdot\text{en}$  crystals were dissolved in 4ml dmf. ESI-MS data were recorded to confirm the presence of  $[\text{Ni}_2\text{Ge}_9(\text{PPh}_3)]^{-}$  and  $[\text{K}(2,2,2\text{-crypt})][\text{Ni}_2\text{Ge}_9(\text{PPh}_3)]^{-}$  ions before the interconversion experiment. The solution was placed in a schlenk flask, the head gasses evacuated

and the flask back filled with CO gas. The reaction mixture was stirred for 3 hr. under the CO atmosphere. The resulting ESI-MS spectra showed decomposition of the starting material but did not show the formation of **1** or the  $[\text{Ni}_2\text{Ge}_9(\text{CO})]^-$  ion.

#### **5.4.5. Crystallographic Studies**

The crystal structures of the complexes were determined at single crystal X-ray facility at Chemistry and Biochemistry Department, University of Maryland, by Dr. James Fettingner.

## Chapter 6

### Conclusions

The hunt for discovering new highly stable clusters that can be used as building blocks for nanomaterials has become a leading thread in cluster science. Clusters with enhanced stabilities are generally referred as ‘magic number’ clusters. The two of the most famous classes of magic number clusters are the fullerene cages (e.g.  $C_{60}$ ) and the centered icosahedral cages (e.g.  $Al_{13}^-$ ). The basis of the enhanced stability varies extensively. The special stability of the  $C_{60}$  is due to its covalent-bonded and highly symmetric framework, whereas the stability of the  $Al_{13}^-$  arises mainly from its closed-shell electronic structure and high HOMO-LUMO gap.<sup>122</sup> Even though fullerenes have been prepared in the gas and the solid phases, to our knowledge;  $Al_{13}^-$  is only identified in gas phase.

The centered icosahedra ( $M_{13}$ ) are the smallest member of the growth sequence of magic number clusters. Therefore, they serve as nucleation sites for larger clusters growing by successive accumulation of layers of atoms. Due to their special structural and electronic properties, the centered icosahedra have attracted a great deal of attention not only by inorganic chemists, but also by physical chemists. To date, varieties of ligated metal clusters have been isolated by inorganic chemists.

On the other hand, physical chemists have investigated *ligand free*, gas phase clusters and performed theoretical studies to predict their structures, bondings and electronic properties. The studies suggesting existence of such systems are numerous.

In this study, we have achieved a long term goal of the gas phase physical chemists. We have successfully isolated new, exciting *ligand-free* Zintl anions which have potential to be used as seeds to larger clusters. The  $[M@Pb_{12}]^{2-}$  ( $M = Pt, Pd, Ni$ ) ions are the *first isolated* free-standing centered icosahedra without any attendant ligands. The anions are the smallest possible subunit in a nanoparticle closest packed crystal lattice and are models for the core shell structures without any ligand spheres. Due to their highly symmetric closed-packed geometry and large HOMO-LUMO gap similar to the magic number clusters such as  $Al_{13}^-$  and  $[Al@Pb_{12}]^+$ , the anions can also be defined as ‘magic clusters’.

It is interesting to see that the general electronic structure of  $[M@Pb_{12}]^{2-}$  ( $M = Pt, Pd, Ni$ ) anions are similar to the closely related  $\sigma$ -aromatic cluster,  $[Al@Pb_{12}]^+$ .<sup>39</sup> Although the theoretical calculations revealed the aromatic nature of the  $[Al@Pb_{12}]^+$ , the results have not yet been verified experimentally. <sup>207</sup>Pb NMR study of the chemically stable  $[Pt@Pb_{12}]^{2-}$  anion represents the first experimental measure of the  $\sigma$ -aromaticity for centered icosahedral clusters, but the result conflicts with the aromatic shift predicted by the theory.

In this study, a new type of Zintl ion,  $[Ni@Pb_{10}]^{2-}$ , has also been synthesized. It is the *first* isolated ten-atom endohedral naked Zintl ion cluster with its homoatomic framework. Due to the stability, electronic and magnetic properties, the metal centered  $Pb_{10}$  clusters attracted great attention by both physical and inorganic

chemists. The structure and stability of the Ni@Pb<sub>10</sub> has been investigated by DFT prior to this work by Schrodtr et. al.<sup>176</sup> The bicapped tetragonal antiprism Ni@Pb<sub>10</sub> with D<sub>4d</sub> point symmetry is predicted to be the most stable isomer compared to other isomers. The successful isolation of this D<sub>4d</sub> symmetric [Ni@Pb<sub>10</sub>]<sup>2-</sup> anion bring theory and application one step closer to each other.

In this study, varieties of spectroscopic techniques have been used to investigate the unusual properties (e.g. structural and dynamic) of the cluster anions. Since the most of the clusters have been synthesized in this study constituted by NMR spin active metal atoms, the NMR spectroscopy is ideal to investigate atomic mobility on the nanoscale. <sup>207</sup>Pb NMR studies for the one focus asymmetric cluster, [Ni@Pb<sub>10</sub>]<sup>2-</sup>, revealed the fluxional nature of the cluster. Observing similar fluxionality for other “single focus” clusters, suggests that many small metallic particles have extensive atomic mobility.

High coordination is common to solid state compounds such as binary alkaline earth metal stannide, BaSn<sub>5</sub>. However, it is unusual to observe coordination number more than five for a Zintl ion cluster system. The synthesized [Ni<sub>2</sub>Sn<sub>17</sub>]<sup>4-</sup> anion comprises a Sn atom having eight coordination. This is the highest coordinated Zintl ion cluster reported to our knowledge.

Besides having unusual structural properties the two focus cluster anion, [Ni<sub>2</sub>Sn<sub>17</sub>]<sup>4-</sup>, reveals surprising dynamic behavior in solution. While the low temperature <sup>119</sup>Sn NMR spectra demonstrating four distinct chemical environments of the Sn atoms are consistent with the solid state structure of the compound, the spectra at higher temperatures illustrate a global exchange in the molecule. This behavior

indicates that all Sn atoms, including the unusually coordinated Sn, are in rapid exchange on the NMR time scale. Such studies showed that NMR analysis might provide valuable insight into the potential dynamic exchange between surface and bulk atoms on the nanoscale. These types of analysis methods are only amenable to bulk cluster materials, and they play an important role to understand and gain more information about the structures and properties of nanoparticles such as decrease in melting points of nanoparticles compared to the bulk metals and alloys.<sup>177</sup>

Wade-Mingos electron counting rules are used for many of the deltahedral Group 14 Zintl ion clusters to describe the structures. The nido-Pb<sub>9</sub><sup>4-</sup>, closo-Sn<sub>6</sub><sup>2-</sup> core in [Sn<sub>6</sub>{Cr(CO)<sub>5</sub>}<sub>6</sub>]<sup>2-</sup> anion and closo-[Ni@Pb<sub>10</sub>]<sup>2-</sup> are some of the examples have Wadlan type structures. As most of the group 14 Zintl ions have structures that are predicted by Wades rules, like boranes. Others such as [Sn<sub>9</sub>Pt<sub>2</sub>(PPh<sub>3</sub>)]<sup>2-</sup>, demonstrate deviations from Wades structure prediction principles. In this study, we have reported new example of Zintl ion cluster, [Ge<sub>9</sub>Ni<sub>2</sub>(PPh<sub>3</sub>)]<sup>2-</sup>, which also shows deviation from Wades Rules. A new type of transition metal stabilized Zintl anion, [Ge<sub>13</sub>Ni<sub>6</sub>(CO)<sub>5</sub>]<sup>4-</sup>, have also been isolated. The anion can be defined as two Ni centered icosahedra fused together by sharing central Ge<sub>3</sub>Ni<sub>2</sub>(CO)<sub>2</sub> pentagonal ring and two interstitial Ni atoms. Although this structure type is known in bimetallic clusters of coinage metals, it is unique to the Zintl ion chemistry.

To date, new exciting transition metal stabilized Zintl anions with few or no ligands have been prepared. They are promising candidates to be used both in nanotechnology and heterogeneous catalysis. They are rare examples of the endohedral, naked metal clusters and received a great deal of interest not only

because of their remarkable structures and non-traditional bonding natures, but also due to their unusual electronic and spectroscopic properties. In particular, the anions presented in the Chapter 2 (i.e.  $[\text{Pt}@\text{Pb}_{12}]^{2-}$ ) demonstrate remarkable similarities with fullerenes and described as potential bridge between molecular ions and nanomaterials.<sup>163</sup> Due to their chemical and electronic stabilities, the anions are suitable building blocks to fabricate cluster-assembled nanostructures. Their stability, fullerene like properties and potential sigma aromaticity give them unique status in the growing class of endohedral naked metal clusters.

## References

1. Brus, L., *Appl. Phys. A* **1991**, 53, 465.
2. Lewis, L. N., *Chem. Rev.* **1993**, 93, 2693.
3. Smyth, J. F., *Science* **1992**, 258, 414.
4. Aiken III, J. D.; Lin, Y.; Finke, R. G., *J. Mol. Catal. A: Chem.* **1996**, 114, 29.
5. Rao, C. N. R.; Cheetham, A. K., *J. Mater. Chem.* **2001**, 11, 2887.
6. Faraday, M., *Phil. Trans. Roy. Soc.* **1857**, 147, 145.
7. Scharfl, W., *Adv. Mater.* **2000**, 12, 1899.
8. Margitfalvi, J. L.; Borbath, I.; Lazar, K.; Tfirst, E.; Szegedi, A.; Hegedus, M.; Gobolos, S., *J. Catal.* **2001**, 203, 94.
9. Meriaudeau, P.; Naccache, C.; Thangaraj, A.; Bianchi, C. L.; Carli, R.; Vishvanathan, V.; Narayanan, S., *J. Catal.* **1995**, 154, 345.
10. Stagg, S. M.; Querini, C. A.; Alvarez, W. E.; Resasco, D. E., *J. Catal.* **1997**, 168, 75.
11. Schubert, M. M.; Kahlich, M. J.; Feldmeyer, G.; Huttner, M.; Hackenberg, S.; Gasteiger, H. A.; Behm, R. J., *PCCP* **2001**, 3, 1123.
12. Llorca, J.; Homs, N.; Fierro, J. L. G.; Sales, J.; delaPiscina, P. R., *J. Catal.* **1997**, 166, 44.
13. Srinivas, S. T.; Rao, P. K., *J. Catal.* **1998**, 179, 1.
14. Schmid, G., *Clusters and colloids*; VCH: Weinheim, 1994.
15. Elghanian, R.; Storhoff, J. J.; Mucic, R. C.; Letsinger, R. L.; Mirkin, C. A., *Science* **1997**, 277, 1078.
16. Vossmeier, T.; Delonno, E.; Heath, J. R., *Angew. Chem. Int. Ed.* **1997**, 36, 1080.
17. Antoniette, M.; Goltner, C., *Angew. Chem. Int. Ed.* **1997**, 36, 910.

18. Glanz, J., *Science* **1995**, 269, 1363.
19. Schon, G.; Simon, U., *Colloid Polym. Sci.* **1995**, 273, 202.
20. Lin, Y.; Finke, R. G., *J. Am. Chem. Soc.* **1994**, 116, 8335.
21. Schmidt, T. J.; Noeske, M.; Gasteiger, H. A.; Behm, R. J.; Britz, P.; Brijoux, W.; Bonnemann, H., *Langmuir* **1997**, 13, 2591.
22. Pool, R., *Science* **1990**, 248, 1186.
23. Bonnemann, H.; Braun, G.; Brijoux, W.; Brinkmann, R.; Schulze Tilling, A.; Seevogel, K.; Siepen, K., *J. Organomet. Chem.* **1996**, 520, 143.
24. Hunter, R. J., *Foundations of Colloid Science*; Oxford Univ. Press: New York, 1987.
25. Aiken III, J. D.; Finke, R. G., *J. Mol. Catal. A: Chem.* **1999**, 145, 1.
26. Vargaftik, M. N.; Zargorodnikov, V. P.; Stolarov, I. P.; Moiseev, I. I.; Kochubey, D. I.; Likhobov, V. A.; Chuvilin, A. L.; Zamaraev, K. I., *J. Mol. Catal.* **1989**, 53, 315.
27. Bergeron, D. E.; Castleman, A. W.; Morisato, T.; Khanna, S. N., *Science* **2004**, 304, 84.
28. Bowen, K. H., *Personal communication* **2005**.
29. Ecker, A.; Weckert, E.; Schonkel, H., *Nature* **1997**, 387, 379.
30. Toshima, N.; Yonezawa, T., *New J. Chem.* **1998**, 1179.
31. Kumar, V.; Kawazoe, Y., *App. Phys. Lett.* **2002**, 80, 859.
32. Lu, J.; Nagase, S., *Chem. Phys. Lett.* **2003**, 372, 394.
33. Pyykko, P.; Runeberg, N., *Angew. Chem. Int. Ed.* **2002**, 41, 2174.
34. Li, X.; Kiran, B.; Li, J.; Zhai, H.; Wang, L., *Angew. Chem. Int. Ed.* **2002**, 41, 4786.
35. Li, X.; Wang, L., *Phys. Rev. B* **2002**, 65, 153404.

36. Zhang, X.; Li, G. L.; Xing, X. P.; Zhao, X.; Tang, Z. C.; Gao, Z., *Rapid Commun. Mass Spectrom.* **2001**, 15, 2399.
37. Autschbach, J.; Hess, B. A.; Johansson, M. P.; Neugebauer, J.; Patzschke, M.; Pyykko, P.; Reiher, M.; Sundholm, D., *Phys. Chem. Chem. Phys.* **2004**, 6, 11.
38. Zhai, H.; Li, J.; Wang, L., **2004**, 121, 8369.
39. Neukermans, S.; Janssens, E.; Chen, Z. F.; Silverans, R. E.; Schleyer, P. V.; Lievens, P., *Phys Rev. Lett.* **2004**, 92, 163401-1.
40. Schleyer, P. V.; Maerker, C.; Dransfeld, A.; Jiao, H.; Hommes, N. J. R. v. E., *J. Am. Chem. Soc.* **1996**, 118, 6317.
41. Heine, T.; Schleyer, P. V.; Corminboeuf, C.; Seifert, G.; Reviakine, R.; Weber, J., *J. Phys. Chem. A* **2003**, 107, 6470.
42. King, R. B.; Heine, T.; Corminboeuf, C.; Schleyer, P. V., *J. Am. Chem. Soc.* **2004**, 126, 430.
43. Schleyer, P. V., *Chem. Rev.* **2001**, 101, 1115.
44. Escudero, M. J.; Hontanon, E.; Schwartz, S.; Boutonnet, M.; Daza, L., *J. Power Sources* **2002**, 106, 206.
45. Bergeld, J.; Kasemo, B.; Chakarov, D. V., *Surf. Sci.* **2001**, 495, L815.
46. Prasada, R., *Advances in Catalysis Science and Technology*; Halsted Press: 1985.
47. Sinfelt, J. H., *Bimetallic Catalysts*; Exxon Research and Eng. Comp.: 1976.
48. Muller, A. C.; Engelhard, P. A.; Weisang, J. E., *J. Catal.* **1979**, 56, 64.
49. Dautzenberg, F. M.; Helle, J. N.; Biloen, P.; Sachtler, W. M. H., *J. Catal.* **1980**, 63, 119.
50. Morimoto, Y.; Yeager, E. B., *J. Electroanal. Chem.* **1998**, 441, 77.
51. Fiddy, S. G.; Newton, M. A.; Campbell, T.; Corker, J. M.; Dent, A. J.; Harvey, I.; Salvini, G.; Turin, S.; Evans, J., *Chem. Comm.* **2001**, 445.

52. Huang, Z.; Fryer, J. R.; Park, C.; Stirling, D.; Webb, G., *J. Catal.* **1998**, 175, 226.
53. Borgna, A.; Garetto, T. F.; Monzon, A.; Apesteguia, C. R., *J. Catal.* **1994**, 146, 69.
54. Goetz, J.; Volpe, M. A.; Sica, A. M.; Gigola, C. E.; Touroude, R., *J. Catal.* **1997**, 167, 314.
55. Lanh, H. D.; Khoai, N.; Thoang, H. S.; Volter, J., *J. Catal.* **1991**, 129, 58.
56. Kesanli, B., *Ph.D. Dissertation*; 2002.
57. Moses, M.; Fettinger, J.; Eichhorn, B., *Science* **2003**, 300, 778.
58. Joannis, A., *Comp. Rend.* **1891**, 113, 795.
59. Joannis, A., *Comp. Rend.* **1892**, 114, 585.
60. Kraus, C. A., *J. Am. Chem. Soc.* **1907**, 29, 1557.
61. Kraus, C. A., *J. Am. Chem. Soc.* **1922**, 44, 1216.
62. Smyth, F. H., *J. Am. Chem. Soc.* **1917**, 39, 1299.
63. Zinthe, E.; Goubeau, J.; Dullenkopf, W. Z., *Phys. Chem. Abt. A.* **1931**, 154, 1.
64. Zinthe, E.; Dullenkopf, W. Z., *Phys. Chem. Abt. B.* **1932**, 16.
65. Zinthe, E.; Harder, A. Z., *Phys. Chem. Abt. A.* **1931**, 154, 47.
66. Diehl, L.; Khodadadeh, K.; Kummer, D., *J. Chem. Ber* **1976**, 109, 3404.
67. Adolphson, D. G.; Corbett, J. D.; Merryman, D. J., *J. Am. Chem. Soc.* **1976**, 98, 7234.
68. Fassler, T. F.; Hoffmann, R., *Angew. Chem. Int. Ed.* **1999**, 38, 543.
69. Corbett, J. D.; Edwards, P. A., *J. Am. Chem. Soc.* **1977**, 99, 3313.
70. Fassler, T. F.; Hoffmann, R., **1999**, 3339.
71. Todorov, E.; Sevov, S. C., *Inorg. Chem.* **1998**, 37, 3889.
72. Queneau, V.; Sevov, S. C., *Angew. Chem. Int. Ed.* **1997**, 36, 1754.

73. Belin, C. H. E.; Corbett, J. D.; Cisar, A., *J. Am. Chem. Soc.* **1977**, 99, 7163.
74. Dahlmann, W.; vonSchnering, H. G., *Naturwissenschaften* **1973**, 60, 429.
75. Dahlmann, W.; Vschneri.Hg, *Naturwissenschaften* **1972**, 59, 420.
76. Laves, F., *Naturwissenschaften* **1941**, 29, 244.
77. Critchlow, S. C.; Corbett, J. D., *Inorg. Chem.* **1984**, 23, 770.
78. Fassler, T. F., *Coord. Chem. Rev.* **2001**, 215, 347-377.
79. Eichhorn, B. W.; Haushalter, R. C., *J. Chem. Soc. Chem. Commun.* **1990**, 937.
80. Campbell, E. B.; Schrobilgen, G. J., *Inorg. Chem.* **1997**, 36, 4078.
81. Critchlow, S. C.; Corbett, J. D., *J. Am. Chem. Soc.* **1983**, 105, 5715.
82. Fassler, T. F.; Hunziker, M., *Inorg. Chem.* **1994**, 33, 5380.
83. Fassler, T. F.; Schutz, U., *Inorg. Chem.* **1999**, 38, 1866.
84. Corbett, J. D., *Chem. Rev.* **1985**, 85, 383.
85. Rudolph, R. W.; Wilson, W. L.; Parker, F.; Taylor, R. C.; Young, D. C., *J. Am. Chem. Soc.* **1978**, 100, 4629.
86. Wade, K., *Adv. Inorg. Chem. Radiochem* **1976**, 18, 1.
87. Xu, L.; Sevov, S. C., *J. Am. Chem. Soc.* **1999**, 121, 9245.
88. Ugrinov, A.; Sevov, S. C., *J. Am. Chem. Soc.* **2002**, 124, 10990.
89. Ugrinov, A.; Sevov, S. C., *Inorg. Chem.* **2003**, 42, 5789.
90. Downie, C.; Tang, Z. J.; Guloy, A. M., *Angew. Chem. Int. Ed.* **2000**, 39, 338.
91. Downie, C.; Mao, J. G.; Guloy, A. M., *Inorg. Chem.* **2001**, 40, 4721.
92. Nienhaus, A.; Hauptmann, R.; Fa'ssler, T. F., **2002**, 41, 3213.
93. Eichhorn, B. W.; Haushalter, R. C.; Pennington, W. T., *J. Am. Chem. Soc.* **1988**, 110, 8704.
94. Kesanli, B.; Fettingner, J.; Eichhorn, B., *Chem. Eur. J.* **2001**, 7, (24), 5277.

95. Kesanli, B.; Fettingner, J.; Gardner, D. R.; Eichhorn, B., *J. Am. Chem. Soc.* **2002**, 124, 4779.
96. Schiemenz, B.; Huttner, G., *Angew. Chem. Int. Ed.* **1993**, 32, 297.
97. Renner, G.; Kircher, P.; Huttner, G.; Rutsch, P.; Heinze, K., *Eur. J. Inorg. Chem.* **2001**, 973.
98. Kauzlarich, S. M., *Chemistry, Structure and Bonding of Zintl Phases and Ions*; VCH Publishers Inc.: New York, 1996.
99. Goicoechea, J. M.; Sevov, S. C., *J. Am. Chem. Soc.* **2005**, 127, 7676.
100. Goicoechea, J. M.; Sevov, S. C., *Angew. Chem. Int. Ed.* **2005**, 44, 4026.
101. Muller, A. C., *Science* **2003**, 300, 749.
102. Tran, N. T.; Dahl, L. F., *Angew. Chem. Int. Ed.* **2003**, 42, 3533.
103. Ceriotti, A.; Demartin, F.; Heaton, B. T.; Ingallina, P.; Longoni, G.; Manassero, M.; Marchionna, M.; Masciocchi, N., *J. Chem. Soc. Chem. Commun.* **1989**, 786.
104. Tran, N. T.; Kawano, M.; Dahl, L. F., *J. Chem. Soc., Dalton Trans.* **2001**, 2731.
105. Muller, A. C.; Krickemeyer, E.; Bogge, H.; Schmidtman, M.; Roy, S.; Berkle, A., *Angew. Chem. Int. Ed.* **2002**, 41, 3604.
106. Teo, B. K.; Zhang, H., *Coord. Chem. Rev.* **1995**, 143, 611-636.
107. Teo, B. K.; Strizhev, A.; Elber, R.; Zhang, H., *Inorg. Chem.* **1998**, 37, 2482.
108. Pignolet, L. H.; Aubart, M. A.; Craighead, K. L.; Gould, R. A. T.; Krogstad, A.; Wiley, J. S., *Coord. Chem. Rev.* **1995**, 143, 219.
109. Greenwood, N. N.; Earnshaw, A., *Chemistry of the elements*; Pergamon Press: Oxford, 1984.
110. Grimes, R. N., *Coord. Chem. Rev.* **1995**, 143, 71.
111. Grimes, R. N., *Carboranes*; Academic Press: New York, 1970.

112. TillardCharbonnel, M. M.; Belin, C. H. E.; Manteghetti, A. P.; Flot, D. M., *Inorg. Chem.* **1996**, 35, 2583.
113. Pauling, L., *Proc. Nat. Acad. Sci.* **1988**, 85, 2025.
114. Dong, Z. C.; Corbett, J. D., *J. Am. Chem. Soc.* **1995**, 117, 6447.
115. Wunderlich, J. A.; Lipscomb, W. N., *J. Am. Chem. Soc.* **1960**, 82, 4427.
116. Dong, Z. C.; Corbett, J. D., *Angew. Chem. Int. Ed.* **1996**, 35, 1006.
117. Paquette, L. A.; Balogh, D. W.; Usha, R.; Kountz, D.; Christoph, G. G., *Science* **1981**, 211, 575.
118. Scuseria, G. E.; Odom, G. K., *Chem. Phys. Lett.* **1992**, 195, 531.
119. Kroto, H. W.; Heath, J. R.; O'Brien, S. C.; Curl, R. F.; Smalley, R. E., *Nature* **1985**, 318, 162.
120. Schmid, G., *Polyhedron* **1988**, 7, 2321.
121. Nguyet, T. T.; Douglas, R. P.; Dahl, L. F., *Angew. Chem. Int. Ed.* **2000**, 39, 4121.
122. Li, X.; Wu, H.; Wang, X.; Wang, L., *Phys. Rev. Lett.* **1998**, 81, 1909.
123. Zope, R. R.; Baruah, T., *Phys. Rev. A.* **2001**, 64, 053202-1.
124. Gee, W.; Shaw, R. A.; Smith, B. C.; Bullen, G. J., *J. Chem. Soc.* **1964**, 4180.
125. Campbell, J.; Mercier, H. P. A.; Franke, H.; Santry, D. P.; Dixon, D. A.; Schrobilgen, G. J., *Inorg. Chem.* **2002**, 41, 86.
126. Campbell, J.; Dixon, D. A.; Mercier, H. P. A.; Schrobilgen, G. J., *Inorg. Chem.* **1995**, 34, 5798.
127. Edwards, P. A.; Corbett, J. D., *Inorg. Chem.* **1977**, 16, 903.
128. Zhang, H.; Teo, B. K., *Inorg. Chim. Acta* **1997**, 265, 213.
129. Wilson, W. L.; Rudolph, R. W.; Lohr, L. L.; Taylor, R. C.; Pyykko, P., *Inorg. Chem.* **1986**, 25, 1535.
130. Esenturk, E. N.; Fettinger, J.; Eichhorn, B., *Chem. Commun.* **2005**, 247.

131. Fassler, T. F.; Muhr, H.-J.; Hunziker, M., *Eur. J. Inorg. Chem.* **1998**, 1998, 1433.
132. Hirsch, A.; Chen, Z.; Jiao, H., *Angew. Chem. Int. Ed.* **2001**, 40, 2834.
133. Schleyer, P. V., *Personal communication* **2004**.
134. Esenturk, E. N.; Fettingner, J.; Lam, Y. F.; Eichhorn, B., *Angew. Chem. Int. Ed.* **2004**, 43, 2132.
135. Khanna, S. N.; Rao, B. K.; Jena, P., **2002**, 65, 125105.
136. Gromov, A.; Krawez, N.; Lassesson, A.; Ostrovskii, D. I.; Campbell, E. B., *Curr. App. Phys.* **2002**, 2, 51.
137. Campbell, E. B., *Appl. Phys. A* **1998**, 66, 241.
138. Seifert, G.; Bartl, A.; Dunsch, L.; Ayuela, A.; Rockenbauer, A., *Appl. Phys. A* **1998**, 66, 265.
139. Bethune, D. S.; Johnson, R. D.; Salem, J. R.; Devries, M. S.; Yannoni, C. S., *Nature* **1993**, 366, 123.
140. Fassler, T. F., *Angew. Chem. Int. Ed.* **2001**, 40, 4161.
141. Kesanli, B.; Fettingner, J.; Eichhorn, B., *Angew. Chem. Int. Ed.* **2001**, 40, 2300.
142. Menon, M.; Andriotis, A. N.; Froudakis, G., *Nano Lett.* **2002**, 2, 301.
143. Ohara, M.; Koyasu, K.; Nakajima, A.; Kaya, K., *Chem. Phys. Lett.* **2003**, 371, 490.
144. Kumar, V.; Kawazoe, Y., *Phys. Rev. Lett.* **2002**, 88, 235504.
145. Lu, J.; Nagase, S., *Phys. Rev. Lett.* **2003**, 90, 115506-1.
146. Sen, P.; Mitas, L., *Phys. Rev. B* **2003**, 68, 155404.
147. Kumar, V.; Singh, A. K.; Kawazoe, Y., *Nano Lett.* **2004**, 4, 677.
148. Kumar, V.; Kawazoe, Y., *App. Phys. Lett.* **2003**, 83, 2677.
149. Sun, Q.; Wang, Q.; Briere, T. M.; Kumar, V.; Kawazoe, Y.; Jena, P., *Phys. Rev. B* **2002**, 65, 235417.

150. Hagelberg, F.; Xiao, C.; Lester, W. A., *Phys. Rev. B* **2003**, 67, 035426-1.
151. Hiura, H.; Miyazaki, T.; Kanayama, T., *Phys. Rev. Lett.* **2001**, 86, 1733.
152. Vedernikov, A., *Personal communication* **2005**.
153. Pederson, M. R., *Personal communication* **2005**.
154. Nicolau, Y. F.; Dupuy, M.; Brunel, M., *J. Electrochem Soc* **1990**, 137, 2915.
155. O'Brien, P.; Nomura, R., *J. Mater. Chem.* **1995**, 5, 1761.
156. Wang, X. J.; Langetepe, T.; Persau, C.; Kang, B. S.; Sheldrick, G. M.; Fenske, D., *Angew. Chem. Int. Ed.* **2002**, 41, 3818.
157. Ahlrichs, R.; Anson, C. E.; Clerac, R.; Fenske, D.; Rothenberger, A.; Sierka, M.; Wieber, S., *Eur. J. Inorg. Chem.* **2004**, 2004, 2933.
158. Fenske, D.; Persau, C.; Dehnen, S.; Anson, C. E., *Angew. Chem. Int. Ed.* **2004**, 43, 305.
159. Steiner, J.; Stosser, G.; Schnockel, H., *Angew. Chem. Int. Ed.* **2004**, 43, 301.
160. Esenturk, E. N.; Fettinger, J.; Eichhorn, B., *Polyhedron* **2005**, 25, 521.
161. Fassler, T. F.; Kronseder, C., *Angew. Chem. Int. Ed.* **1998**, 37, 1571.
162. Fassler, T. F.; Hunziker, M., *Z. Anorg. Allg. Chem.* **1996**, 622, 837.
163. Fassler, T. F.; Hoffmann, S. D., *Angew. Chem. Int. Ed.* **2004**, 43, 6242.
164. Yong, L.; Hoffmann, S. D.; Fassler, T. F., *Z. Anorg. Allg. Chem.* **2004**, 630, 1977.
165. Goicoechea, J. M.; Sevov, S. C., *Inorg. Chem.* **2005**, 44, 2654.
166. Haushalter, R. C.; O'Connor, C. M.; Haushalter, J. P.; Umarji, A. M.; Shenoy, G. K., *Angew. Chem. Int. Ed.* **1984**, 23, 169.
167. Esenturk, E. N.; Eichhorn, B.; Fettinger, J., *submitted to J. Am. Chem. Soc.*, **2006**.
168. Lee, S., *Inorg. Chem.* **1992**, 31, 3063.

169. Kesanli, B.; Fettinger, J. C.; Gardner, D. R.; Eichhorn, B. W., *Chem. Eur. J.* **2001**, 5277.
170. Gardner, D. R.; Eichhorn, B. W.; Fettinger, *Angew. Chem. Int. Ed.* **1996**, 35, 2852.
171. Teo, B. K.; Zhang, H.; Kean, Y.; Dang, H.; Shi, X. B., *J. Chem. Phys.* **1993**, 99, 2929.
172. Teo, B. K.; Zhang, H., *Coord. Chem. Rev.* **1995**, 143, 611.
173. Belin, C.; Mercier, H.; Angilella, V., **1991**, 15, 931.
174. Yong, L.; Hoffmann, S. D.; Fassler, T. F., *Z. Anorg. Allg. Chem.* **2005**, 631, 1149.
175. Charles, S.; Eichhorn, B. W.; Bott, S. G., *J. Am. Chem. Soc.* **1993**, 115, 5837.
176. Schrodtr, C.; Weigend, F.; Ahlrichs, R., *Z. Anorg. Allg. Chem.* **2002**, 628, 2478.
177. Buffat, P.; Borel, J. P., *Phys. Rev. A* **1976**, 13, 2287.